Rapid Single Molecule FRET Biosensing Assay for Nucleic Acid Detection

by

Kunal Khanna

A dissertation submitted in partial fulfillment
of the requirements for the degree of
Doctor of Philosophy
(Chemistry)
in the University of Michigan
2022

Doctoral Committee:

Professor Nils G. Walter, Chair
Professor Ryan Bailey
Professor Zhan Chen
Professor Muneesh Tewari

Kunal Khanna

khannak@umich.edu

ORCID: 0000-0001-5400-1023

ACKNOWLEDGMENTS

This five and a half year PhD journey has been a tremendous period of growth and development for me as a scientist and professional and it was made possible with some wonderful support and mentorship. This experience at the University of Michigan and the Walter lab has been a pleasure and I am grateful to have gotten the opportunity and support necessary to grow into an independent scientist.

I would like to thank Prof. Nils G. Walter for his consistent and responsive support, mentorship and advice as I went through this journey. I am grateful for the space and example he provided for me to grow into a stronger, more effective researcher. I would also like to thank Dr. Alexander Johnson-Buck for his extensive mentorship, support and advice when I joined the Walter lab and being a consistent, patient mentor as I developed my scientific thinking, habits, and understanding of various topics. Additionally, I would like to thank Dr. Shankar Mandal for his extensive collaboration and support to this dissertation as well as his wonderful advice in approaching experiments, conducting scientific writing. I learned so much from both and they were instrumental in pushing this dissertation to its completion. I would also like to thank my prior mentor, Juan Marcos Alarcon, for being tremendously supportive of both my personal and professional journey when I was a postbac and beyond as well as offering the mentorship, perspective, and advice that transitioned me to the path of a scientist.

This journey had it triumphs and its moments of discovery and clarity, but also its challenges and lows. I am thankful to have been part of the Walter lab which provided a great deal of perspective and assistance to both enjoy the highs and help in getting through the lows. I would like to thank my Walter lab colleagues for helping to make this a worthwhile experience and being there not only to listen to my questions, ideas, or perspective, but also to offer their own and enrich my experience. Additionally, my closest friends and family deserve tremendous thanks for being there to listen to me and offer support and a special place when I most needed it throughout my journey. This was an incredible journey with everyone and I will take all the things I've learned from it to the next stage of my professional journey.

TABLE OF CONTENTS

LIST OF FIGURES

LIST OF TABLES

ABSTRACT

Cancer is a complex, multi-faceted, and varied disease that comes with a substantial economic and health burden. Due to this immense burden and its increasing prevalence, diagnostic tools capable of detecting cancer and aiding treatment, especially at an early stage, have grown into a major area of interest for researchers and clinicians alike. There has especially been a growth in interest in liquid biopsies, which are assays that utilize biomarkers found in typical body fluids like blood and urine in order to diagnose cancer in the same way tissue biopsies normally do, but without the need for invasive procedures. Although cancer biomarkers come in many different forms, two in particular that have received the attention of researchers for liquid biopsies are circulating tumor DNAs and microRNAs due to their stability in body fluids and differential expression in healthy individuals versus cancer patients.

Several technologies have arisen and established themselves as gold standards for detecting and analyzing nucleic acid biomarkers, in particular, Polymerase Chain Reaction (PCR) and Next Generation Sequencing (NGS). While these techniques possess excellent sensitivity and throughput, respectively, they have drawbacks that include false negatives from amplification bias, primer mismatching causing false positives for short sequences like those of miRNAs, and laborious preparation for both techniques and extensive analysis for NGS. Our group recently developed a kinetic fingerprinting-based detection method that counts single target molecules directly from sample with ultra-high specificity. This amplification-free

approach, termed single-molecule recognition through equilibrium Poisson sampling (SiMREPS), immobilizes potential target molecules on a microscope slide surface and fingerprints them via binding and dissociation patterns of a freely diffusing fluorescent probe. This approach, however, had an upper limit on analysis speed as a higher probe concentration is necessary to accelerate binding speed and the associated background worsens the signal-to-noise ratio. This dissertation focuses on the development of a kinetics-based biosensor design, termed iSiMREPS, which incorporates intramolecular Förster Resonance Energy Transfer (FRET) to rapidly identify nucleic acid targets through conformational changes in the biosensor.

Chapter 2 highlights the biosensor design including the three component strands that comprise it called the anchor, capture and query strands and the development of a standardized design capable of rapidly alternating between two conformations to generate a target-identifying FRET signal pattern. In this chapter, I detail the optimizations necessary for the biosensor to perform effectively including capture probe modifications, optimization of the query probe and a competing sequence on the anchor for conformational flexibility and desirable kinetic behavior, and the introduction of the denaturant formamide to provide faster signal generation. Chapter 3 focuses on developing a full assay with the biosensor and details my optimizations to the imaging and slide preparation protocol, maximizing the effectiveness of formamide, improving sensitivity through toehold mediated strand displacement of target-unbound biosensors, and establishing limits of detection for a microRNA target as well a DNA target performed alongside a collaborator. Chapter 4 addresses multi-target detection and shows my development and refinement of biosensors for additional targets, the establishment of design principles and guidelines for generalized target detection, and the development of a multi-target well setup for use in panel assays. Combined, this thesis has developed a proof-of-concept and case for using a

biosensor-based assay for liquid biopsy detection, eventually in a spatially addressable microarray format.

Chapter 1. Introduction: Cancer Biomarker Detection, Relevant Technologies, and the Role of Biosensors and FRET

1.1 Scope of Cancer and Value of Diagnostics

Cancer has become an increasingly prevalent disease with the American Cancer Society estimating there will be ~1.9 million new cases and over 600,000 deaths in 2021 for the US alone[1]. Cancer carries an enormous financial burden on its patients with its direct medical costs estimated to be over 80 billion dollars in the year 2015[2]. Additionally, it carries a heavy toll in terms of physical and mental health as well as quality of life. The scale and scope of cancer as a disease has thus generated significant interest and development of basic and translational research, treatments and therapies, and various types of diagnostics.

The variation and complexity of cancer as a disease has also necessitated variation in the treatment modalities and diagnostics used in its assessment and treatment[3-5]. Effective diagnostics play a critical role in cancer treatments because they can provide detailed, critical information necessary for treatment including cancer stage, characteristics, as well as response to treatments[6, 7]. Early stage disease diagnostics are especially valuable because earlier diagnosis of cancer results in a better prognosis for patients; in fact certain cancers, such as pancreatic cancer, have particularly poor prognosis because early stage diagnosis is limited or unavailable [8-11].

An effective cancer diagnostic must be able to definitively detect a biomarker, a biological substance that, when present at specific levels within a cell or fluid sample collected from a patient reliably gives an indication of a certain disease or health state. To

accomplish this, there are several criteria that must be met. Firstly, the biomarker must be a reliable and consistent indicator for the cancer it is used to diagnose. Secondly, the diagnostic must show sufficient specificity so that it can detect its intended biomarker and establish a clear difference between a patient with and without the condition. Lastly, the diagnostic must have sufficient sensitivity because its limit of detection and dynamic range must be consistent with the abundance of the biomarker in a real sample. Speed is also desirable and even necessary in circumstances where there are large volumes of clinical samples for a certain disease. In this chapter, I will provide an overview of the significance of cancer biomarkers and assess developments and promising of emerging cell-free nucleic acid biomarkers, evaluate existing detection technologies, assess single molecule kinetic fingerprinting approaches, and the value that can be provided by utilizing Förster Resonance Energy Transfer (FRET) and biosensors.

1.2 Cancer Biomarkers and Emerging Developments

Biomarkers serve a critical role in the detection and treatment process for cancer. Potential biomarkers themselves come in many shape and forms and include cells, proteins, various types of DNA and RNA, and even epigenetic modifications like methylation[12-14]. This breadth is reflective of the complexity and variation of cancer as a disease as well as the different characteristics of diverse cancer types. Due to this variation and because each cancer has its own complexities, mechanisms, and characteristics, there is a large well of research done on cancer biomarkers that includes basic research studies, translational studies, and clinical studies that cover different aspects of biomarkers including their role and mechanisms within their disease state, their feasibility for diagnostic purposes, and their applicability to clinical use[15, 16]. Clinically, biomarkers can serve many different purposes. Certain biomarkers, such as prostate-specific antigen (PSA) and HER2 are used to aid in the detection of cancer and offer predictive

value in detecting certain cancer types[17, 18]. Other biomarkers offer value in providing information about the cancer itself such as the tumor status, the nature of the tumor, the types of cancer cells, as well as even the responsiveness to different types of cancer treatment[15, 16]. Some examples of these biomarkers include alfa-fetoprotein (AFP)[19], Human chorionic gonadotropin-β (β-hCG)[20], and Carcinoembryonic antigen (CEA)[21]. One factor that is critical for adoption of biomarkers, due to variance in assay protocols, labs, and patient samples, is reproducibility where indications of disease are reliable and consistent[22, 23].

Cell-free nucleic acids (cfNAs) have emerged as biomarkers of major interest because of their relative stability in common body fluids and ability to be detected directly from those fluids[24, 25] (Anfossi et al., 2018; Schwarzenbach et al., 2011). There is interest in using cfNAs for liquid biopsies, which are defined as cancer tests that diagnose by the detection of biomarkers from body fluids such as blood[26, 27] (Crowley et al., 2013; Heitzer et al., 2015). Liquid biopsies have garnered significant interest from clinicians because of their promise in achieving detection in a manner that is simpler and less invasive than tissue biopsies, whose invasive nature also precludes their use in certain patients (**Figure 1.1**)[28, 29]. Among cfNA biomarkers, two in particular that have been especially notable are circulating tumor DNAs (ctDNAs) and microRNAs (miRNAs). miRNAs are 21-25 nucleotide (nt) short, non-coding RNAs that are major regulators of gene expression and are thought to be involved in regulating over half of all human protein coding genes[30-32]. After transcription and processes in the nucleus, they are exported, further processed and then incorporated into a complex called an RNA-induced silencing complex where they act on mRNAs for which they have some or complete sequence specificity so that they can reduce or silence the expression of the genes those mRNAs represent. miRNAs have demonstrated a strong connection to cancer with miRNA families such as the

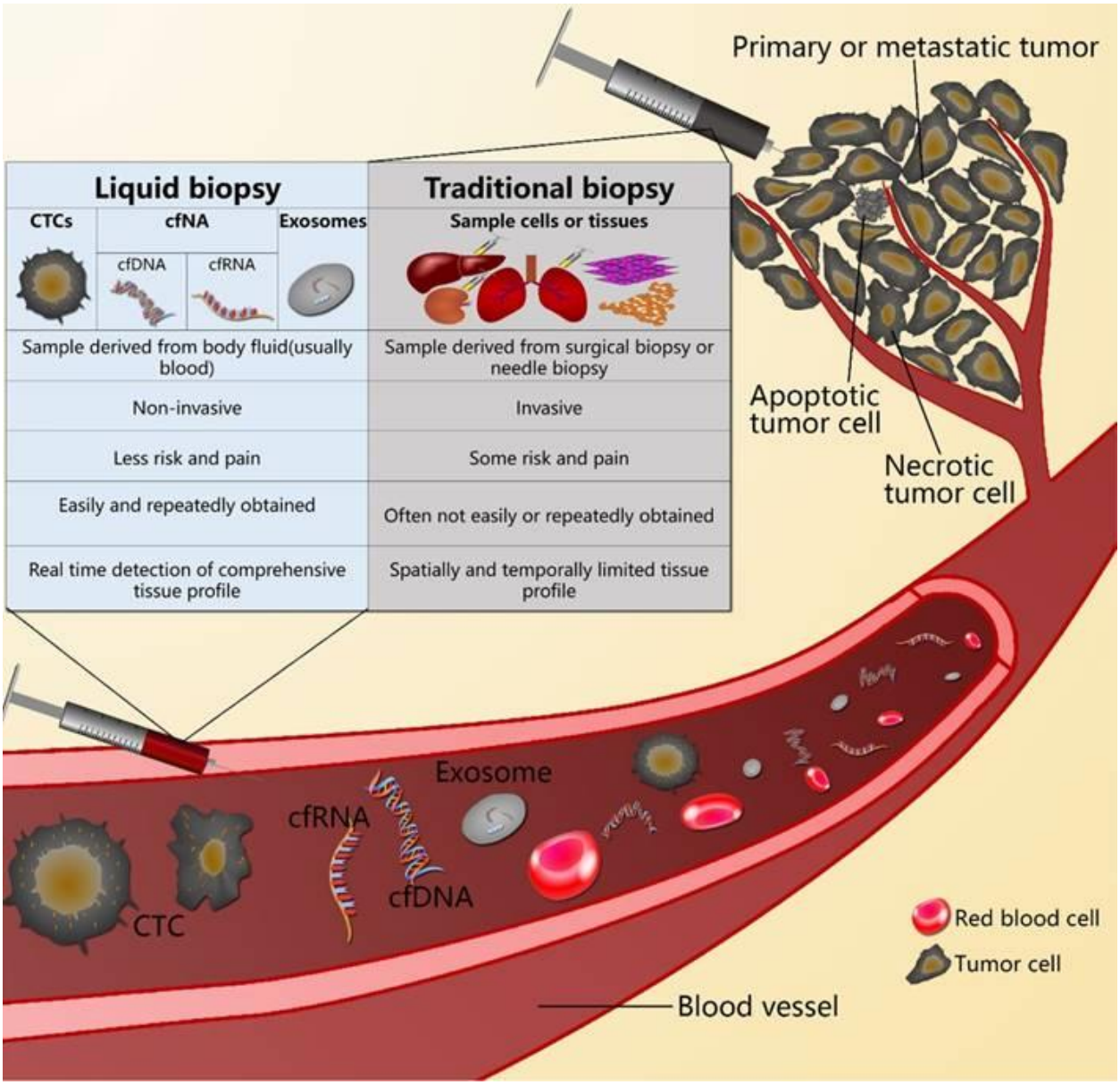

Figure 1.1. A comparison of liquid biopsies to traditional biopsies in terms of typical biomarkers, procedures, availability and patient experience**.** [1]

miR-17/92 cluster being dubbed oncomiRs for their role in cancer pathways[33, 34]. Additionally, many different miRNAs, have shown promise as biomarkers for cancer detection due to their

[1] This figure is reproduced in full from Qi ZH, Xu HX, Zhang SR, Xu JZ, Li S, Gao HL, Jin W, Wang WQ, Wu CT, Ni QX, Yu XJ, Liu L. The Significance of Liquid Biopsy in Pancreatic Cancer. J Cancer 2018; 9(18):3417-3426 under the Creative Commons Attribution-Noncommercial 4.0 International license as linked: https://creativecommons.org/licenses/by-nc/4.0/#

different abundances in healthy versus cancer patients[35-37]. For example, miR-21 has shown promise for non-small cell lung cancer and breast cancer detection, whereas miR-141 has shown promise for prostate cancer[38-41]. They have emerged as promising candidates for liquid biopsies because unlike many other RNAs, they are stable in biofluid due to their association with protein complexes[24, 41]. ctDNAs are DNA strands that are found circulating in biofluid and are thought to have been secreted from cancer cells or released due to necrosis or apoptosis of said cells[42]. Interest has developed in using them as biomarkers because they are also suitable candidates for liquid biopsies as they, like miRNAs, also show different abundance in healthy versus cancer patients and stability in body fluids[35-37]. Some examples of ctDNAs include *EGFR* exon 19 deletion mutants and KRAS mutants[43, 44].

1.3 Nucleic Acid Detection Technologies

Since these cfNAs have a low abundance that can be in the femtomolar range for miRNAs and even lower for ctDNAs, which are often <1% of total cfDNAs[45-47], any detection technologies built for them must be extremely sensitive. Additionally, high specificity is especially critical for miRNAs because their short length increases the odds of off-target interactions and rapid detection with high throughput is desirable in clinical settings with large numbers of samples. Technologies to meet this need have arisen and they can be broadly divided into techniques that rely primarily on amplification, on direct hybridization of the target nucleic acid to a probe, or on some form sequencing often coupled with amplification as their main method of target identification. While all of these technologies have their strengths and are effective for certain targets, they are not without their own sets of weaknesses.

Amplification-based techniques primarily rely on Polymerase Chain Reaction (PCR) where the target nucleic acids are isolated, purified, sometimes reverse transcribed for RNAs and

then subject to continuous replication reactions to generate detectable levels of the original target. Quantitative PCR (qPCR) in particular is an established gold standard technique for nucleic acid detection and is sufficiently sensitive to detect mutant DNA with a point mutation even at allelic frequencies below 1%[48]. Droplet digital PCR (ddPCR) in particular is sensitive enough to detect down to a small copy number and provides absolute quantification, due to its compartmentalized droplet design and precise counting capabilities[49, 50]. PCR-based techniques, however, have a few drawbacks that reduce their utility for cfNA detection. They have issues with amplification bias which can result in false negatives if certain low-abundance sequences fail to amplify well[51]. They also generate false positives from replication error and are vulnerable to mismatching of primers when the sequence is short like for miRNAs[51]. Lastly, they can require considerable preparation due to a need for enzymatic reactions, isolation and purification. These limitations subsequently hamper specificity, especially for miRNAs, which is detrimental for their utility in cancer detection.

Hybridization-based techniques, such as microarrays, rely on complementary base pairing between their target and a complementary probe with one of the 2 being fluorescently labeled and have many amplification-free variants[52-54]. These techniques are typically simple in design and preparation and are a useful way to gather information about relatively higher abundance nucleic acids within a sample quickly. Single molecule array (SiMoA) for example, is able to achieve absolute quantification in a manner similar to ddPCR with minimal sample preparation and a simple workflow[52]. However, there is an upper limit on the specificity of these techniques due to the thermodynamics of hybridization[55]. This limitation can be quantified by the equation: $Q_{max,therm} = e^{-\Delta\Delta G°/RT}$ where $\Delta\Delta G°$ is the difference in free energy of target-probe

hybridization for two single nucleotide variants (SNVs) and the value of $Q_{max,therm}$ can be as low as 20[55, 56].

Lastly, sequencing-based techniques, of which Next-Generation Sequencing (NGS) is considered a gold standard, use fluorescently labeled bases to track their addition into a newly formed strand allowing the target nucleic acid to be identified by the fluorescent pattern over time which is indicative of its sequence. NGS has risen as another gold standard method because of its ability to identify and analyze a large number of different genetic targets at once as well as provide analysis at the level of the entire genome[57-59]. However, NGS has difficulty with shorter sequences with strong adapter ligation bias which introduce additional sources of error and often require additional steps to address[60]. NGS typically relies on pre-amplification as part of its workflow and thus has all of the same weaknesses that amplification techniques do. Lastly, NGS also requires considerable preparation from libraries, to adapter ligation to complex bioinformatics analysis since fragment formation and analysis are of its workflow[61-63]. While NGS has a significant edge in varied, large scale analysis, its drawbacks limit its utility for more targeted, specific analysis and in settings where fast, simple analysis with fewer resources is desirable.

1.4 Single Molecule Kinetic Fingerprinting

Single molecule kinetic fingerprinting, developed by the Walter group as Single Molecule Recognition through Equilibrium Poisson Sampling (SiMREPS)[64] and conceptually related to the super-resolution fluorescence imaging technique DNA-PAINT[65], is an approach aiming to address many shortcomings of the existing techniques outlined above. SiMREPS was designed as a kinetics-based approach that identifies its target through its dynamic interactions with a fluorescent probe[64]. Single molecule fluorescence microscopy (SMFM) allows for absolute

quantification because it can image individual molecules and interrogate them for their interactions with fluorescent probes through analysis by software, giving an exact digital count of the number of nucleic acid molecules found, which is directly correlated to their concentration in the sample. This obviates the need for amplification and allows for more consistent detection of low concentrations of nucleic acids without the biases and errors that come with molecular amplification. SiMREPS, currently implemented, utilizes a total internal reflection fluorescence (TIRF) microscope because this allows any signal from the target to be restricted to a surface where it is captured as excitation of fluorophores is only possible through evanescent waves that penetrate the surface and travel only a short distance. This setup allows for single molecule observation as it provides a clearer field of view (FOV) without background from the sample bulk, permitting absolute quantification for SiMREPS.

As shown in **Figure 1.2A**, SiMREPS functions by capturing the target nucleic acid using a complementary probe that is surface-tethered, introducing fluorescent probes (FPs) complementary to a different target region and then imaging the signal over a time window to observe the fluorescent intensity as fluorescent probes bind and dissociate repeatedly over time. The surface of a coverslip or microscope slide is first coated with an adsorbent, which for SiMREPS is typically biotin-Polyethylene Glycol (PEG) mixed with methoxypolyethylene glycol (mPEG) which allows for binding of streptavidin, a protein with four biotin binding sites. A biotinylated DNA strand that is complementary to the target nucleic acid, called the capture probe, is then added which binds strongly to streptavidin and can bind to the target nucleic acid and effectively tether it to the surface of the microscope slide. After the target is captured, a FP that is complementary to another region of the target and is labeled with a fluorophore for imaging can then bind to the surface-tethered target. SiMREPS is designed so that the

association between the target and imager probe is weak and the probes will bind and dissociate repeatedly over time. This creates an observed signal that shows a pattern of alternating between high intensity where the imager probe is bound and low intensity when there is no bound probe (**Figure 1.2B**). In its simplest analysis, this signal pattern can be broken down into the number of transitions between the high intensity state, or bound state, and the low intensity or unbound state, as well as the dwell times for both. Through software analysis, these measures can be distinguished from those of non-specific interactions and background and thus serves as a kinetic fingerprint for target identification.

SiMREPS is able to achieve near-perfect specificity even for two miRNA SNVs[64] because even two similar strands will have slightly different kinetics which will become more apparent after sufficient observation. The probe kinetics can be modeled as a Poisson process and as the observation window is extended, the distribution of the number of binding and dissociation events (N_{b+d}) between the target and any non-targets becomes more and more distinct until it is clearly distinguished (**Figure 1.2D**). It is thus possible to virtually eliminate false positives from measurements by using a sufficiently long observation window. Additionally, this technique demonstrates a limit of detection in the low femtomolar range which is sufficient for detection of many miRNA targets[64, 66]. It also is usable with a direct sample and minimal preparation, allowing it to overcome several limitations previously described techniques often suffer from. However, SiMREPS requires about 10 minutes of analysis per FOV and needs 30 minutes total for target detection as previously demonstrated[64] and this analysis speed has an upper limit on how much it can be improved. Increasing analysis speed requires either weakening the target-FP interaction or raising the probe concentration so that the time the target does not have a probe bound is shorter and N_{b+d} count increases faster so that the needed

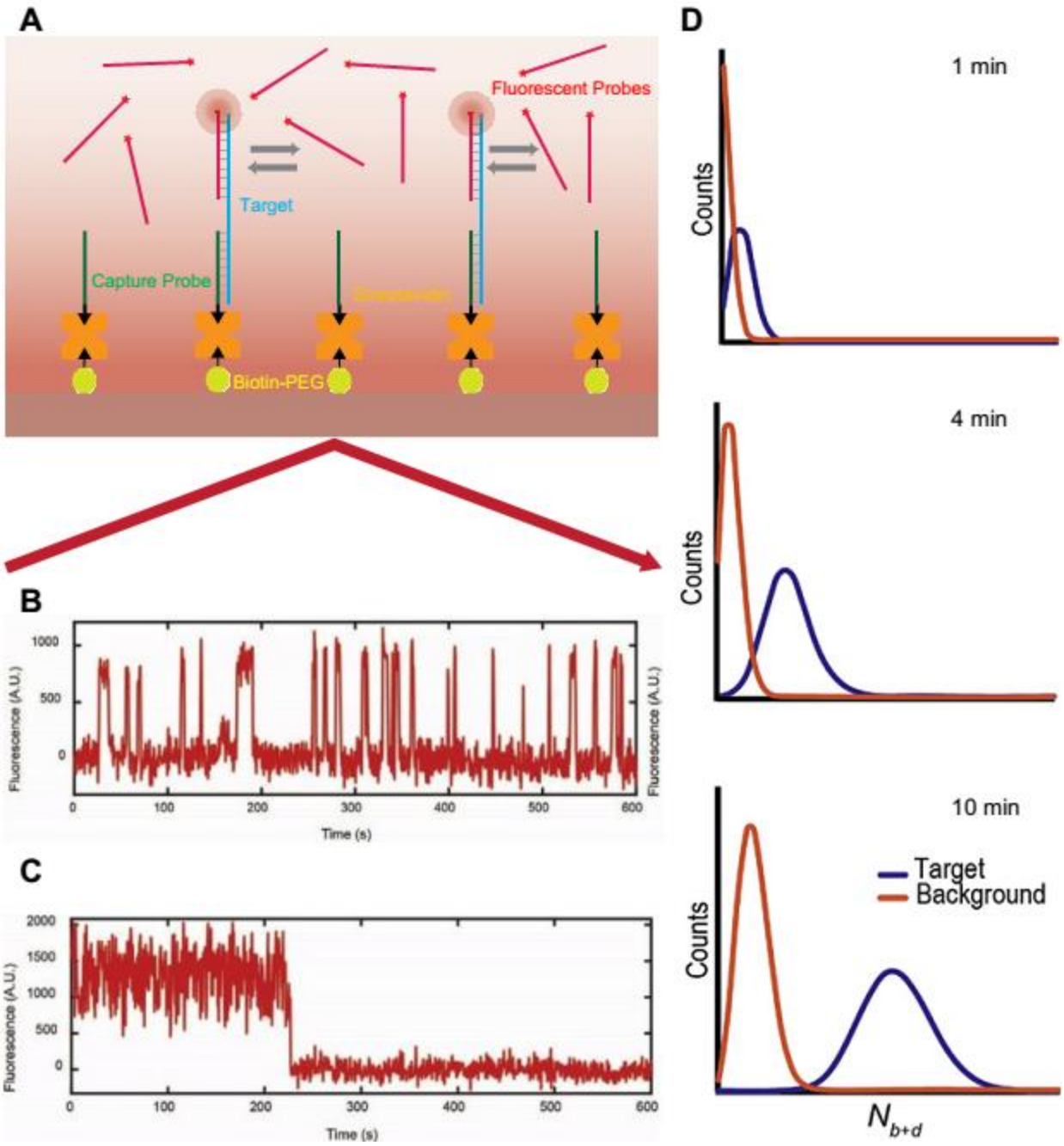

Figure 1.2. The SiMREPS technique. (A) The surface is passivated with Biotin-PEG and streptavidin which allows for a biotinylated capture probe to attach to streptavidin. This probe binds the target strongly on one end and tethers it to the surface and a fluorescent probe that weakly binds is introduced. The binding and dissociation of this fluorescent probe generates an on and off signal that is recorded and used to identify the target from the background, which rarely shows such signal transitions. (B) Signal in the presence of the nucleic acid target where there is frequent transitioning between bound and unbound states. (C) Signal in the absence of target which is much more static and lacks the characteristic transitioning. (D) As the imaging

time is increased, the number of binding and dissociation events observed in the presence of target increases and becomes more easily distinguished from the background.[2]

observation window shortens. However, increasing probe concentration also increases background noise due to increased non-specific surface proximity and interaction of unbound fluorescent probes. Additionally, while the speed can also be improved by reducing the target-FP binding region length or using a denaturant, this approach also has limits because shortening the target-FP binding region also reduces specificity. Lastly, while both reducing the target-FP binding region length and using denaturant can reduce the lifetime of the bound state, the unbound state will remain unaffected and this limits the extent to which speed can be improved. Overcoming this limitation will thus demand some innovation.

1.5 The Utility of Biosensors and FRET

Biosensors have been a major area of interest for researchers and industry alike because of their versatility and broad applicability to a variety of problems[67]. Biosensors are defined as analytical tools that can provide information about their analyte through the use of a biomaterial that serves as a recognition element for the analyte, a transduction method that converts the recognition of analyte into an observable signal, and a detector that can pick up the signal, ideally in a form that can be correlated to the amount of analyte[68, 69]. One aspect that allows biosensors to be extremely versatile is that they can be made from a variety of different biomaterials including DNA or RNA strands, proteins, and biological polymers[67]. Additionally, this versatility can be expanded further by utilizing different transduction mechanisms which include but are not limited to be mechanical, electrochemical, or optical mechanisms to generate

[2] This figure is adapted with permission in part from figures in Chatterjee, T*; Li, Z*; Khanna, K; Montoya, K; Tewari ,M; Walter, N; Johnson-Buck, A. "Ultraspecific analyte detection by direct kinetic fingerprinting of single molecules". TrAC Trends in Analytical Chemistry. 2020, 123 (2), 115764.

signal[67]. Due to the possibilities provided by this variation, biosensors have found attention and usage in a variety of different applications. Environmentalists, for example, have utilized biosensors for detecting and quantifying contaminants in the environment[70]. Clinicians have used them as the basis of assays or medical devices[71, 72]. Given their flexibility, biosensors also possess the capability to be used as diagnostic or analytical tools for cancer biomarkers as well and there is already research that explores this application[73].

Optical biosensors, which utilize light as their transduced signal have been used extensively in single molecule detection[74]. These biosensors typically use fluorescent molecules that can be excited by a laser to release detectable photons or generate a product that naturally fluoresces when imaged. Examples of the former include CRISPR-based methods like SHERLOCK or DETECTR which utilize a fluorescently labeled DNA strand, and examples of the latter include Single Molecule Arrays (SiMoA) which utilize a β-galactosidase reaction that only completes and generates a fluorescent product when the target is present[52, 75, 76]. Optical biosensors also have the option to utilize FRET where a pair of fluorophores are used and the intensity of the signal is distant-dependent[77, 78]. This occurs because when the emission spectrum of one fluorophore, the donor, overlaps with the absorption spectrum of another, the acceptor, and they are sufficiently close, energy from excitation of the donor can be transferred to the acceptor in a distant-dependent fashion. FRET is useful in analytical systems for structural analysis because fluorophores can be placed in such a way that the change in intensity can be correlated to changes in structure where the structural change will shift the placement of the fluorophores resulting in a different distance between them and thus, a different signal[79]. It has been previously used in the Walter lab for example, as a way to study riboswitch function and nanostructures[80-82]. FRET can also be coupled with single molecule techniques to assess the

distribution of behaviors of a molecule through individual, rather than ensemble averaged observation[83, 84].

1.6 Overview of Dissertation

In the following chapters, I will discuss how FRET, single molecule microscopy, and biosensing came together as the basis for a new intramolecular, biosensor-based technique that expanded upon kinetics-based detection built by SiMREPS into a new technology, called intramolecular SiMREPS (iSiMREPS) that was built for accelerated detection, demonstrated its analytical and diagnostic utility, and showed a capacity for multi-target detection.

In Chapter 2, I describe the basic design and foundation of iSiMREPS that utilizes a single molecule FRET (smFRET) biosensor to allow rapid detection through changes in conformation, or state, that are made possible by close proximity of the target and all of the biosensor components. By optimizing the sequence and placement of strand modifications within the biosensor, I demonstrate the feasibility of the technique for nucleic acid detection and by utilizing formamide, the feasibility for particularly rapid detection. The prism-based TIRF (P-TIRF) microscopy methods and preparation that were utilized for this particular chapter are also outlined here.

In chapter 3, I, detail the optimization of this sensor for use as a liquid biopsy assay and demonstrate that it is capable of achieving low femtomolar sensitivity comparable to SiMREPS with only 10 seconds of analysis per FOV. I demonstrate the importance of each optimization for speed, signal-to-noise (S/N), and sensitivity. This chapter also provides a thorough guide to objective-type TIRF (O-TIRF) microscopy imaging, methods, experiment design, and preparation considerations that would become standardized for the utility of this assay. It also

demonstrates the proof-of-concept that will be pivotal for this techniques utility in a clinical setting.

In Chapter 4, I delve into the expansion of iSiMREPS for multi-target detection and demonstrate more thoroughly the design principles and rules that are important when utilizing this technique for multiple targets. I show the multi-target well design and demonstrate that with proper configuration of the wells and of the microscope settings, it is feasible to detect multiple targets with one single imaging run. This will demonstrate iSiMREPS capability to further evolve into a multi-target technique capable of being used as a detection panel in research or the clinic.

These chapters serve to expand the unique utility offered by biosensors towards the detection of DNA and RNA biomarkers relevant for diagnostics and treatment of cancer, establish a new analytical technique that can serve as a research or clinical detection tool, and expand that technique for a multi-target configuration that will allow it more utility when used as a robust product. My thesis serves to apply single molecule microscopy, FRET and the design principles of biosensors towards creating a biosensor-based analytical assay that is capable of detecting nucleic acids at clinically relevant concentrations and is expected to become a basis for the further development of a diagnostic or research tool for the rapid, targeted analysis of DNA and RNA molecules of interest, such as cancer biomarkers.

Chapter 2. Pioneering a Rapid, smFRET-based Biosensor for Nucleic Acid Detection[3,4]

2.1 Introduction: The Rationale and Design of iSiMREPS

iSiMREPS was conceived as a meeting of kinetics-based single molecule detection outlined by SiMREPS, optical biosensing, and a FRET-based probe system. As outlined in section 1.4, SiMREPS achieves two highly desirable qualities for a more specialized, targeted nucleic acid assay: near-perfect specificity that is not limited by probe thermodynamics and SNV discrimination for miRNAs[64]. However, its upper limit on speed is an inherent limitation of its design because an increase in speed requires an increased probability of association of fluorescent probe to surface-bound target. This can only readily be achieved by raising probe concentration which as mentioned above, has an upper limit as this increase also increases the frequency at which unbound probes are near the surface and adds noise to the signal. As such, a different approach that can utilize kinetics-based identification like SiMREPS for specificity while having a design that is not as dependent on diffusion of probes to the surface would offer a significant step forward in designing a sensitive, highly specific and targeted assay for nucleic acids.

[3] This chapter is adapted in part from Mandal, S*; Khanna, K*; Johnson-Buck, A; Walter, N.G. "A guide to accelerated direct digital counting of single nucleic acid molecules by FRET-based intramolecular kinetic fingerprinting", Methods, 2021, In press. and in part from Khanna, K*; Mandal, S*; Blanchard, A.T.; Tewari, M; Johnson-Buck, A; Walter, N.G. "Rapid Kinetic Fingerprinting of Single Nucleic Acid Molecules by a FRET-based Dynamic Nanosensor", Biosensors and Bioelectronics, 2021, 190 113433. *These first two authors contributed equally.

[4] All RNA experiments in this chapter were done by Kunal Khanna. Shankar Mandal and Kunal Khanna both contributed to the writing of this paper and all authors contributed to editing.

Biosensors more broadly offer a way to incorporate the strengths of SiMREPS without its drawback because they can be built to function like nanomachines on the binding of their target molecule[74] and this approach allows for any dynamic behavior of the nanomachine based on the properties of the nucleic acid target to be more directly controllable as it can be adjusted with the design of the machine and has more options to overcome inherent design limitations like SiMREPS reliance on probe diffusion. Additionally, a FRET-based probe system helps in achieving this result as such a probe system, when properly designed, can prevent this unwanted background by requiring the proximity of two fluorophores for a detectable signal which unless they are bound to the same target, will not naturally occur when diffusing in solution. iSiMREPS thus combined all of these designed elements to create an assay that could achieve comparable sensitivity and specificity with much greater speed.

iSiMREPS, as depicted in **Figure 2.1**, is a SMFM, kinetics-based detection technique that uses a DNA-based biosensor that is tethered to the surface, captures its target nucleic acid, and then generates a signal from the switching between high- and low-FRET conformations, or states. This sensor is composed of 3 strands which are called the anchor (A), the capture probe (CP), and the query probe (QP). The anchor in iSiMREPS is biotinylated at one end, which allows it to bind to proteins that have an affinity for biotin binding, such as the avidin family[85]. The anchor as depicted in **Figure 2.1A** binds to a surface-tethered streptavidin protein and has sequences that are complementary to part of both the QP and CP which allows it to be a scaffold for assembly of the sensor on the slide surface. The CP binds to the anchor and utilizes its other free end, which is complementary to the target, to capture it and incorporate it into the biosensor. The CP sequence must have sufficient length and binding affinity to maintain stable capture

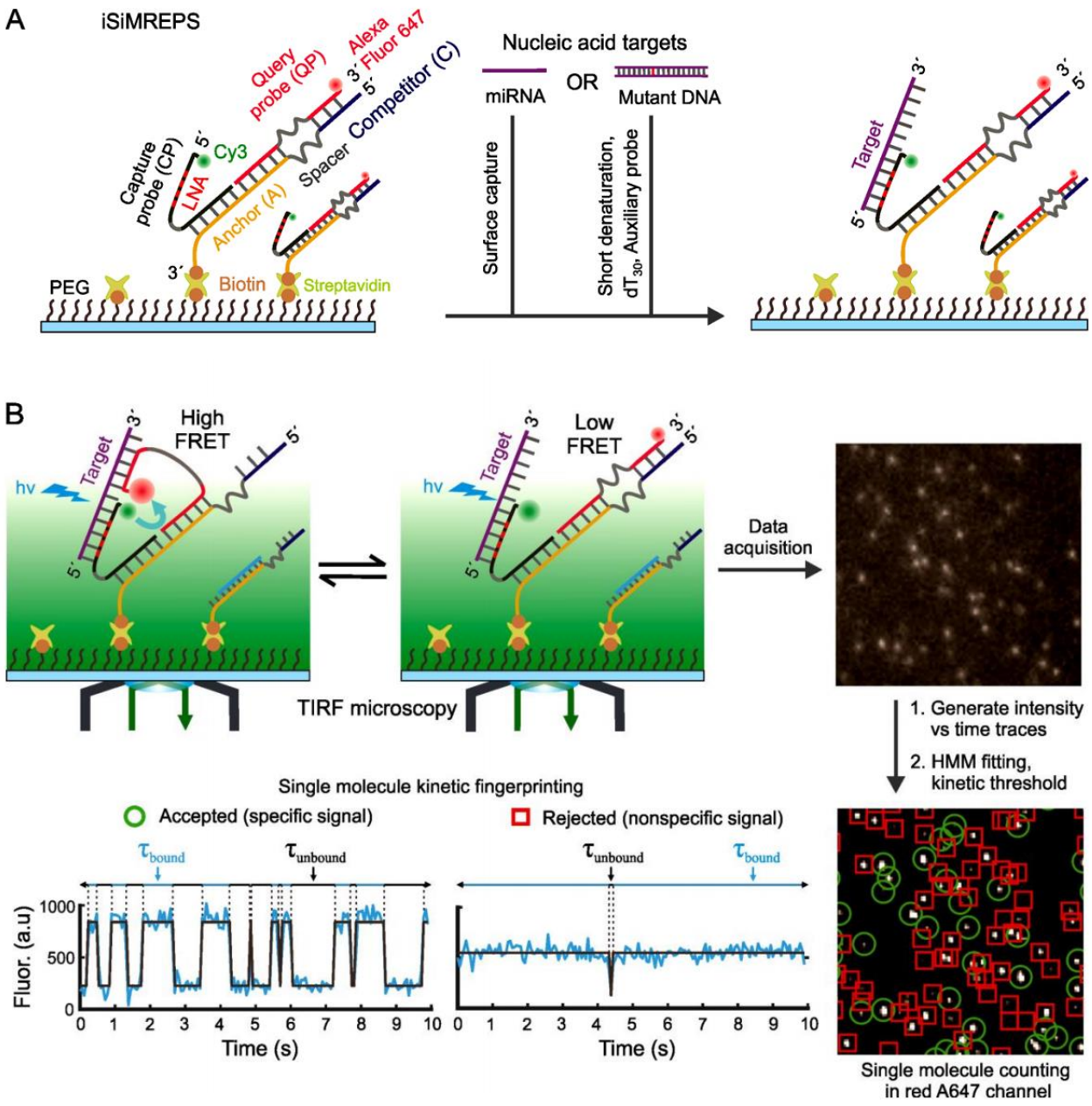

Figure 2.1. Schematic of smFRET-based intramolecular SiMREPS for digital counting of single nucleic acid molecules. (A) Schematic of iSiMREPS sensor assembly and target capture at the surface. iSiMREPS uses a surface immobilized and intramolecularly assembled FRET pair of fluorescent probes for surface tethering and imaging of single nucleic acid molecules. The 5´ Cy3-labeled capture probe contains several LNA residues for high-affinity, stable capturing of target miRNA or mutant DNA molecules. (B) Mechanism of smFRET signal generation and schematic of data acquisition and processing to obtain single molecule kinetic fingerprints. The A647-labeled query probe interacts transiently and reversibly with the target and competitor sequence and generates a single molecule kinetic fingerprint that represents donor (Cy3) or FRET-mediated-acceptor (A647) emission recorded by a TIRF microscope. A representative

field of view (top right corner, not in scale) from TIRF microscopy analyzed with MATLAB programs to identify spots with potential smFRET signals in a field of view (bottom right corner, not to scale) and generate intensity vs time traces (bottom left, cyan). Hidden Markov Model idealization (grey lines) for each intensity vs. time trace and application of kinetic thresholds like the N_{b+d}, dwell times, S/N, and signal intensity distinguishes target-specific signals (green circle) from nonspecific background signals (red rectangle).

when under imaging conditions. The QP also has a free end complementary to bind to another segment of the target sequence and this binding is weak. The CP is labeled with a donor fluorophore, namely Cy3 as depicted here, and the QP is labeled with an acceptor fluorophore, namely Alexa Flor 647 (A647) depicted here. iSiMREPS is designed so that the weakly bound QP will switch between being bound to the target and being bound to a complementary sequence on the anchor called the competitor (C) (**Figure 2.1B**). When the QP is target-bound, the donor and acceptor fluorophores are in close proximity and FRET occurs, with the sensor in a high-FRET state. When it is bound to the competitor, the fluorophores are far apart and there is no FRET behavior observed, with the sensor in a low-FRET state. This generates a signal pattern where you have high fluorescent intensity in the high-FRET state where there is detectable acceptor emission and a low fluorescent intensity in the low-FRET state where no detector emission can be picked up. Just like with SiMREPS before it, the target can be identified by its kinetic fingerprint which is determined primarily by the N_{b+d} between the high- and low-FRET states as well as the dwell times in each state. This identification, as with classical SiMREPS, is assisted by data analysis software which can estimate the N_{b+d} and dwell times and distinguish molecules through filtering based on signal characteristics.

This biosensor configurations affords several advantages that pave the way for rapid nucleic acid detection. Using a biosensor configuration creates a high local concentration of probes at the slide surface which is helpful for eliminating the gaps of time spent without a

bound probe that SiMREPS suffered from. Secondly, this biosensor design allows both states to be directly controllable through modification of the sensor design which grants it additional customizability that can grant it flexibility for different targets as well as the ability to fine tune kinetics towards more desirable behaviors. Since this approach retains the benefits of using kinetics-based detection, I hypothesized that it should be capable of producing the near-perfect specificity of SiMREPS while also gaining much faster analysis speed because of the biosensor configuration. In the remainder of this chapter, the development of the iSiMREPS biosensor design and the proof-of-concept demonstrating its ability to detect a nucleic acid target rapidly is shown as well as all relevant experimental procedures and optimizations necessary to obtain those results.

2.2 Materials and Methods

2.2.1 Materials and Nucleic Acid Strands

All single stranded nucleotides without any locked nucleic acid (LNA) modifications were purchased from IDT (Integrated DNA Technologies, Inc.) with PAGE purification. All A647-labeled QPs were also purchased from IDT and purified via HPLC. CPs were purchased either from Qiagen with a 5' Amino modification usable for subsequent Cy3 labeling via a monoreactive dye pack (GE life sciences, catalog no. PA23001) or labeled with Cy3 directly from IDT with both being HPLC purified. **Table 2.1** below lists all of the nucleic acids used for this chapter. Any relevant melting temperature, or T_m values were calculated using the IDT oligo analyzer at 1 μM nucleic acid and 600 mm Na^+ concentration[86] or the T_m prediction tool from Qiagen if the strands contained LNA[87]. Biotinylated Bovine Serum Albumin (bBSA, 25mg ImmunoPure), Streptavidin (S-888), 10× Phosphate-buffered Saline (PBS, pH 7.2, 70-013-032), Trolox (MFCD00006846), 3,4-dihydroxybenzoate (), and Protocatechuate 3,4-dioxygenase

(PCD, AC218940050) were purchased from Thermo Fisher. Tris base (77-86-1), boric acid (10043-35-3), and disodium EDTA (6381-92-6) were purchased from Sigma-Aldrich. 40% Acrylamide/Bis solutions of 19:1 and 29:1 were purchased from Bio-Rad (Catalog no. 1610146 & 1610154). SYBR Gold was purchased from Thermo-Fisher (S-11494).

ID	Sequence: 5´-3´
miR-141	UAACACUGUCUGGUAAAGAUGG
Capture_miR-141	/5Cy3/C+A+GAC+A+GTGTTATTTGGCGGAGTGTCC
Query_Q_8QS_3_miR-141	CGCGGCCCAGGATTTCCATCTTT/3AlexF647N/
Query_Q_8QS_{18}_miR-141	CGCGGCCCAGGATTTTTTTTTTTTTTTTTCCATCTTT /3AlexF647N/
Query_Q_8QS_{33}_miR-141	CGCGGCCCAGGATTTTTTTTTTTTTT TTTTTTTTTTTTTTTTTTCCATCTTT/3AlexF647N/
Anchor_C_6CS_3_miR-141	TTAGATGGTTTTCCTGGGCCGCGGGACACTCCGCCTTTTTTTT/ 3Bio-TEG/
Anchor_C_7CS_3_miR-141	TTAAGATGGTTTTCCTGGGCCGCGGGACACTCCGCCTTTTTTT T/3Bio-TEG/

Table 2.1. All Oligonuleotides used in Chapter 2. The relevant binding regions for each sequence are underlined.

2.2.2 P-TIRF Microscopy

iSiMREPS requires a TIRF microscope in order to execute single molecule analysis as that ensures only signal from surface-bound probes is recorded which allows for the resolution and S/N necessary for analyzing individual molecules with the technique. In our studies, all experiments were carried out using either a prism-type or objective-type TIRF microscope. This chapter utilizes a P-TIRF microscope based on an Olympus IX-71 frame equipped with a 60× water-immersion objective (Olympus Uplanapo, 1.2NA) with an ICCD (I-Pentamax, Princeton

Instruments) or sCMOS (Hamamatsu C13440-20CU) camera for recording movies. A 640 nm red laser (Coherent CUBE 640-100C, 100 mW) and 532 nm green laser (CrystaLaser CL532-150mW-L) was used at an illumination intensity of ~100W/cm^2 in order to excite Alexa Fluor 647 (A647) and Cy3 fluorophores, respectively in order to execute 2 channel imaging studies. A dichroic mirror with a cut-off wavelength of 610 nm (Chroma) was used to separate the Cy3 and Cy5 emission signals with a full-frame acquisition rate of 10Hz. The Cy3 channel image was passed through a bandpass filter (HQ580/60m, Chroma) and the Cy5 channel was passed through a long-pass filter (HQ655LP, Chroma). This 2 channel setup was ideal for simultaneous observation of both the CP and QP during imaging and a more detailed analysis of changes in both signals.

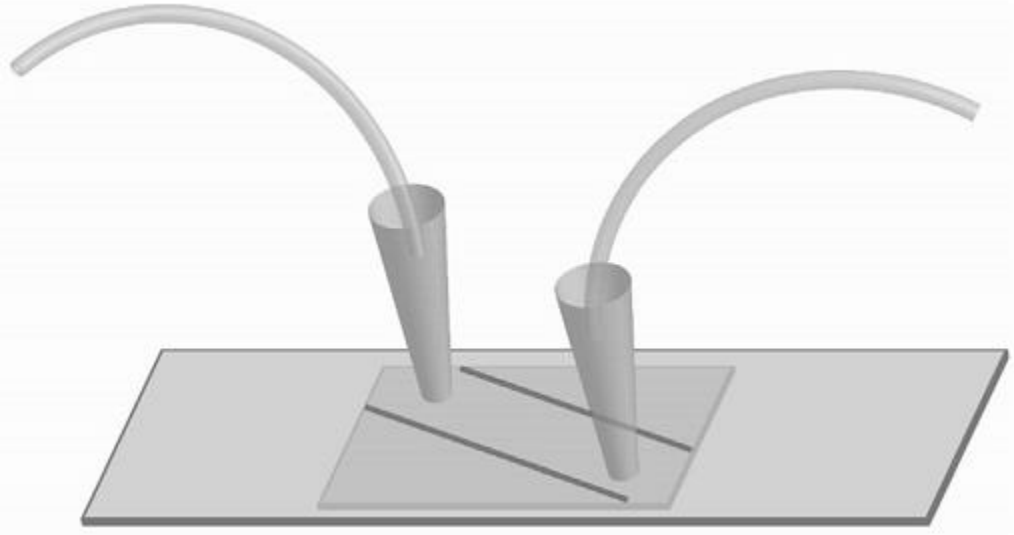

Figure 2.2. P-TIRF Sample Cell. The slide above has 2 holes over which a coverslip is glued around its edges in order to create a sealed chamber. Two cut pipette tips are glued onto each hole along with a piece of Tygon tubing so that sample or buffer can be injected into the chamber and exited out the other hand when in excess or removed when necessary.[5]

[5] This figure is reproduced with permission in part from Chatterjee, T*; Li, Z*; Khanna, K; Montoya, K; Tewari ,M; Walter, N; Johnson-Buck, A. "Ultraspecific analyte detection by direct kinetic fingerprinting of single molecules". TrAC Trends in Analytical Chemistry. 2020, 123 (2), 115764.

2.2.3 Preparation of P-TIRF Sample Cell

iSiMREPS experiments utilize a sample cell that houses a chamber for the imaging solution containing the biosensor and an oxygen scavenger system that protects the fluorophores from oxygen exposure, which hastens photobleaching (**Figure 2.2**). The flow sample cells used for the P-TIRF imaging experiments in this chapter were sandwiched between a microscope slide (fused silica) and glass coverslip (VWR Micro Cover Glasses 22 x 30 mm, catalog no. 48393-026) in a configuration that permitted easy setup of a prism for P-TIRF imaging. Each microscope slide has a hole drilled on each of two ends that together allow for easy introduction and exchange of sample as well as buffer solutions using Tygon tubing (U.S. plastic corporation, 0.020" ID x .060" OD Tygon® ND 100-80, catalog no. 56515) that is connected to the holes. The sample cell is prepared and recycled through a few preparation steps. The preparation beings by gluing the aforementioned coverslip to one side of the slide with the drilled holes near a corner to provide a seal after drying and setting. After this, a pipette tip cut on one end to fit in the hole is glued on the other side of the slide and a piece of Tygon tubing is glued into the other open end to provide a seal that allows for flowing of sample and buffer with a needle.

After the first use, this slide is boiled to remove the glue, coverslip, tips and tubing for further cleaning and reuse. When used for another experiment, it is then subject to a "base piranha" protocol[66, 88]. In this protocol, slide is first carefully rinsed with water and then sonicated in acetone for 10 min. This is followed by sonication in 1 M KOH for 20 min to remove aqueous and organic residues from the surface. Next, the slide or coverslip is treated with "base piranha" solution consists of 14.3% v/v of 28-30 wt% NH_4OH, and 14.3% v/v of 30-35 wt% H_2O_2 that is heated to 70-80 °C for ~45 min. After this is completed, the piranha is disposed of and the slide is again rinsed with water to clear any remaining solution. It is then placed under a Bunsen burner

on both sides briefly to remove any remaining water and impurities that may impede imaging. Once this process is completed, the preparation procedure mentioned above can be used again to ready it for imaging.

2.2.4 P-TIRF Assay Preparation

As outlined in the previous section**,** P-TIRF imaging utilizes the slide sandwich sample cell for sample introduction, buffer exchange, and space above the sample chamber to seat a prism. This cell is first incubated with 150 µL of 1 mg/mL biotinylated Bovine Serum Albumin (bBSA) for 10 min which adsorbs to the slide surface and passivates it with a source of biotin can be used to help tether the biosensor to the slide surface. After passivation is complete, unbound bBSA is washed out with T50 buffer (10 mM Tris-HCl pH 8.0 at 25 °C, 50 mM NaCl) and 1 mg/mL streptavidin is then injected into the chamber and incubated for 10 min where it binds to the biotin on bBSA using 1 of its 4 biotin-binding domains and enables capture and surface tethering of other biotinylated molecules. Any unbound streptavidin is then washed out with 4× PBS (Phosphate-buffered saline, pH 7.4 at 25 °C). iSiMREPS sensors were then assembled at ~200 nM initial concentration in 4× PBS buffer with miR-141 target at a 1.000:1.125:1.125:1.250 ratio for A, CP, QP, and target respectively. This solution was heated at 70 °C for 7 min in a metal bath and then cooled by holding at ambient room temperature for 20-25 min. This solution was then diluted to ~100 pM final concentration and injected into the chamber at 150 µL volume for 10 min incubation to allow surface capture by binding to open streptavidin sites established by prior steps. Finally, a 4× PBS imaging buffer containing an oxygen scavenging system (OSS) made of 1 mM Trolox 5 mM 3,4-dihydroxybenzoate (PCA), and 50 nM protocatechuate dioxygenase (PCD) was added to provide protection from oxygen and the system was ready for imaging.

2.2.5 P-TIRF Imaging

The P-TIRF microscope outlined in **Section 2.2.2.** has 2 channel recording which allows for collection of detailed kinetic information as both donor and acceptor signals can be observed and inspected for FRET-based anti-correlation. Longer acquisition times were beneficial for the P-TIRF imaging studies outlined in this thesis as they allowed for thorough and accurate information on FRET states and kinetic behavior of the iSiMREPS biosensor and the establishing of a much stronger initial demonstration of feasibility. Brief direct excitation of the acceptor at low power (~3 mW) at the beginning and end of the imaging time window was helpful in selecting high quality traces to evaluate biosensor kinetics (See **Section 2.2.6** for more details). Additionally, a bead slide was imaged prior to the sample because a short movie with easily identified spots in both channels was necessary to allow the data processing software to effectively pair signals from the same molecule in both channels when processing FRET movies. When ready, the cell was placed on the objective with a prism seated above the sample chamber, focused, and imaged. The signal integration time (exposure time) per frame was 100 ms, and up to 9000 movie frames were acquired per FOV as needed to obtain detailed kinetic information.

2.2.6 Processing and Analysis of P-TIRF data

P-TIRF data analysis utilizes MATLAB scripts and software to identify spots of high fluorescence, map out spots in both channels, process signals from both channels for each molecule, and manually select traces that show FRET signal which can be saved and further analyzed for kinetic information. Firstly, a MATLAB script was used to find regions with intensity higher than background in one or both detection channels, to use the bead map movies to pair these regions with the corresponding regions of the other channel, and then generate two-channel (donor-acceptor) time-intensity traces. The traces were then manually viewed and selected based on

demonstration of FRET behavior. Consistent selection criteria to choose traces with clear, readily interpretable kinetic behavior for the target is was established to ensure high data quality and accurate representation of iSiMREPS biosensor kinetics. The criteria used for the manual trace picking with their respective rationales are listed in **Table 2.2**. Once the traces were selected, several MATLAB scripts were used to clean up and organize the selected traces' data. That cleaned data was placed into the software QuB[89] where each trace was fitted to a 2-state Hidden Markov Modeling (HMM) to determine the FRET state the sensor was in at a given time, idealized and then saved with detailed data. These idealized traces were then further processed with additional MALTAB scripts to generate transition occupancy density plots (TODPs) that gave detailed information about FRET transition behavior across all traces, and to extract the dwell times for each event that occurred for both FRET states[90]. This information was used to evaluate whether or not a particular biosensor was capable of the necessary analytical performance.

Criterion	**Rationale**
Clear anti-correlation in donor and acceptor signal when FRET states switch	In genuine FRET, only one signal is active at a time and it always decreases while the other increases when states switch.
Acceptor signal is present	Filters out traces with a bleached acceptor or no QP.
No multistep transitions	It is hard to distinguish genuine FRET transitions from noise in such traces
No signal drifting into the baseline	Worsening S/N renders some FRET states indistinguishable from noise
Very low high-FRET or very high low-FRET values and very weak S/N	These traces are susceptible to incorrect FRET assignments in HMM modeling
Only the longest segment or the one with the best S/N is chosen	Prevents data bias by a few traces with a large number of transitions

Low-FRET last events in segment accepted only if acceptor is present after that event.	Prevents acceptor photobleaching from tainting kinetic data
Traces must have distinction between signal and baseline	A static signal and an unusually intense baseline cannot be distinguished

Table 2.2. Selection criteria for P-TIRF traces with rationales

2.2.7 Determination of Average Dwell Times

A MATLAB script (version 2019a or later) was used to first place the data into bins ranging from the minimum to maximum dwell time that are incremented by the length of the camera exposure. It then calculates the cumulative frequency of the range of dwell times in the data and fit it with a single- (*Equation 1*) or double-exponential (*Equation 2*) function.

$$y = ae^{-x/\tau} + c \quad (1)$$

$$y = ae^{-x/\tau 1} + be^{-x/\tau 2} + c \quad (2)$$

The variables a, b, c, τ, $\tau 1$ and $\tau 2$ are the fit parameters. The coefficients a and b provide the weight or influence of their population of molecules in the double-exponential. The coefficient τ describes the average event dwell time for the single-exponential function. The coefficients $\tau 1$ and $\tau 2$ describe the average event dwell times for shorter- and longer-lived populations of events, respectively. The coefficient c is a constant that gives the y-intercept for the equation. The sum squared error (sse) and R^2 values for the fit, which describe the residuals or deviation from the fit and goodness-of-fit, respectively, are used to decide whether a single- or double-exponential fitting is best used. At an sse < 0.05 and $R^2 > 0.98$ for miR-141 detection, a single-exponential was considered a good fit and used. When this criterion was not met, a double-exponential fit was used. The average dwell time for double-exponential fits was calculated as $\tau = (a\tau 1 + b\tau 2)/(a +$

b). This equation calculates a weighted average of both populations that was reported as the average dwell time for the entire dataset.

2.2.8 Gel Electrophoresis Characterizations

Polyacrylamide Gel Electrophoresis (PAGE) was run to help in evaluating the binding and structural integrity of iSiMREPS biosensors. Gels were run at 175V for 60-90 minutes using a gel solution that was 17% polyacrylamide. The samples were prepared in 4× PBS buffer containing 10% glycerol and 5 µL of sample were inserted into their respective lanes. These gels were then imagined using the GE Amersham Typhoon imager on the Cy3 and Cy5 settings to obtain images of Cy3- or A647-labeled strands and the biosensors which contained these strands. Optionally, some gels were stained after Cy3 and Cy5 imaging with 1× SYBR gold to image strands without fluorophores.

Figure 2.3. iSiMREPS design for the detection of miR-141 with the capture probe, query probe, competitor, and query spacer depicted. The underlined residues contain LNA modifications to improve binding stability that allows for improved target capture. The competitor and query spacer length vary as indicated in the figure for the design experiments and the exact sequences for all strands can be found in **Table 2.1**.

2.3 Developing and Establishing the iSiMREPS Design

The first iSiMREPS biosensors were designed with miR-141, a promising miRNA for prostate cancer detection[40, 41], as the target (**Figure 2.3**). The naming convention used for these biosensors is described as $Q_aC_bQS_cCS_d$ where each number is a coefficient representing the number of nucleotides in that sequence and Q, C, QS, and CS represent the query-target binding sequence, competitor sequence, query spacer sequence length, and the length of the spacer near the competitor (CS) respectively. CS is omitted from biosensor names in this chapter as it is always CS_3 for miR-141 biosensors and does not vary. The first biosensors tested were $Q_8C_{6,7}QS_3$. The CP was designed to have a higher melting temperature (T_m, 45.3ºC) for a strong, stable capture of the target and the QP was designed to have a T_m closer to room temperature (30.2ºC) to allow for binding and dissociation to occur regularly so that a kinetic fingerprint could be readily generated. The competitor length was varied to evaluate if it offered improvement in kinetic fingerprint generation, improved analysis speed, and to ascertain which length translated into relative parity between high- and low-FRET states when generating the fingerprint. This parity was necessary for designing a good sensor as transitions are necessary for the signal to be differentiated from noise (**Figure 2.1B**) and a biosensor without parity between states will not transition frequently enough to generate a usable fingerprint. These initial lengths were chosen on the basis that they offered similar binding affinity as the QP-target binding and accounted for the low-FRET being an easier conformation to access due to it not requiring significant bending of the QP strand. The QS was designed to be a 3 nt stretch as even such a short length is above the persistence length for oligonucleotide polymers and would not impede its flexibility in switching between states[91]. I hypothesized that this design, combined with the intramolecular biosensor design localizing the

probes, should have sufficient flexibility, binding stability, and parity between states to achieve rapid kinetic fingerprint generation for miR-141.

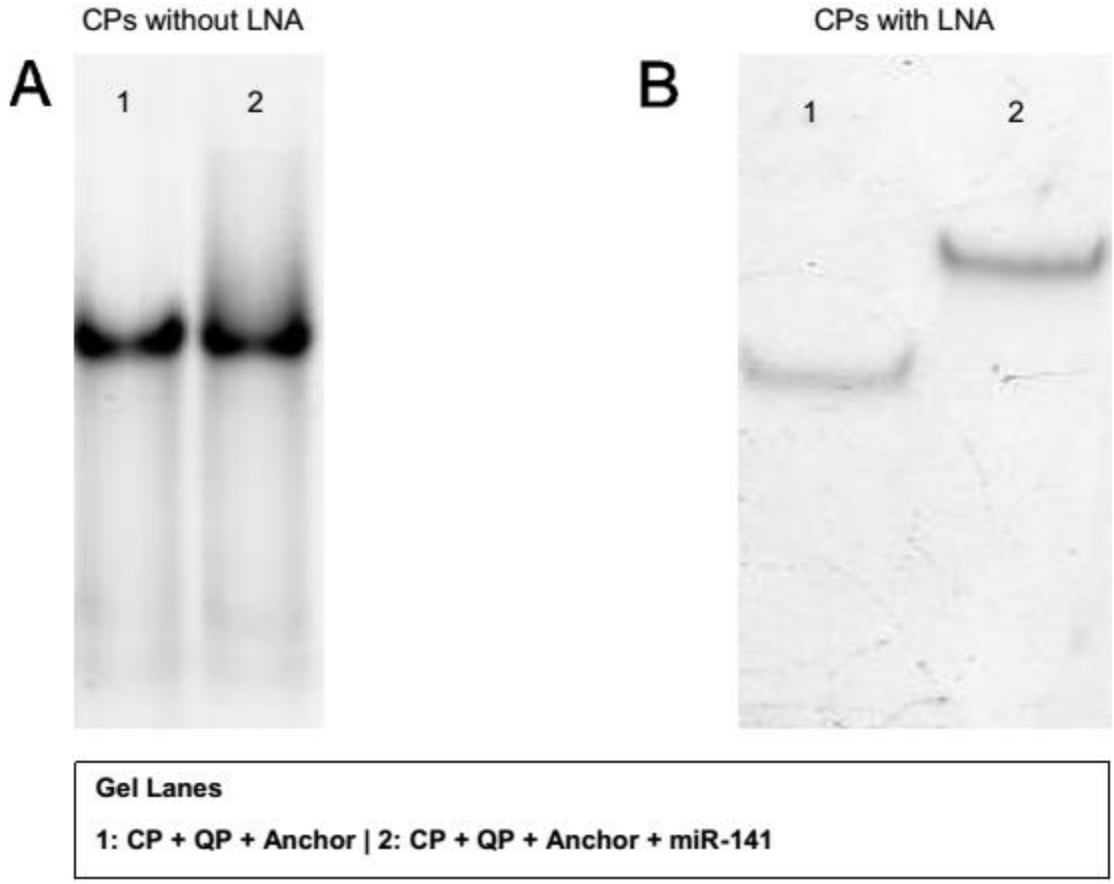

Figure 2.4. Non-denaturing page gels for $Q_8C_7QS_3$. For both panels, the lane on the left has the anchor, capture probe, and query probe added without miR-141 while the lane on the right has all 3 biosensor strands with miR-141. (A) Without LNA-modified capture probe. (B) With LNA-modified capture probe.

To evaluate the assembly of the biosensor, a non-denaturing polyacrylamide gel was run with lanes for each individual strand of the biosensor, miR-141, and then all the strands assembled into a biosensor in the presence and absence of miR-141. As shown in **Figure 2.4A,** the biosensor components effectively assembled as noted by the crisp, defined shape of the band with all of them together. However, the target capture was not sufficiently strong for stable fingerprint generation as noted by the smeared band when miR-141 was added to the rest of the sensor. This result was

corroborated by an inability to collect any FRET signal when imaged under the microscope. To correct this issue, a new CP was designed so that the CP-target binding region would have several LNA residues, which are known to raise the melting temperature of duplexes[92], that would strengthen the CP-target binding and permit more effective target capture. The new CP had a T_m of 73 ºC and was successful in stably capturing target as demonstrated by the sharp, crisp band for the biosensor with RNA and an LNA-containing CP (**Figure 2.4B)**.

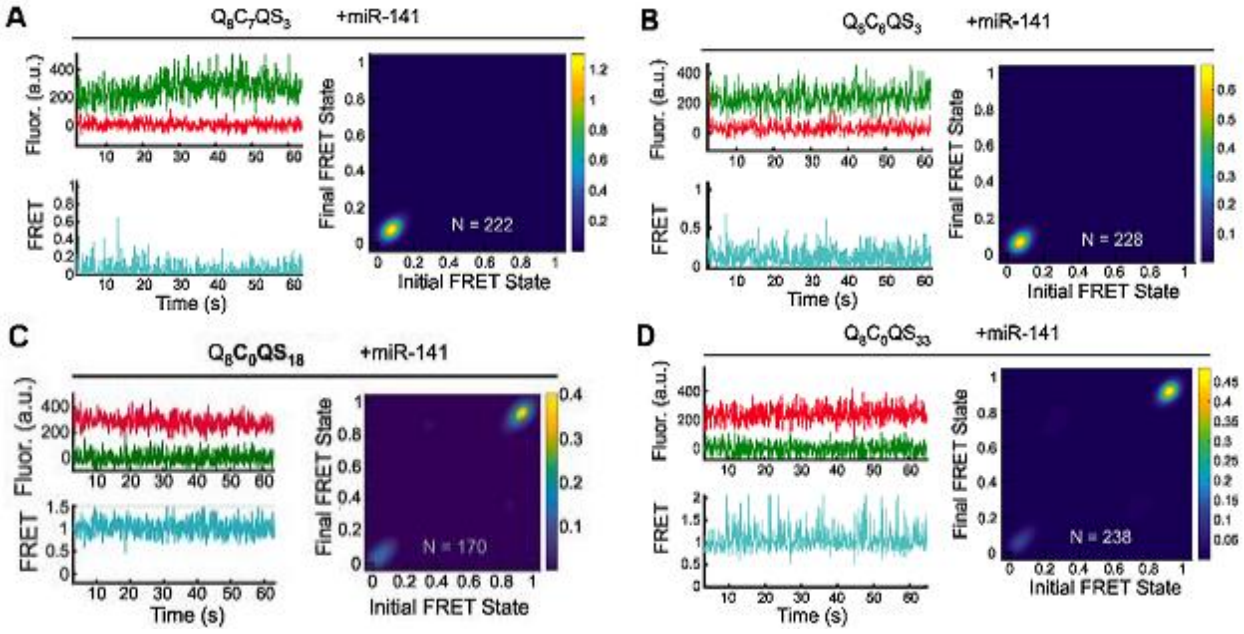

Figure 2.5. Transition occupancy density plots for initial iSiMREPS biosensors with competitor and 2 without any competitor to show FRET state distribution. (A) $Q_8C_7QS_3$ (B) $Q_8C_6QS_3$ (C) $Q_8C_0QS_{18}$ (D) $Q_8C_0QS_{33}$

The two biosensors as outlined previously with variable competitor lengths and LNA-modified CPs were then evaluated for their kinetic behavior and target identification. The biosensors with a competitor did not show any FRET signal and show only a static low-FRET state (**Figure 2.5A-B**). Three additional biosensors $Q_8C_0QS_{3,18,33}$ were also tested to evaluate if this design was capable of assuming a high FRET state without a competing interaction. When the competitor was removed there was a domination of static high-FRET signals without any

transitions between states (**Figure 2.5C-D**). These results indicated that the sensor was capable of assuming a high-FRET state as it was able to achieve it without the competitor. However, the results also demonstrated that the biosensor was not usable in its current design because the QP-competitor interaction was far more favorable than the QP-target interaction as indicated by the low-FRET state dominance of those designs. Additionally, this problem could not be solved by just removing the competitor as the results indicate that this translates to a dominance of the high-FRET state. This prompted evaluation of the structural assembly through using NUPACK[93, 94] modeling. This modeling confirmed that these designs do not assume the high-FRET conformation and that lengthening the QS shifts the biosensor further towards that conformation with an 18 and 33 nt QS providing better parity according to the model for 6- and 7 nt competitor lengths respectively. The modeling information suggests that this result could not be readily predicted by QP-target or QP-competitor interactions (**Table 2.3**) where the ΔG values are consistent despite the varying QS length predicted to have a different result.

Sensor ID	Complementary (bp)		ΔG (kcal/mol)		T_m (°C)	
	Q-T	Q-C	Q-T	Q-C	Q-T	Q-C
$Q_8C_6QS_{18}$	8	6	-13.56	-9.67	30.2	7.5
$Q_8C_6QS_{33}$	8	6	-13.56	-9.67	30.2	7.5
$Q_8C_7QS_{18}$	8	7	-13.56	-11.62	30.2	18.1
$Q_8C_7QS_{33}$	8	7	-13.56	-11.62	30.2	18.1

Table 2.3. The free energy (ΔG) and melting temperature (Tm) of query-target (Q-T) and query-competitor (Q-C) duplexes in different iSiMREPS sensors used for detection of miR-141. ΔG and T_m were calculated using IDT oligo analyzer[86] as outlined in **Section 2.2.1** using the complementary segments that form the duplex.

The four biosensors $Q_8C_{6,7}QS_{18,33}$ were then evaluated for the same kinetic behavior and target identification utilizing dwell time data and both TODP plots. The dwell time data was

calculated as described in **Section 2.2.7** and shown in **Figure 2.6**, which was unavailable for previous designs due to their lack of dynamic behavior. The TODP plots were used to evaluate FRET state distribution for parity as shown in **Figure 2.7**.

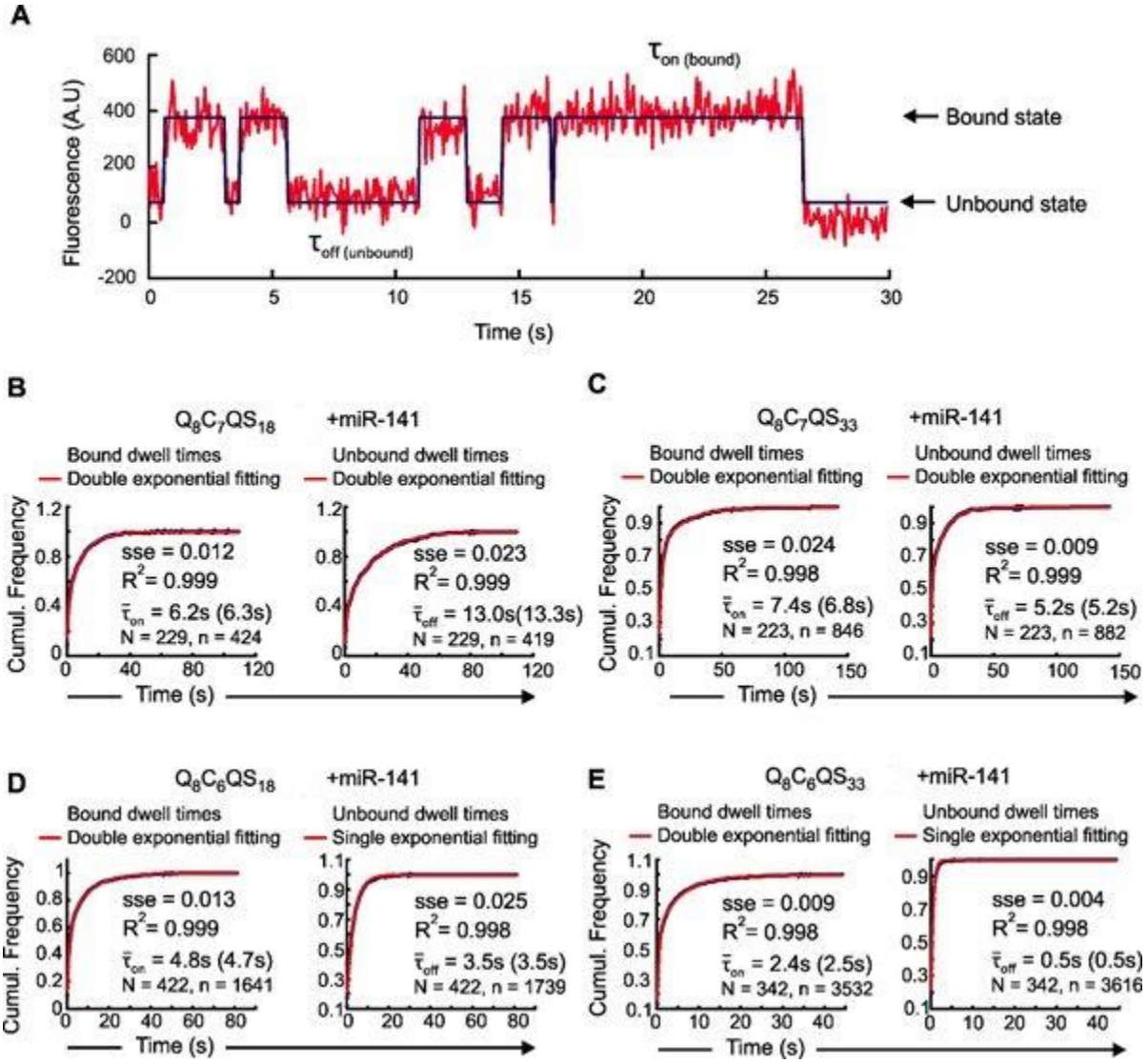

Figure 2.6. Representative single molecule kinetic trace and estimation of average dwell times of FRET states for different iSiMREPS sensors for detecting miR-141. (**A**) Representative intensity-time trace fitted with tan HMM to extract the dwell times of miR-141 target bound ($\bar{\tau}_{on}$) and unbound states ($\bar{\tau}_{off}$). (**B-E**) Exponential fitting to dwell time cumulative frequency for miR-141 target bound (high-FERT) ($\bar{\tau}_{on}$) and non-target-bound (low-FRET) ($\bar{\tau}_{off}$) states for various sensors. All experiments were performed without formamide in the imaging buffer. Single exponential fitting was chosen when sum squared error (sse) <0.05 and $R^2 > 0.98$ and double exponential fitting was used otherwise. The time listed reflects the dwell time calculated from the best-fit curve using all accepted traces, and the time in parenthesis is the reported average when the data was split into

3 populations and is the one seen in the main text. The 'N' represents number of accepted traces, and 'n' represents the total number of dwell time events used for the fitting.

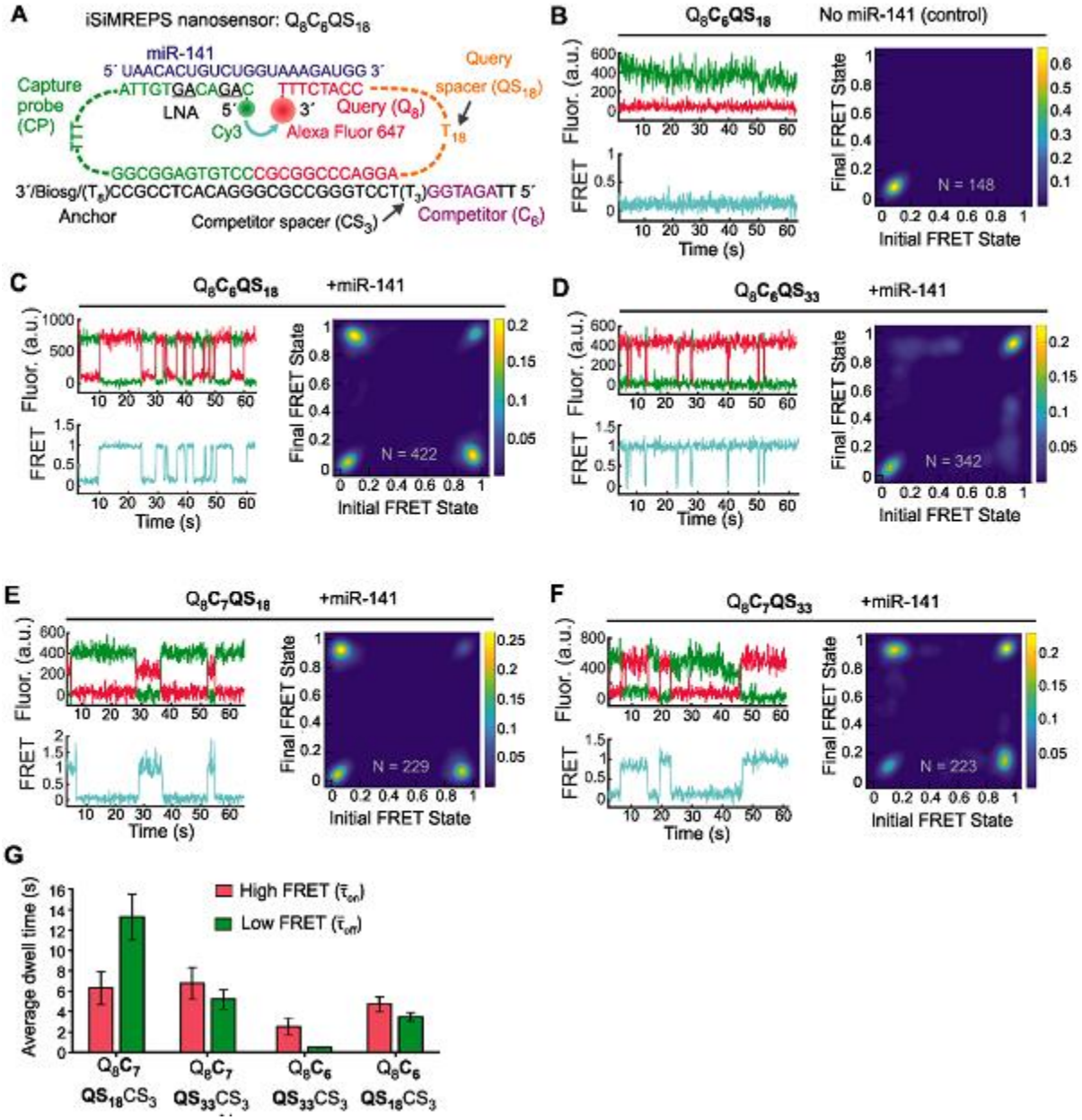

Figure 2.7. Design and optimization of iSiMREPS for detection of a miRNA. (**A**) Design of the optimized $Q_8C_6QS_{18}$ smFRET-based iSiMREPS sensor for detection of miR-141. The CP stably binds with the miRNA target with the assistance of locked nucleic acid residues (black and underlined) that increase the stability of the DNA-RNA duplex. The query (8 nt) switches between being bound to the 8 nt overhang of the target or to a 6 nt competitor sequence that extends from the anchor, resulting in dynamic kinetic smFRET fingerprints. (**B-F**) TODP plots and representative traces for different iSiMREPS sensor designs that have fixed query (8 nt), varying competitor (6 and 7 nt), and varying query spacer (3, 18 and 33 nt) lengths in the presence of miR-141, as well as control without miR-141. The smFRET dynamics of each sensor

is indicated. (**G**) The average dwell times of the high-FRET ($\bar{\tau}_{on}$) (red) and low-FRET ($\bar{\tau}_{off}$) (green) interactions for each sensor design. All data are presented as mean ± s.d., where n = 3 populations of a split data set for each condition.

Among the four candidate biosensors, $Q_8C_7QS_{18}$ and $Q_8C_6QS_{33}$ demonstrated a significant bias for low- and high-FRET respectively (**Figure 2.7D-E**). This was further demonstrated by the average dwell times for the high-FRET ($\bar{\tau}_{on}$) and low-FRET ($\bar{\tau}_{off}$) states where $Q_8C_7QS_{18}$ had a $\bar{\tau}_{on}$ of 6.3 ±1.6 s and $\bar{\tau}_{off}$ of 13.3 ±2.2 s and $Q_8C_6QS_{33}$ had a $\bar{\tau}_{on}$ of 2.5 ±0.8 s and $\bar{\tau}_{off}$ of 0.5 ±0.1 s (**Figure 2.6B, 2.6E, and 2.7G**). By contrast, $Q_8C_7QS_{33}$ and $Q_8C_6QS_{18}$ showed a much more parity between FRET states (**Figure 2.7C and 2.7F**) and this was reflected in their dwell times where $Q_8C_7QS_{33}$ had a $\bar{\tau}_{on}$ of 6.8 ±1.6 s and $\bar{\tau}_{off}$ of 5.2 ±0.9 s and $Q_8C_6QS_{18}$ had a $\bar{\tau}_{on}$ of 4.7 ±0.7 s and $\bar{\tau}_{off}$ of 3.5 ±0.4 s (**Figure 2.6C-D and 2.7G**). Based on the results, the dwell times and FRET distribution generally shifted in favor of the high FRET state as the QS length increased and this is reflected both in the changes of the TODP plot and the average dwell time values of the QS_{18} vs QS_{33} biosensors for both C_6 and C_7 designs as the QS length was increased (**Figures 2.5 and 2.7**). This can be explained by the increased length of the QS providing sufficient conformational flexibility for the QP to make contact with the target and this increased length increasing the entropic cost of the QP-competitor interaction. It also confirms that the ΔG value between the QP-target and QP-competitor interaction does not predict behavior alone (**Table 2.3**). Monte-Carlo simulation that evaluated the biosensor structural dynamics is outlined in **Section 3.3.2** which offers greater insight into the observed behavior seen here. $Q_8C_6QS_{18}$ was chosen as the final design because it offered the necessary parity between both FRET states to generate a distinct fingerprint and a shorter average dwell time for both states and was cheaper due to the shorter QP when compared to $Q_8C_7QS_{33}$. This design was chosen as the standard as it was hypothesized that

a change in the complementary nucleotides for the biosensor strands and positioning of base pairs would suffice to adapt this technique to multiple targets.

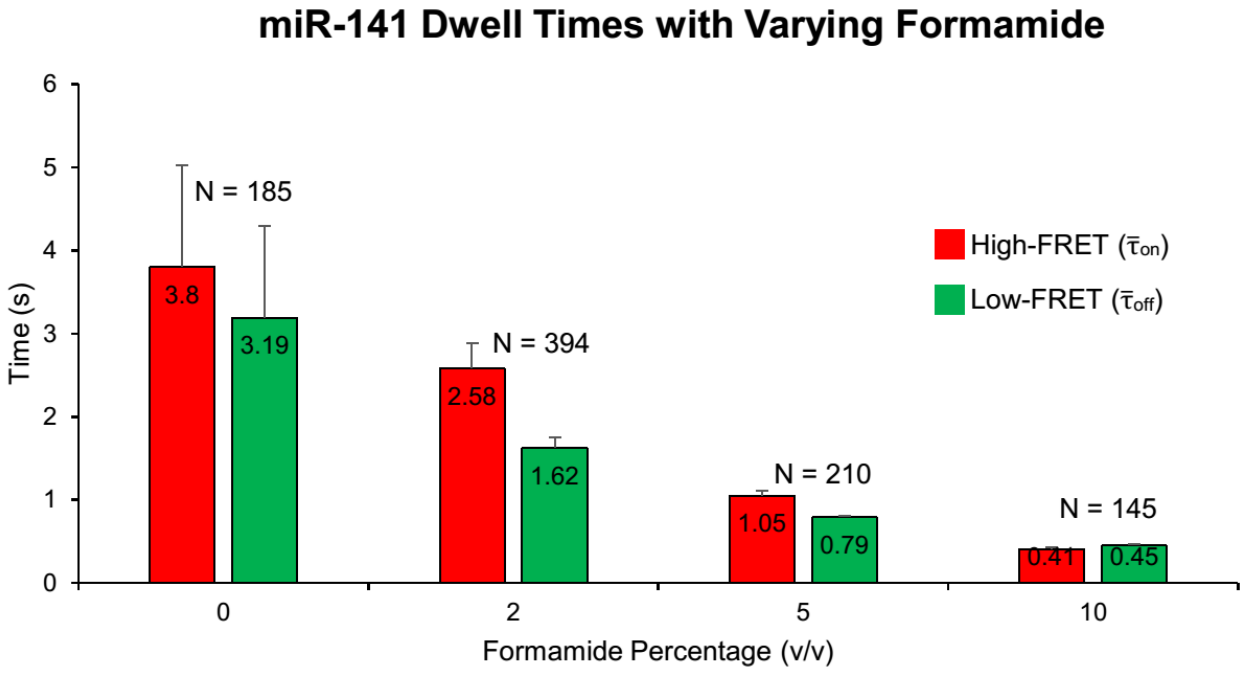

Figure 2.8. Dwell time data for the $Q_8C_6QS_{18}$ biosensor for miR-141 with the v/v% of formamide varied from 0-10%. The graphs show both high-FRET (Red) and low-FRET (Green) states. The total number of traces considered for the dwell times, N, is shown above the dwell time values. All data are presented as mean ± s.d., where n = 3 populations of the total number split into 3 data sets.

Once the iSiMREPS design was chosen, the next step was optimizing the assay for speed. This would necessitate reducing the dwell times in both conformations without distributing the FRET state parity established in the standardized design. One way this was possible was by reducing the number of base pairs in the query-target and query-competitor duplexes. However, this has the undesirable consequence of reducing the specificity of this interaction and thus limiting the general applicability of the technique. Additionally, such an approach would require additional design work in order to preserve FRET state parity. Another, potentially simpler route, is to use a denaturant which can reduce duplex stability in general and will thus act on both duplexes.

Formamide was chosen for this route because it is known to reduce the melting temperature of nucleic acid duplexes of ~2.4-2.9 °C /mol L^{-1} depending on the GC content, helix conformation and hydration state[95]. This biosensor was then tested at 0, 2, 5, and 10% v/v formamide in the imaging buffer to evaluate its effect on the high- and low-FRET state dwell times as well as binding stability. It showed a decrease in the dwell times for both states as expected as the formamide percentage increased and did not show a measurable loss in stability (**Figure 2.8**). Additionally, the dwell times were reduced to <1s at 10% formamide which provided a possibility of achieving detection with a time window on a scale of seconds as opposed to 10 minutes per FOV as it was for classical SiMREPS.

2.4 Discussion and Summary

In this chapter, the proof-of-concept for iSiMREPS was demonstrated. It was possible to successfully combine the kinetics-based detection of SiMREPS with the customizability of a biosensor and a FRET signal design to detect miR-141 at a significantly faster speed than classical SiMREPS. The high local concentration of probes achieved its intended effect in removing the dependency on high probe concentrations to increase speed by eliminating the long gaps of time spent without a probe bound to target. Additionally, iSiMREPS benefitted from the biosensor design as placing both high- and low-FRET conformations under direct control permitted the dwell times to be more readily customized as noted by the different performances of the various designs and the acceleration of fingerprinting by formamide was possible because both dwell times are directly dictated by a different duplex formed per conformation. Insight was also obtained into the fundamentals that go into designing a good biosensor including a strong capture, a sufficiently long QS to obtain necessary flexibility for both conformations, and the correct sequence content and length to get parity between FRET states which gives the most distinct kinetic fingerprint for

detection. The $Q_8C_7QS_{18}$ biosensor demonstrated all of these qualities and was amenable to acceleration through formamide, making it an ideal choice to standardize for further studies.

Chapter 3. Rapid Kinetic Fingerprinting of Single Nucleic Acid Molecules by a FRET-based Dynamic Nanosensor[6,7]

3.1 Introduction: Moving Towards iSiMREPS Assay Development

iSiMREPS, as established in the previous chapter, demonstrated the ability to detect nucleic acids with the same near-perfect specificity offered by SiMREPS at a significantly faster analysis speed than SiMREPS[64]. However, iSiMREPS required further development, optimization, and demonstration on multiple targets to truly reach its full potential as a liquid biopsy assay. To achieve this, iSiMREPS needed a limit of detection (LOD) and linear dynamic range (LDR) suitable for its target nucleic acids and optimizations and best practices that achieve these analytical benchmarks and allow the technique to reproduce them consistently. Additionally, demonstration of its utility beyond miR-141 was necessary. To this end, a LOD in the lower femtomolar range was desirable as it is a typical range for lower-abundance miRNA targets[45] and adding *EGFR* exon 19 deletion mutant (*EGFR*Δ_{exon_19}) as an additional target would demonstrate its more general applicability. This chapter will address iSiMREPS' development into a full assay including transitioning from P-TIRF microscopy to objective-TIRF (O-TIRF),

[6] This chapter was reproduced in part from Khanna, K*; Mandal, S*; Blanchard, A.T.; Tewari, M; Johnson-Buck, A; Walter, N.G. "Rapid Kinetic Fingerprinting of Single Nucleic Acid Molecules by a FRET-based Dynamic Nanosensor", Biosensors and Bioelectronics, 2021, 190 113433. *The first two authors contributed equally.

[7] Kunal Khanna performed all early development and optimization experiments on RNA as well as RNA quantification experiments. Shankar Mandal performed all DNA experiments and assisted with collecting RNA quantification data. Both Shankar Mandal and Kunal Khanna performed various optimization experiments and contributed to the writing and editing of the manuscript. Aaron Blanchard performed the Monte-Carlo simulation. All other authors aided in editing and revision of the manuscript and offered advice or input on experiment design.

optimizing the preparation and protocol for an O-TIRF-based assay, improving sensitivity to obtain the desired LOD through best practices and the use of toehold-mediated strand displacement (TMSD) to improve signal-to-noise (S/N), and demonstrating proof-of-concept for both miR-141 and *EGFR*Δ_{exon_19}.

3.2 Methods

3.2.1 Materials and Nucleic Acids

All nucleic acid strands used in this chapter are those mentioned in **Section 2.2.1** and **Table 2.1** as well as new strands used in this chapter as highlighted in **Table 3.1** below. Any T_m values in this chapter were determined as outlined in **Section 2.2.1**. Capture probes containing LNA and pre-labeled with A488 were purchased from IDT with HPLC purification. The chemicals and other materials mentioned in **Section 2.2.1** were also used here and the PEG preparation chemicals are all mentioned in Section **3.2.2** with their sources.

ID	Sequence: 5´-3´	Usage
CI_{mis} for miR-141	TCCGCCATATAACACTGTCTG	Removes capture probe from non-target-bound sensor. Sequence has mismatch in area that binds to capture linker.
CI_{full} for miR-141	TCCGCCAAATAACACTGTCTG	Removes capture probe from non-target-bound sensor. Sequence is fully complementary to its

		target on the capture probe.
QI for miR-141	GAGTGTCCCGCGGCCCAGGA	Removes query probe from non-target-bound sensor
Capture_ Exon 19	/5AmMC6/AG+CG+ACG+GG+AATTTGGCGGAG TGTCC	All sensors
Query_Q_8QS_{18}_Exon 19	CGCGGCCCAGGATTTTTTTTTTTTTTTTTATG TTTTG/3AlexF647N/	All sensors with Q_8QS_{18}
Anchor_C_6CS_4_Exon 19	TTAAACATCTTTTCCTGGGCCGCGGGACACTC CGCCTTTTTTTT/3Bio-TEG/	Sensor $Q_8C_6QS_{18}CS_4$
Anchor_C_6CS_{12}_Exon 19	TTAAACATCTTTTTTTTTTTTCCTGGGCGCGGG ACACTCCGCCTTTTTTTT/3Bio-TEG/	Sensor $Q_8C_6QS_{18}CS_{12}$
Anchor_C_6CS_{19}_Exon 19	TTAAACATCTTTTTTTTTTTTTTTTTTTCCTGGG CCGCGGGACACTCCGCCTTTTTTTT/3Bio-TEG/	Sensor $Q_8C_6QS_{18}CS_{19}$
Anchor_C_7CS_{19}_Exon 19	TTAAAACATCTTTTTTTTTTTTTTTTTTTCCTGG GCCGCGGGACACTCCGCCTTTTTTTT/3Bio-TEG/	Sensor $Q_8C_7QS_{18}CS_{19}$
Anchor_C_8CS_{19}_Exon 19	TTACAAACATCTTTTTTTTTTTTTTTTTTTCCTG GGCCGCGGGACACTCCGCCTTTTTTTT/3Bio-TEG/	Sensor $Q_8C_8QS_{18}CS_{19}$
EGFR exon 19 del MUT_ FW	TTCCCGTCGCTATCAAGACATCTCCGAAAGCC AACAAGTAGGAC	FW and Rev strands were annealed to prepare dsDNA. FW strand was detected
EGFR exon 19 del MUT_Rev	GTCCTACTTGTTGGCTTTCGGAGATGTCTTGA TAGCGACGGGAA	
EGFR exon 19 WT_FW	TTCCCGTCGCTATCAAGGAATTAAGAGAAGC AACATCTCCGAAAGCCAACAAGTAGGAC	

EGFR exon 19 WT_Rev	GTCCTACTTGTTGGCTTTCGGAGATGTTGCTT CTCTTAATTCCTTGATAGCGACGGGAA	FW and Rev strands were annealed to prepare dsDNA. FW strand was detected
CI_{20}_Exon 19	TCCGCCAAATTCCCGTCGCT	Removes non-target-bound capture probe
CI_{15}_Exon 19	ACTCCGCCAAATTCC	Removes non-target-bound capture probe
CI_{17}	ACTCCGCCATATTCCCG	Removes non-target-bound capture probe
CI_{18}	ACTCCGCCTTTTTCCCGT	Removes non-target-bound capture probe
CI_{22}	ACTCCGCCATATTCCCGTCGCT	Removes non-target-bound capture probe
QI	GAGTGTCCCGCGGCCCAGGA	Removes non-target-bound query probe

Table 3.1. All strands used for *EGFR*Δ_{exon_19} experiments and any new strands used for miR-141 experiments for Chapter 3 in addition to those listed in **Table 2.1**.

3.2.2 O-TIRF Microscope & Imaging

iSiMREPS experiments in this chapter were performed using an O-TIRF setup that meets the same requirements outlined in **Section 2.2.2**. This setup uses an Olympus IX-81 objective-type TIRF microscope equipped with a 60× oil-immersion objective (APON 60XOTIRF, 1.49 NA) with CellTIRF and z-drift control modules. An ICCD (I-Pentamax, Princeton Instruments, MCP Gain 60) or sCMOS (Hamamatsu C13440-20CU) camera was used to record movies for the prism-TIRF while an EMCCD camera (IXon 897, Andor, EM gain 150) was used for the objective-TIRF. For recording smFRET signal, the Cy3-Alexa Fluor 647 fluorophore pairs were excited by light from a 532 nm laser at a power of 15–30 mW. For reliably detecting FRET

signals with satisfactory S/N, an illumination intensity of ~50 W/cm^2 is typically used, and the TIRF angle adjusted to achieve a calculated evanescent field penetration depth of ~70-85 nm. The exposure time per frame was 60-100 ms, and typically 200-600 movie frames were acquired per FOV.

3.2.3 O-TIRF Sample Cell Preparation

O-TIRF experiments utilized a coverslip with cut pipette tip wells glued to it as the sample cell (**Figure 3.1**). O-TIRF coverslips and imaging cells were prepared by following three

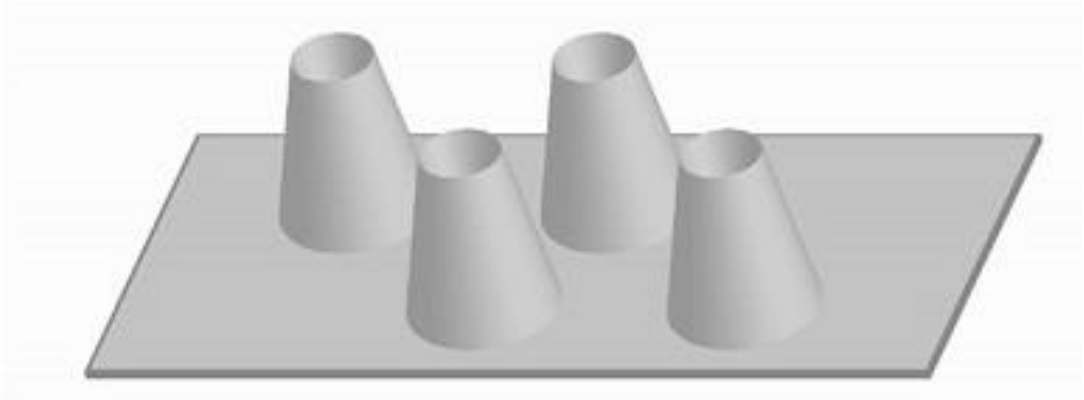

Figure 3.1. O-TIRF Sample Cell. The slide above has 4 cut pipette tips that are glued in place to form wells that sample can be pipetted in and out of. This design is suitable for O-TIRF microscopy since a PRISM is not needed and the height and reduced surface area within the wells allow for greater concentration of molecules and higher sensitivity.[8]

basic steps: cleaning the coverslip to remove organic residues from surface, passivating the surface with affinity tags, and preparing the sample cells by attaching cut pipette tips as described in previous works[56, 66]. To summarize, VWR No. 1.5, 24×50 mm coverslips (VWR, catalog no. 48393-241) were cleaned following either one of two procedures. In one cleaning

[8] This figure is reproduced in part from Chatterjee, T*; Li, Z*; Khanna, K; Montoya, K; Tewari ,M; Walter, N; Johnson-Buck, A. "Ultraspecific analyte detection by direct kinetic fingerprinting of single molecules". TrAC Trends in Analytical Chemistry. 2020, 123 (2), 115764.

procedure, the coverslips were cleaned by applying plasma for 3 min and then washed two times with acetone. In the second cleaning procedure, the coverslips were first sonicated for 10 min in acetone, then sonicated in 1M KOH for 20 min, and finally were treated with "base piranha" solution consisting of 14.3% v/v of 28-30 wt% NH_4OH, and 14.3% v/v of 30-35 wt% H_2O_2 that was heated to 70-80°C before immersing the slide in it as previously described[56, 66]. Following either cleaning procedure, coverslips were then modified to present surface amines by mounting them in a coplin jar and submerging them in a 2% v/v solution of (3-aminopropyl) triethoxysilane (APTES) (Sigma-Aldrich, catalog no. A3648-100ML) in acetone for 10 min, sonicating the jar for 1 min, incubating for another 10 min, rinsed twice with acetone, rinsed five times with water, and dried with nitrogen. Slides were then functionalized by sandwiching a 1:10 or 1:100 mixture of biotin-PEG-succinimidyl valerate and methoxy-PEG-succinimidyl valerate (Laysan Bio, Inc. catalog no. BIO-PEG-SVA-5K-100MG & MPEG-SVA-5K-1g) in 0.1M $NaHCO_3$ with a final mPEG concentration of 0.25 mg/μL and a final biotin PEG concentration of 0.0025 or 0.025 mg/μL for 1:100 or 1:10 mixtures, respectively, between pairs of coverslips. To reduce nonspecific binding of nucleic acids to the surface, the remaining surface amines were quenched by sandwiching ~80 μL of 0.03 mg/μL disulfosuccinimidyltartrate (Soltec Ventures, catalog no. CL107) in 1M $NaHCO_3$ between pairs of coverslips. Finally, the coverslips were dried completely under nitrogen flow and stored in the dark under air for further use for up to 3 weeks.

The sample cells were prepared prior to the single-molecule experiments using 20 μL pipette tips (ART low retention, Thermo Scientific). Specifically, a razor blade was used to cut through the diameter of a pipette tip ~2 cm from the wide end of the pipette tip and the noncut base was attached to the functionalized coverslip via epoxy (Ellsworth adhesives, hardman

double, catalog no. 4001)[66]. Four pipette tips were generally attached to each coverslip in this manner. The 1:10 PEG ratio coverslips were used for objective-TIRF miR-141 optimization experiments and the 1:100 PEG ratio was used for all optimization and quantification experiments for *EGFR* exon 19 deletion mutant DNA (*EGFR*Δ_{exon_19}) and quantification experiments only for miR-141 RNA. These ratios were chosen to ensure desirable field density at low and high sensor concentration for 1:10 and 1:100 respectively. Additionally, all objective-TIRF miR-141 quantification experiments used plasma cleaning while all *EGFR*Δ_{exon_19} experiments used piranha cleaning and miR-141 optimization used mostly piranha with some plasma cleaning. Both cleaning protocols had comparable analytical performance (**Figure 3.2**).

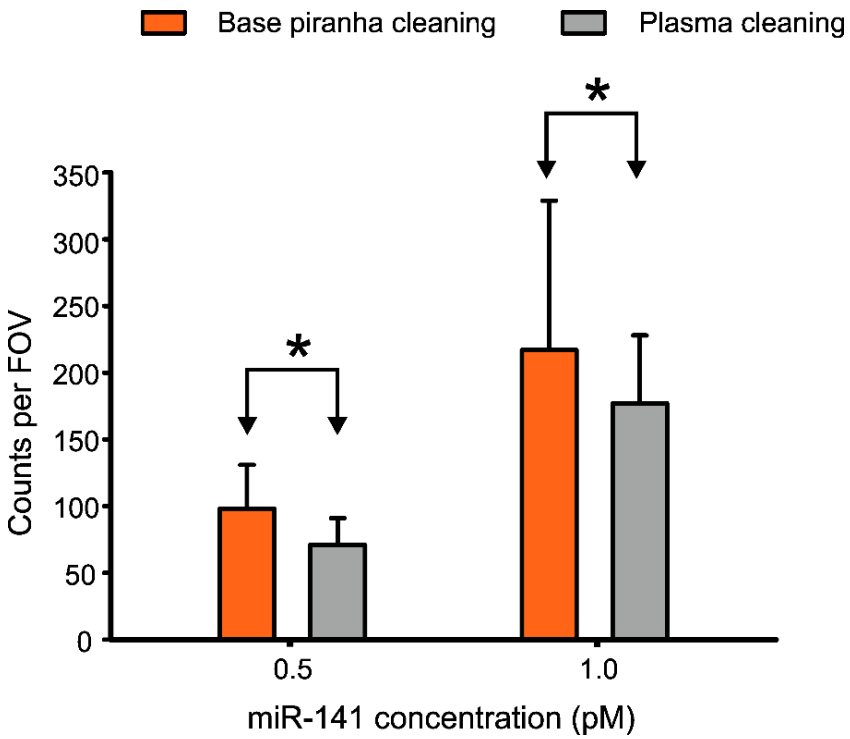

Figure 3.2. Comparison of the performance of coverslip cleaning protocols for detecting miR-141. Base piranha cleaning protocol used a solution consisting of 14.3% v/v of 28-30 wt% NH_4OH, and 14.3% v/v of 30-35 wt% H_2O_2 that was heated to 70-80°C, whereas plasma cleaning protocol used application of plasma for 3 min to clean glass coverslip. The experiments were performed using a glass coverslip passivated with biotin-PEG: m-PEG at a ratio of 1:100, 10 nM sensor, 0.5 and 1.0 pM miR-141, and 2 µM invaders (CI_{mis} + QI). All imaging was performed with 10% v/v formamide. See **Section 3.3.4 and 3.3.5** for more information on

Formamide and Invader optimizations. All data are presented as mean ± s.d. where n = 3 independent experiments. Single asterisk indicates the statistically insignificant differences at 95% confidence levels as assessed using a two-tailed, unpaired t test.

3.2.4 O-TIRF Assay Preparation

The Biotin-PEGlayed sample cells were first treated with 45 µL of 0.1-0.5 mg/mL streptavidin in T50 (10 mM Tris-HCl pH 8.0, 50 mM NaCl) for 10-20 min. The subsequent steps for this assay followed one of two procedures. One procedure similar to the P-TIRF protocol outlined in **Section 2.2.4** was followed for the initial optimization of iSiMREPS assay parameters and conditions for detecting miR-141. The anchor, capture, query strands and miR-141 target were combined at 200, 225, 250 and 5 nM final concentrations, respectively in 4× PBS (40 mM Na_2HPO_4, 7.2 mM KH_2PO_4, pH 7.4, 548 mM NaCl, 10.8 mM KCl), heated at 70˚C for 7 min in a metal bath, and then cooled at room temperature for 25 min. Unless otherwise noted, all nucleic acid samples preparation were performed in GeneMate low-adhesion 1.7 mL micro centrifuge tubes in 4× PBS. The sensor was diluted 1000-fold, and 100 µL of the sensor solution was added to the cell for 45 min to tether the sensor on the surface via streptavidin-biotin affinity linkages. After removing non-surface-bound sensors and washing the cell 3 times with 4× PBS, a 100 µL solution of a pair of invader strands (see **Table 3.1** and **Section 3.3.4**), each at 2 µM, was added to the cell and incubated for 20 min to remove non-target-bound fluorescent probes from the imaging surface. Next, the invaders solution was removed, the cell was washed 3 times with 4× PBS, and 200 µL imaging buffer containing the same oxygen scavenger system (OSS) outlined in **Section 2.2.4**, and the desired w/w% formamide in 4× PBS was added in the cell which was then imaged by TIRF microscopy.

The other procedure was followed for all experiments for detecting *EGFR*Δ_{exon_19} as well as miR-141 quantification. Unless otherwise noted, a synthetic forward strand of *EGFR*Δ_{exon_19}

was used for optimizing the sensor parameters and assay conditions, while all experiments for quantifying concentration and determining sensitivity and specificity used duplex *EGFR*Δ_{exon_19}. The anchor, capture, and query strands for miR-141 or *EGFR*Δ_{exon_19} was combined in a PCR tube at 400-500 nM final concentrations in 4× PBS, heated at 95˚C for 3 min, 72˚C for 7 min and 25˚C for 25 min and 4˚C for 10 min using a thermocycler to form a stable intramolecular complex. The sensor was then diluted to the desired concentration of 10 nM miR-141 sensor or 10-50 nM *EGFR*Δ_{exon_19} sensor and 100 µL of the diluted sensor was added in the cell and incubated for 30 min to tether the sensor to the surface. Next, 100 µL of a solution containing either miR-141 or *EGFR*Δ_{exon_19} target of the desired concentrations in 4× PBS was applied in the cell for 90 min for efficient capturing of the target by surface-tethered sensors. *EGFR*Δ_{exon_19} target solution containing 100 nM of auxiliary probe and 2 µM of dT_{30} were heated at 90˚C for 3 min in a metal block and cooled in a water bath at room temperature for 3 min prior to cell application. The non-target-bound probes were removed by invaders before imaging under an objective-type TIRF microscope in the presence of OSS as outlined above.

Parameter	Default	0%F 10s	0%F 30s	5%F	10%F	15%F	20%F
Frames	1-166	1-166	1-500	1-166	1-166	1-166	1-166
Exposure Time (s)	0.06	0.06	0.06	0.06	0.06	0.06	0.06
Intensity Threshold	200	200	200	200	200	200	200
Max Intensity	Inf	Inf	Inf	Inf	Inf	Inf	Inf
S/N Event Threshold	2	2	2	2	2	2	2
S/N Trace Threshold	3.5	4.5	3.8	4.5	3.4	3.4	1.4
Minimum N_{b+d}	5	2	4	4	3	5	6
Maximum N_{b+d}	Inf	Inf	Inf	Inf	Inf	Inf	Inf

Minimum $\tau_{on,\ median}$ (s)	0.06	0.24	0.18	0.06	0.06	0.06	0.06
Maximum $\tau_{on,\ median}$ (s)	10	9.9	19.98	7.38	7.44	1.38	2.7
Minimum $\tau_{off,\ median}$ (s)	0.06	0.12	0.18	0.06	0.06	0.06	0.06
Maximum $\tau_{off,\ median}$ (s)	0.9	3.3	6.06	2.82	2.1	1.2	0.6
Maximum $\tau_{on,\ event}$ (s)	5	Inf	22.5	8.82	3.96	9.78	9.54
Maximum $\tau_{off,\ event}$ (s)	4	Inf	15	5	4	4	2.34
Minimum $\tau_{on,}$ CV	Inf	Inf	Inf	Inf	Inf	Inf	Inf
Maximum $\tau_{on,}$ CV	Inf	Inf	Inf	Inf	Inf	Inf	Inf

Table 3.2. Acquisition parameters and default kinetic filtering criteria for different iSiMREPS sensors, with and without formamide, for detecting miR-141. All experiments other than the ones indicated specifically in this table use the settings listed under "default". The formamide variance filtering settings shown here represent data from 1 trial and were obtained using the SiMREPS kinetic parameters optimizer, which gives a starting point of filtering settings to maximize counts and minimize false positives using real and control data sets. The exact filtering settings vary from day to day for formamide experiments, as they were selected using the optimizer to gauge each condition's best possible performance. The τ_{on} and τ_{off} indicate target bound (high-FRET) and non-target-bound (low-FRET) states, respectively.

Sensors	Q_8C_6 QS_{18} CS_4	Q_8C_6 QS_{18} CS_{12}	Q_8C_6 QS_{18} CS_{19}	Q_8C_7 QS_{18} CS_{19}	Q_8C_8 QS_{18} CS_{19}	Q_8C_6 QS_{18} CS_{19}	Q_8C_6 QS_{18} CS_{19}	Q_8C_6 QS_{18} CS_{19}
Formamide (%)	0	0	0	0	0	0	5-10	15-20
Start-to-end frame	1-200	1-200	1-200	1-200	1-200	1-100	1-100	1-100
Exposure time per frame (s)	0.1	0.1	0.1	0.1	0.1	0.1	0.1	0.1
Acquisition time (s)	20	20	20	20	20	10	10	10
Intensity threshold per trace	500	500	500	500	500	500	500	500
S/N threshold per event	1.5	1.5	1.5	1.5	1.5	1.5	1.5	1.5

S/N threshold per trace	1.7	3.7	2.6	2.9	4.5	1.5	1.5	1.5
Minimum N_{b+d}	5	5	5	5	5	5	6	8
Maximum N_{b+d}	Inf	Inf	Inf	Inf	Inf	Inf	Inf	Inf
Minimum $\tau_{on,\ median}$ (s)	0.1	0.3	0.1	0.1	0.1	0.1	0.1	0.1
Maximum $\tau_{on,\ median}$ (s)	10	10	10	10	10	6	6	6
Minimum $\tau_{off,\ median}$ (s)	0.1	0.1	0.1	0.1	0.1	0.1	0.1	0.1
Maximum $\tau_{off,\ median}$ (s)	10	10	10	10	10	6	6	6
Minimum $\tau_{on,}$ CV	Inf	Inf	Inf	Inf	Inf	Inf	Inf	Inf
Maximum $\tau_{on,}$ CV	Inf	Inf	Inf	Inf	Inf	Inf	Inf	Inf
Maximum $\tau_{on,\ event}$ (s)	12	12	12	12	12	8	8	8
Maximum $\tau_{off,\ event}$ (s)	12	12	12	12	12	8	8	8
Maximum $I_{low\ FRET\ state}$ per trace	Inf	Inf	Inf	Inf	Inf	Inf	Inf	Inf
Number of intensity states	2	2	2	2	2	2	2	2
Ignore post photobleaching (s)	12	12	12	12	12	8	8	8

Table 3.3. Acquisition parameters and default kinetic filtering criteria for different iSiMREPS sensors with and without formamide for detecting *EGFR* exon 19 deletion mutant DNA (*EGFR*Δ_{exon_19}). The default kinetic filtering criteria was determined by used in thour newly developed machine learning based SiMREPS optimizer, which used data sets with multiple FOVs (e.g.., ≥ 10) from at least three independent experiments with and without the target as training data. For each individual experiment, the default kinetic filtering criteria were optimized slightly to minimize false positives in the negative control without rejecting true positive counts in the positive sample. The τ_{on} and τ_{off} indicate target bound (high-FRET) and non-target-bound (low-FRET) states, respectively.

3.2.5 Processing and Analysis of O-TIRF Data

MATLAB scripts were used to identify areas of high average FRET acceptor intensity within each field of view, generate intensity-versus-time traces from these areas, and save these traces for further analysis. These traces were then analyzed using a two-state HMM[96] algorithm to generate idealized (noise-less) intensity-versus-time traces to identify transitions between high- and low-FRET states. Thresholds of a minimum intensity of FRET transitions as well as a

minimum S/N for the FRET signal were applied to each trace to distinguish genuine FRET transitions from baseline noise[96] (**Tables 3.2 and 3.3**). Those traces passing the initial intensity and SNR thresholding were subjected to kinetic analysis to extract the number of FRET transitions per trace (N_{b+d}), the median dwell time in the high-FRET ($\tau_{on,\ median}$), and low-FRET states ($\tau_{off,\ median}$), the intensity of the low-FRET ($I_{low\text{-}FRET}$) and high-FRET ($I_{high\text{-}FRET}$) states, the longest individual dwell times in the high- and low-FRET states, and the coefficients of variation (CVs) of the dwell times in the high- and low-FRET states. These extracted parameters were subjected to minimum and maximum thresholding as indicated in **Tables 3.2 and 3.3** to identify target-bound sensors based on their distinct kinetic and intensity behavior and to count the number of such target-bound sensors ("accepted counts") observed in each movie. In addition, the cumulative frequencies of the dwell times in the high- and low-FRET states were fit to a single or double exponential function (see **Section 2.2.7**, and **Figure 3.5**) to obtain the average dwell time in each state and generate N_{b+d} histograms for each sensor. The N_{b+d} histograms and average dwell times were used to evaluate the sensor's performance in terms of separation from background and capacity for rapid detection. The accepted counts were used for quantification and assessment of sensitivity.

3.2.6 Monte-Carlo Simulation

Simulations were performed using a Monte Carlo simulation method described by Becker, Rosa, and Everaers[97]. In this method, each ssDNA nucleotide (nt) or dsDNA base pair (bp) was represented as a point at fixed distance from its neighbors, h (0.6 nm/nt for ssDNA[98] or 0.34 nm/bp for dsDNA[99]), and then a series of 10^7 iterations were applied to the construct via the Metropolis-Hastings algorithm. Each iteration consisted of a pivot attempt, which entails selection of a random point in the construct, followed by a counterclockwise rotation of all downstream points

(where upstream means closer to the point at which the construct is anchored to the surface) around a random axis by an angle randomly sampled from the range $\pm 50°$. The construct's post-pivot free energy, G, was calculated as the sum of the bending energy of all non-terminal points. The bending energy for the i^{th} non-terminal point (e.g., a point that is bound to at least two additional points), g_i, with 3D coordinate vector $\boldsymbol{r_i}$ is:

$$g_i = -k_{s,i} \frac{(\boldsymbol{r}_i - \boldsymbol{r}_{i\leftarrow}) \cdot (\boldsymbol{r}_i - \boldsymbol{r}_{i\rightarrow})}{|\boldsymbol{r}_i - \boldsymbol{r}_{i\leftarrow}||\boldsymbol{r}_i - \boldsymbol{r}_{i\rightarrow}|} \qquad (S3)$$

where $k_{s,i}$ is the point's bending spring constant, which is related to the persistence length, L_p (1.4 nm for ssDNA[100] or 53 nm for dsDNA[99], via the relation

$$L_p = \frac{-h}{\ln\left(coth(k_s) - \frac{1}{k_s}\right)} \qquad (S4)$$

and $r_{i\leftarrow}$ and $r_{i\rightarrow}$ are the 3D coordinate vectors for the nearest upstream and downstream points, respectively. (Note that for single-stranded RNA in the miR-141 design, we used $L_p = 0.8\,nm$ and $h = 0.67\,nm$)[101]. Next, G was calculated as $G = \sum g_i$ and the change in G from the last iteration, ΔG, was used to determine whether the pivot is accepted. Specifically, the pivot was accepted if $\Delta G < 0$ or, in the scenario that $\Delta G > 0$, if $\exp(-\Delta G) > R$, where R is a randomly generated number sampled from the range of 0 to 1. To reflect attachment of the construct to a surface, G was set to ∞ if any point in the construct exhibited a z-position below 0. Regardless of whether or not the pivot was accepted, the inter-strand distance was calculated at the end of each iteration as the average of the distances between the pairs of nucleotides that pair together to form the query-target duplex or the competitor-query duplex.

3.3 Results

3.3.1 Transitioning to O-TIRF System and Protocols

As outlined in **section 2.2.3**, P-TIRF experiments utilized a slide sandwich sample cell for sample introduction and imaging. This sample cell is a limiting factor for sensitivity because its larger surface area allows for the molecules to be more spread out in any given FOV which limits sensitivity. Additionally, the P-TIRF protocols for imaging and data processing and analysis outlined in **sections 2.2.5 and 2.2.6** required considerable manual preparation for imaging by the user to seat the prism and prevent drift since that setup did not come equipped with drift correction. It also required long, arduous manual trace selection which made the entire process less consistent and less efficient. Given the counts obtained per FOV in the formamide experiments for section 2.4 peaked at ~400 for ~100 pM of miR-141, the setup established in section 2 was also not capable of the low femtomolar LOD necessary to match classical SiMREPS and function effectively as a liquid biopsy assay. An O-TIRF workflow as outlined in more detail in **Sections 3.2.2-3.2.5** was thus transitioned to as it was demonstrated to be a superior option because of its sample cell design and superior workflow. The cut pipette tip sample cell offers a significant advantage over the slide sandwich for sensitivity because of its smaller surface area and taller height which allows for a higher concentration of target within the same field of view, allowing detection of lower concentrations than was possible previously. Additionally, the O-TIRF workflow is easier to use because of features like automatic drift correction on the microscope and the tools to automate movie collection, processing of data, and analysis of data. Additionally, a shift from using bBSA to Biotin-PEG as the surface adsorbent was made because bBSA preparations had some problems that negatively impacted the sensitivity. Surface adsorption by bBSA was inconsistent and aggregates were a common

occurrence. This is shown by the variation in the N values for counts in **Figure 2.8** where the full observation window was available where the CV after calculating average and standard deviation was 0.41. This difference may be attributed to the preparation procedure for bBSA lacking T50 buffer which is known to provide stability for proteins[102] and may have helped address some of the issues observed. Nonetheless, this variance would be a significant problem for iSiMREPS because diagnosis through liquid biopsies necessitates quantifying the targets of interest[26, 27] and a high CV will reduce the reliability of quantification and hurt the overall sensitivity and viability of iSiMREPS for liquid biopsies. PEG was chosen for the final, standardized assay because of its better results in terms of FOV, density, and counts. Once the switch to PEG and an O-TIRF protocol was completed, the method of preparing the target with the sensor was kept as it was desirable for optimization experiments because it was easier to prepare and faster than introducing the target after the biosensor and was thus used for all miR-141 optimizations. However, this was not carried over to the final assay design as actual samples would already have low target concentration and this approach would create additional problems by further diluting them.

3.3.2 Understanding iSiMREPS Dynamics via Monte-Carlo Simulation

To better understand the effect of spacer length on iSiMREPS probe kinetics, we developed a coarse-grained Monte Carlo simulation model (see section **3.2.6** for details). Our simulation results (**Figure 3.3**) show that at very short spacer lengths such as those used for the 3 nt biosensors described in **Section 2.3**, the distance between the target and query strands is large due to conformational rigidity of the stiff anchor duplex and this inhibits pairing of the strands to form the target-query interaction. Increasing spacer length up to 10 nt allows the target and query strands to interact without bending the anchor duplex. Beyond 10 nt, increasing the spacer length

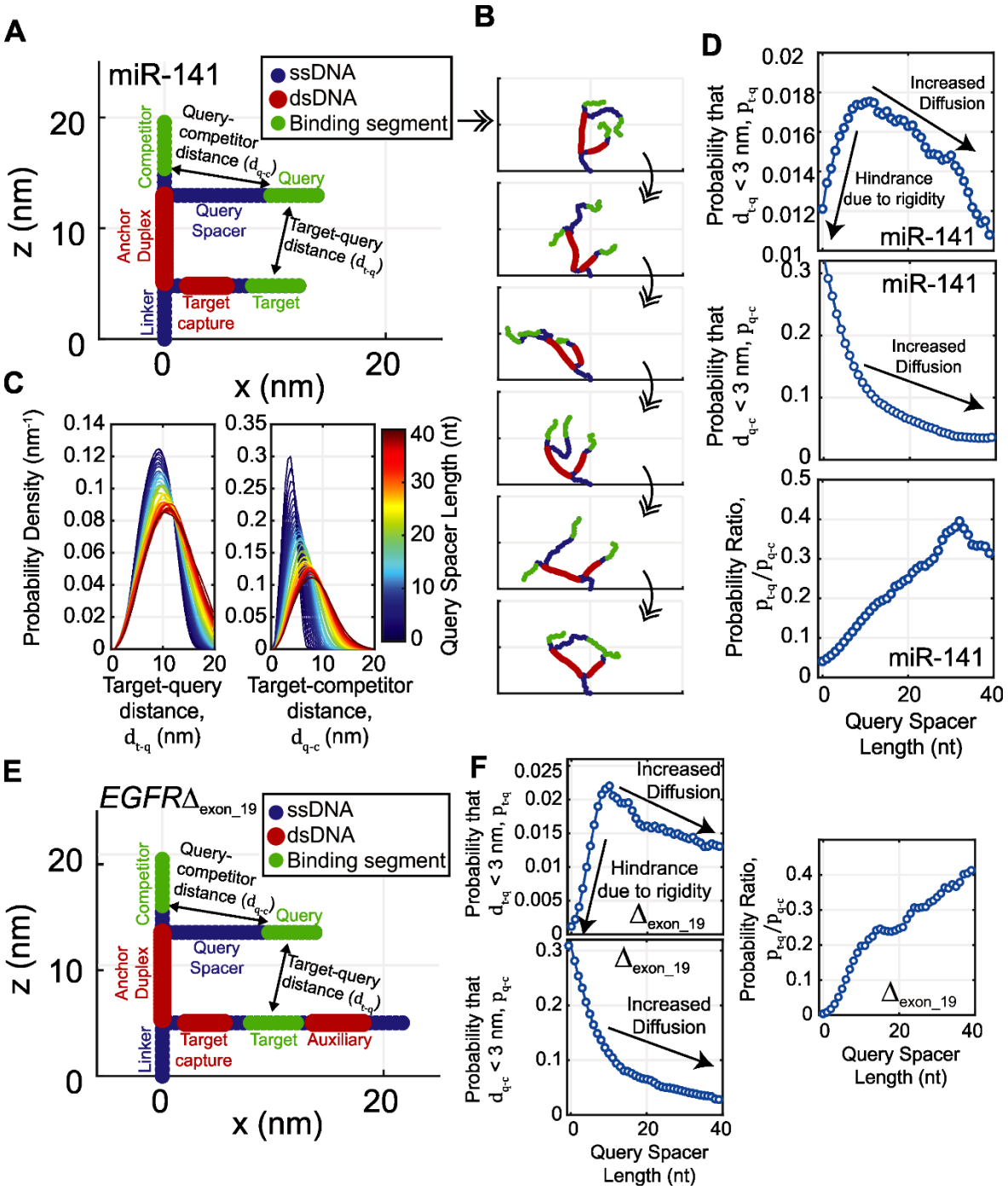

Figure 3.3 Simulations support finding that iSiMREPS kinetics scale non-monotonically with query spacer length. (**A**) Initialized simulated iSiMREPS construct with labels showing the three main regions of the probe (anchor, query, and target) as well as the distances between the target and query segments (d_{t-q}) and the query and competitor segments (d_{q-c}) for the miR-141 construct. All points are represented as circles with color denoted by polymer type as shown in the legend. (**B**) Six representative snapshots of a 2D version of the Monte Carlo simulation method, separated by at least 10,000 iterations each. (**C**) Probability density functions of d_{t-q} for

simulations with query spacers lengths (depicted by color) ranging in length from 0 nt to 39 nt. (**D**) Three plots are shown. The top plot shows the probability (denoted p_{t-q}) that d_{t-q} is less than a close contact cutoff of 3 nm, as measured from the cumulative output of the Monte Carlo simulation, as a function of the query spacer length. The middle plot is similar, but for d_{q-c}. The bottom plot shows the ratio p_{t-q}/p_{q-c}. Because the activation energy for base pairing should be largely independent of spacer length and is also expected to be the rate-limiting step due to the high rate of diffusion, the strand association rate should scale linearly with p_{t-q}. Arrows in the top plot show that there are two roughly linear trend regimes. At query spacer lengths shorter than 9 nt, decreasing the spacer length decreases p_{t-q} by what we expect is a hindrance imposed by the long, stiff anchor duplex. In this regime, it is expected that this hindrance will also increase the rate of unbinding. In contrast, p_{q-c} decreases monotonically with increasing spacer length. This finding is consistent with the conformational rigidity model, as there are no dsDNA regions separating the competitor and query segments. At spacer lengths exceeding ~10 nt, increasing the spacer length mildly decreases p_{t-q} due to what we expect is an increased radius of diffusion. This trend is seen for p_{q-c} across the entire range of spacer lengths tested. However, while both p_{t-q} and p_{q-c} decrease monotonically with long spacer lengths, the ratio p_{t-q}/p_{q-c} increases monotonically across the entire range, suggesting that increasing spacer length monotonically increases the preference for the target's association with the target over the competitor. These findings hold true for cutoffs that are reasonably larger or smaller than 3 nm (not shown). Notably, this simulation method is limited in that it does not account for long-range repulsive interactions between non-neighboring regions of the probe. We expect that if we did incorporate such long-range interactions, different branches of the iSiMREPS probe would be further repelled by each other, potentially steepening the correlation observed in the long-spacer length regime. (**E**) Initialized simulated iSiMREPS *EGFR* exon 19 deletion mutant DNA (*EGFR*Δ_{exon_19}) construct with labels showing the three main regions of the probe (anchor, query, and target + auxiliary complex), like that shown in A. (**F**) Results for a simulation of the *EGFR*Δ_{exon_19}design show similar trends to those shown in D.

causes the target-query distance to gradually decrease due to the query strand's increased radius of diffusion. By contrast, the query-competitor distance decreases monotonically across all spacer lengths. These findings (**Figure 3.3**) are in qualitative agreement with the experimental results for detecting miR-141 using the 6 nt competitor (**Figures 2.5-2.6**); the QS_3 sensors showed that query-target interactions were unfavorable, while the QS_{18} sensors showed near-parity between the two states and the QS_{33} sensors favored query-target binding.

3.3.3 Optimization of iSiMREPS for *EGFR*Δ_{exon_19}, a ctDNA

To test for generality of the iSiMREPS approach, we next targeted a different class of nucleic acid biomarker: ctDNA. We chose an *EGFR* exon 19 deletion mutation DNA (*EGFR*Δ_{exon_19}) commonly found as fragmented ctDNA in biofluids of NSCLC patients[44]. The optimized iSiMREPS sensor features the same fundamental components and architecture as the sensor design for miR-141 detection. However, it deals with the greater length and dsDNA nature of the ctDNA through two additional features. First, we added a short auxiliary probe that stably binds the extended 3' end of the forward strand of the duplex mutant target DNA (**Figure 3.4A**) to prevent reannealing of the complementary strand once melted during sample preparation. The auxiliary probe also aims to minimize any potential secondary structure of the target strand[88].

Additionally, we noticed that the DNA-based architecture of iSiMREPS sensors permitted selective removal of the CP and QP of biosensors without a target after the target capture step and before imaging (**Figure 2.1**). We hypothesized that we could achieve a desirable S/N improvement by removing these probes from target-less sensors and eliminating the unwanted signal at its source. To this end, we developed a two-step process that employs a 2 ssDNA strands we call invader strands that selectively bind and remove the QP and CP from target-less biosensors via TMSD, a strategy often displayed in dynamic DNA nanotechnology[103]. In the first step, a capture invader (CI) binds to a toehold exposed on the CP in the absence of target. Via TMSD, the CI disrupts the capture-anchor duplex to remove the CP from the surface (**Figure 3.4B**). This first step reveals a second toehold where the CP was previously bound to the anchor and this new toehold is then bound by a query invader (QI) in the second step. The QI disrupts the query-anchor duplex to remove the QP from the biosensor (**Figure 3.4B**). The end result is the removal of any fluorophores on from which signal can be generated on target-less biosensors. Although these

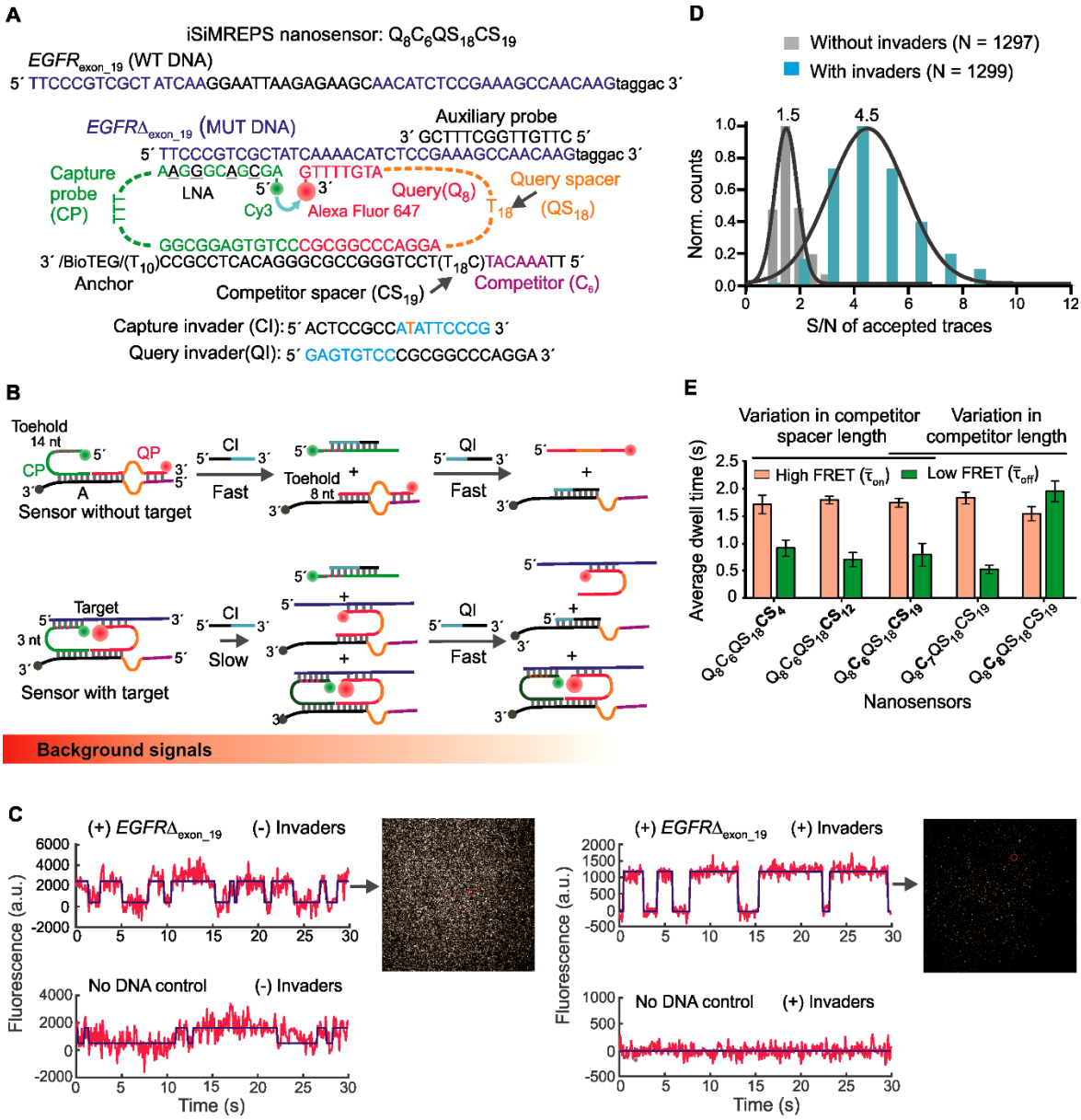

Figure 3.4. Design and optimization of iSiMREPS for detection of a ctDNA biomarker mutant DNA sequence. (**A**) Design of optimized smFRET-based iSiMREPS sensor for the detection of *EGFR* exon 19 deletion mutant DNA (*EGFR*Δexon_19). Two invaders, which are used to remove non-target-bound fluorescent probes from the surface, are also shown. (**B**) Schematic depiction of the removal of non-target-bound fluorescent probes (top) using CI and QI, and the much slower side reaction that removes target-bound probes (bottom). Each non-target-bound sensor has an exposed 9 nt toehold on the CP that binds with CI (cyan) and initiates the toehold displacement cascade. A 3 nt toehold on the CP in target-bound sensors can also bind with CI and ultimately prevent detection of a target molecule, but this reaction occurs much more slowly due to the shorter toehold. (**C**) Comparison of single-molecule FRET traces of iSiMREPS sensor in the presence (top) or absence (bottom) of the target sequence containing the *EGFR*Δexon_19. Background signals are significantly reduced with the application of invaders (right panel) compared to samples imaged without invader treatment (left panel). (**D**) Comparison of signal-to-noise (S/N) ratio with

(cyan) and without (grey) invaders. (**E**) The average dwell times spent in the high-FRET ($\bar{\tau}_{on}$) (light red) and low-FRET ($\bar{\tau}_{off}$) (green) states for different iSiMREPS sensors designs. All data are presented as mean ± s.d., with n = 3 independent experiments.

invaders are designed to work on non-target-bound probes to reduce background signals significantly, the 3 nt spacer region on the CP is also capable of functioning as a toehold[104] and this can lead to unwanted removal of probes from target-bound sensors. **Section 3.3.4** will detail the optimization of this protocol in more detail.

We performed proof-of-concept studies for detecting *EGFR*Δ_{exon_19} using a $Q_8C_6QS_{18}CS_{19}$ sensor, where CS, as stated in **Section 2.3**, denotes the length of the spacer near the competitor sequence or the competitor spacer, (**Figure 3.4A**). This sensor was modelled after the optimized sensor for miR-141 (**Figure 2.1**), but used a longer competitor spacer (CS_{19} versus CS_3) to further improve parity between the FRET states. We used a query specific to *EGFR*Δ_{exon_19} (T_m = 23.9˚C,**Table 3.1**) that was designed to maximize discrimination between *EGFR*Δ_{exon_19} and the off-target wild type sequence (**Figure 3.4A**), as predicted using NUPACK [93, 94]. For optimization of sensor designs, we used a synthetic forward strand of *EGFR*Δ_{exon_19}. A pair of CI and QI strands, as shown in **Figure 3.4A**, were designed to remove non-target-bound fluorescent probes from the surface (**Figure 3.4B**). However, the initial design of CI contains a single mismatch in the spacer region to prevent the use of the capture spacer as a toehold (**Figure 3.4A**).

To examine the performance of $Q_8C_6QS_{18}CS_{19}$ for detecting *EGFR*Δ_{exon_19} and to assess the efficacy of the invader strands, the preassembled sensor was first tethered to the glass coverslip and the mutant DNA target was introduced to bind the sensor probes on the surface. Next the samples were (or were not) incubated with invaders and imaged with O-TIRF. We found that invader treatment significantly reduced background signal in single-molecule intensity-time traces, resulting in a 3-fold higher S/N ratio relative to samples that were not treated with

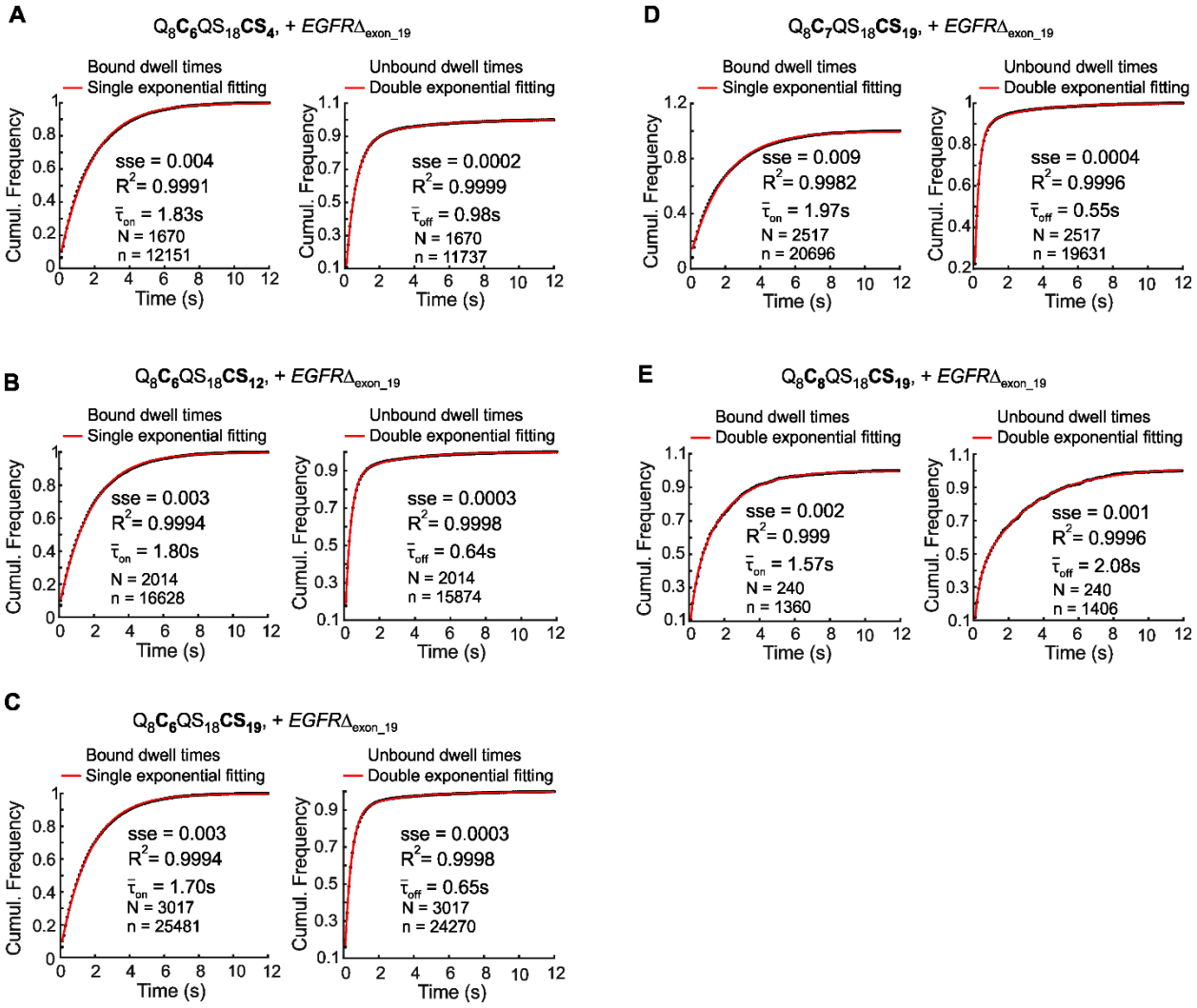

Figure 3.5. Estimation of average dwell times of smFRET states for different iSiMREPS sensors for detecting *EGFR* exon 19 deletion mutant DNA (*EGFR*Δexon_19). (**A-E**) Calculation of the average dwell time for the target bound (high-FRET) ($\bar{\tau}_{on}$) and non-target-bound (low-FRET) ($\bar{\tau}_{off}$) states for different iSiMREPS sensors for detecting *EGFR*Δexon_19. All experiments were performed without formamide in the imaging buffer. For all the sensors except the one with an 8 nt competitor, the target bound state dwell times were fitted with a single exponential. Single exponential fitting was chosen when sum squared error (sse) <0.08 and $R^2 > 0.96$, and double exponentials were used otherwise. All non-target-bound dwell times were fitted with a double exponential. All data is from 1 of 3 independent experiments. The 'N' represents number of accepted traces, and 'n' represents the total number of dwell time events used for the fitting.

invaders (**Figure 3.4C and 3.4D**). Exponential fitting of dwell time distributions (see Section **2.2.7** and **Figure 3.5**) showed a $\bar{\tau}_{on}$ and $\bar{\tau}_{off}$ of 1.7 ± 0.1 s and 0.8 ± 0.2 s respectively, indicating some

bias for the high-FRET state (**Figure 3.4E**). These $\bar{\tau}_{on}$ and $\bar{\tau}_{off}$ are shorter than those measured for miR-141 detection under similar salt concentration and temperature. This change likely arose because the query-mutant DNA duplex (T_m = 23.9°C) was less stable than query-miR-141 duplex (T_m = 30.2°C). Moreover, the presence of the extra 3′ sequences in the *EGFR*Δ_{exon_19} target may destabilize the interaction with the query strand slightly by introducing more electrostatic repulsion from the nearby phosphates.

To modulate the dwell times of high-(τ_{on}) and low-FRET (τ_{off}) states, we designed several additional iSiMREPS sensors. Firstly, we decreased the length of competitor spacer of $Q_8C_6QS_{18}CS_{19}$ to CS_{12} and CS_4 (**Figure 3.6)**. We expected that decreasing the CS length would 1) increase the rate of the query–competitor interactions because of higher local effective concentrations, and 2) increase τ_{off}, making it more closely resemble the high-FRET state (τ_{on}). However, the results showed that varying the CS length had an insignificant effect on the dynamics of FRET transitions in iSiMREPS sensors (**Figure 3.4E**). This result may be because of the relatively long QS (dT_{18}) present in this series of designs introduced substantial flexibility to all constructs, thus undercutting attempts to finely tune effective local concentrations. Secondly, we ran experiments where we increased the length of competitors of $Q_8C_6QS_{18}CS_{19}$ to C_7 and C_8 to raise the thermodynamic stability of the query–competitor interaction (**Table 3.4**). Indeed, increasing the competitor length from 6 to 8 nt increased $\bar{\tau}_{off}$ significantly (**Figure 3.4E**), further confirming that competitor length is one of the most important parameters in iSiMREPS sensor design. Overall, the $Q_8C_6QS_{18}CS_{d = 4, 12, 19}$ design, where d is the number of nucleotides in CS, worked well for *EGFR*Δ_{exon_19}. Given the insignificant effect of CS length, $Q_8C_6QS_{18}CS_{19}$ was chosen for further assay optimization.

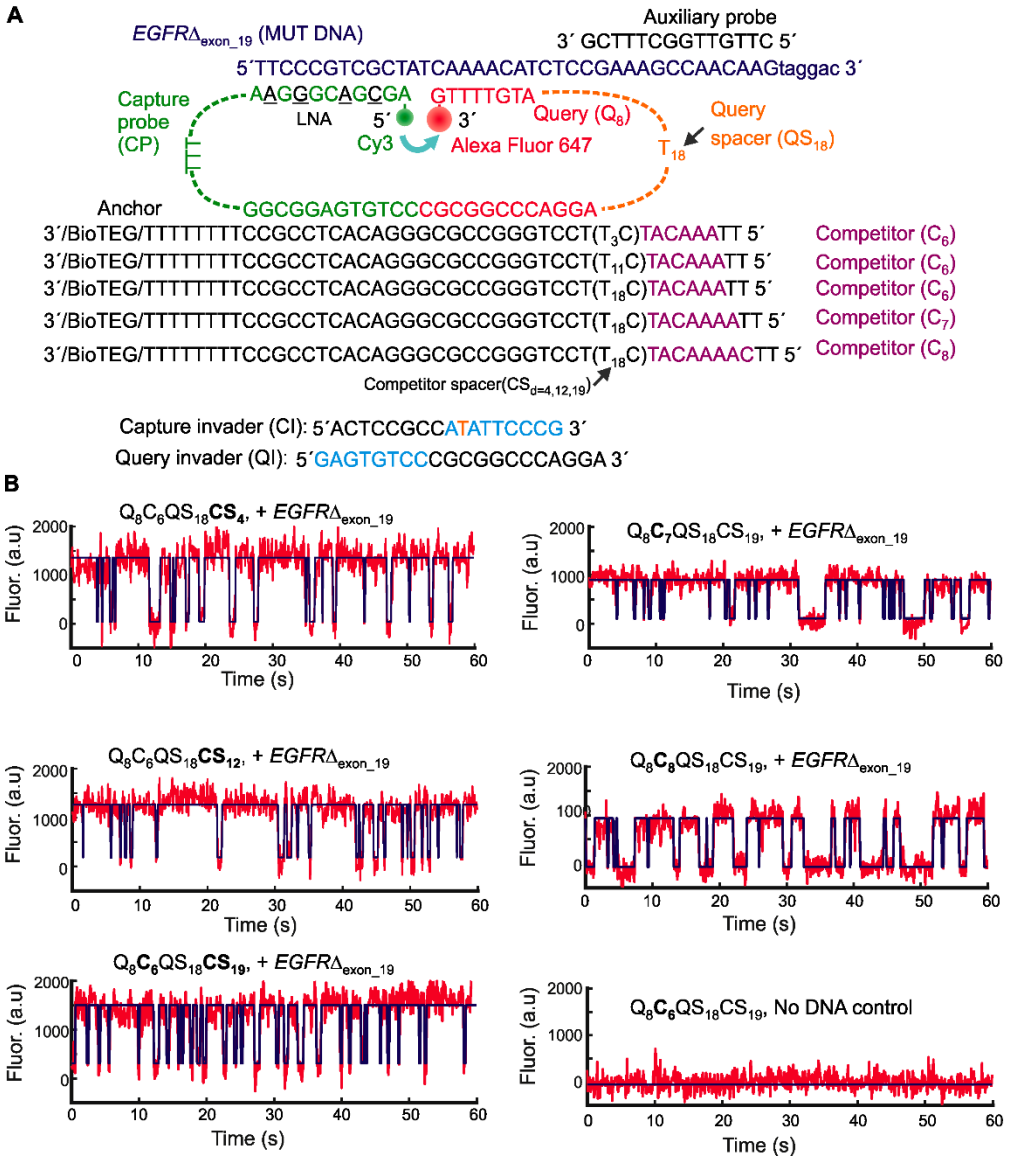

Figure 3.6. Schematic of different iSiMREPS sensors and representative single molecule kinetic traces in the presence of *EGFR* exon 19 deletion mutant DNA (*EGFR*Δexon_19). (**A**) Designs of iSiMREPS sensors for detecting *EGFR*Δexon_19with various competitor spacer and competitor (C) lengths. (**B**) Representative single-molecule kinetic traces (red) for different iSiMREPS sensors with or without *EGFR*Δexon_19 with an idealized hidden Markov model (HMM) fit (blue). All experiments were performed using 10 nM preassembled sensors consisting of anchor, capture and query probes, and 10 pM *EGFR*Δexon_19 forward strand. Imaging was done in 4x PBS (pH 7.4) at room temperature under an objective-type-TIRF microscope. The donor fluorophore (Cy3) was excited at 532 nm and the acceptor fluorescence (Alexa Fluor 647) was recorded as FRET signal.

Sensor ID	Complementary (bp)		ΔG (kcal/mol)		T_m (°C)	
	Q-T	Q-C	Q-T	Q-C	Q-T	Q-C
$Q_8C_6QS_{18}CS_4$	8	6	-11.7	-9.1	23.9	0
$Q_8C_6QS_{18}CS_{12}$	8	6	-11.7	-9.1	23.9	0
$Q_8C_6QS_{18}CS_{19}$	8	6	-11.7	-9.1	23.9	0
$Q_8C_7QS_{18}CS_4$	8	7	-11.7	-10.6	23.9	11.7
$Q_8C_8QS_{18}CS_4$	8	8	-11.7	-11.7	23.9	23.9

Table 3.4. The free energy (ΔG) and melting temperature (T_m) of query-target (Q-T) and query-competitor (Q-C) duplexes for different iSiMREPS sensors used for detection of *EGFR* exon 19 deletion mutant DNA ($EGFR\Delta_{exon\_19}$). ΔG was predicted using NUPACK[93, 94] and T_m was calculated using IDT oligo analyzer[86] as outlined in **Section 2.2.1**. The single stranded regions (spacers) flanking the complementary segments of query, target and competitor probe were considered to calculate ΔG using NUPACK[93, 94], but only complementary segments were considered to calculate T_m using IDT oligo analyzer.

3.3.4 Optimization of iSiMREPS S/N improvement via TMSD

Once the O-TIRF setup was established, improving S/N for sensitivity was an important step, especially for protocols that would require introducing the target after the sensor. This was necessary because at sufficiently high probe concentrations, there are enough biosensors within a given area that when any individual molecule is examined, there will be bleedthrough of donor signal along with a modest excitation of acceptors and subsequent noise from nearby biosensors that lack a bound target. This hurts sensitivity as it reduces S/N and limits the usable probe concentration. One option to address this was to use a different fluorophore pair where there was more distance between the donor and emission spectra of the fluorophores to reduce the possibility of bleedthrough or unwanted acceptor excitation. Alexa Fluor 488 (A488) and 647 were one such pair where the excitation wavelength overlaps poorly with A647's excitation and emission wavelengths[105]. We hypothesized that despite the lower FRET efficiency this pair had when compared to Cy3-A647, there would be enough signal in order to get a clear, crisp field. However, this strategy proved ineffective because the field was far too dim when we were

observing for FRET signals vs for direct excitation. As a result, there was not a sufficient enough change in signal intensity for the individual fluorescent areas to be distinguished from noise and increasing the laser power did not provide substantial improvement and placed the system at risk for rapid photobleaching. As such, a new approach was needed.

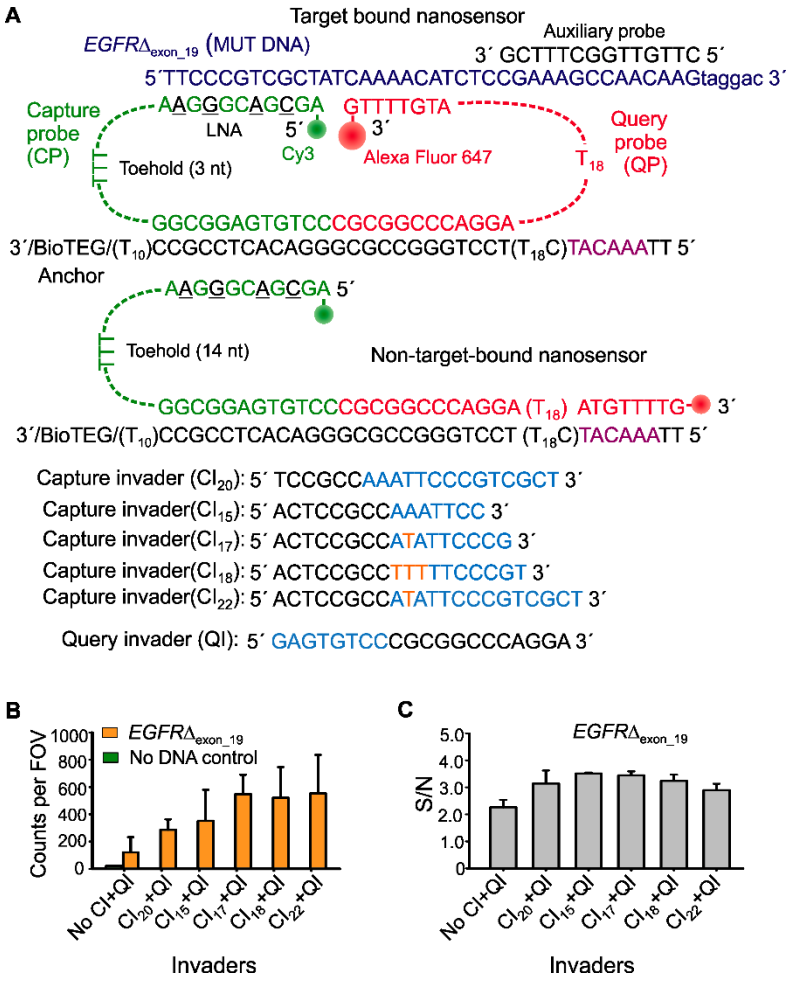

Figure 3.7. Optimization of the invaders for increased sensitivity of iSiMREPS assays for nucleic acids. (**A**) Schematic of target bound and non-target-bound iSiMREPS sensors, depicting the toehold available for invader binding as well as capture invaders (CIs) of variable lengths. Cyan segments of the invaders are complementary to the exposed toeholds, while orange sequences represent the nucleotides that are mismatched between invaders and toeholds in the CP. (**B**) Number of accepted counts per FOV in the presence of *EGFR*Δ$_{exon_19}$ after application of different CIs. (**C**) S/N ratio in the candidate target bound molecules after application of different CLs. All data are presented as the mean ± s.d. of n = independent experiments.

As mentioned in **Section 3.3.3**, we noticed that the DNA-based architecture of iSiMREPS sensors permitted selective removal of the CP and QP of biosensors without a target after the target capture step and before imaging and demonstrated that this results in an improvement in S/N (**Figure 3.4B**). We decided to thoroughly test and optimize the effect of this TMSD strategy by initially performing five experiments with a biosensor customized for *EGFR*Δ_{exon_19} detection that was built on the standard design of the miR-141 biosensor and modified in terms of sequence length and placement for *EGFR*Δ_{exon_19} (**Figure 3.7**) each pairing the identical query invader (QI) with one of five different capture invaders (CIs) shown in **Figure 3.7A**. These CIs have different toehold and pairing region lengths. Some contain mismatches to the spacer region of the CP, which are intended to mitigate undesired displacement of target-bound sensors. We also performed a control experiment without invaders. These experiments showed that all five CIs increase the number of detected counts per FOV and decrease the number of false positives in a control without mutant DNA (**Figure 3.7B**). However, treatment with CIs that contain one or more mismatches (CI_{17}, CI_{18}, and CI_{21}) with the capture probe's 3 nt spacer showed more accepted traces and, surprisingly, improved S/N compared to treatment with fully complementary CIs (CI_{20} and CI_{15}) (**Figure 3.8**). These results suggest that fully complementary CIs cause unwanted removal of target-bound probes. Overall, treatment with CI_{17} and QI performed the best, increasing the number of accepted traces ~4.5-fold compared to assays without invaders (**Figure 3.7B**). This strategy was also tested and optimized for the detection of miR-141 (**Figure 3.9**); the best-performing CI had a mismatch and exhibited a ~3.5-fold increase in accepted traces and improved S/N (**Figure 3.9**). Interestingly, there was only a modest improvement in S/N for miR-141 vs *EGFR*Δ_{exon_19} and this is likely because accepted miR-141 traces possess high intensity values and S/N for both conditions and

without invaders, too many traces lack this characteristic intensity due to noise and are rejected as a result.

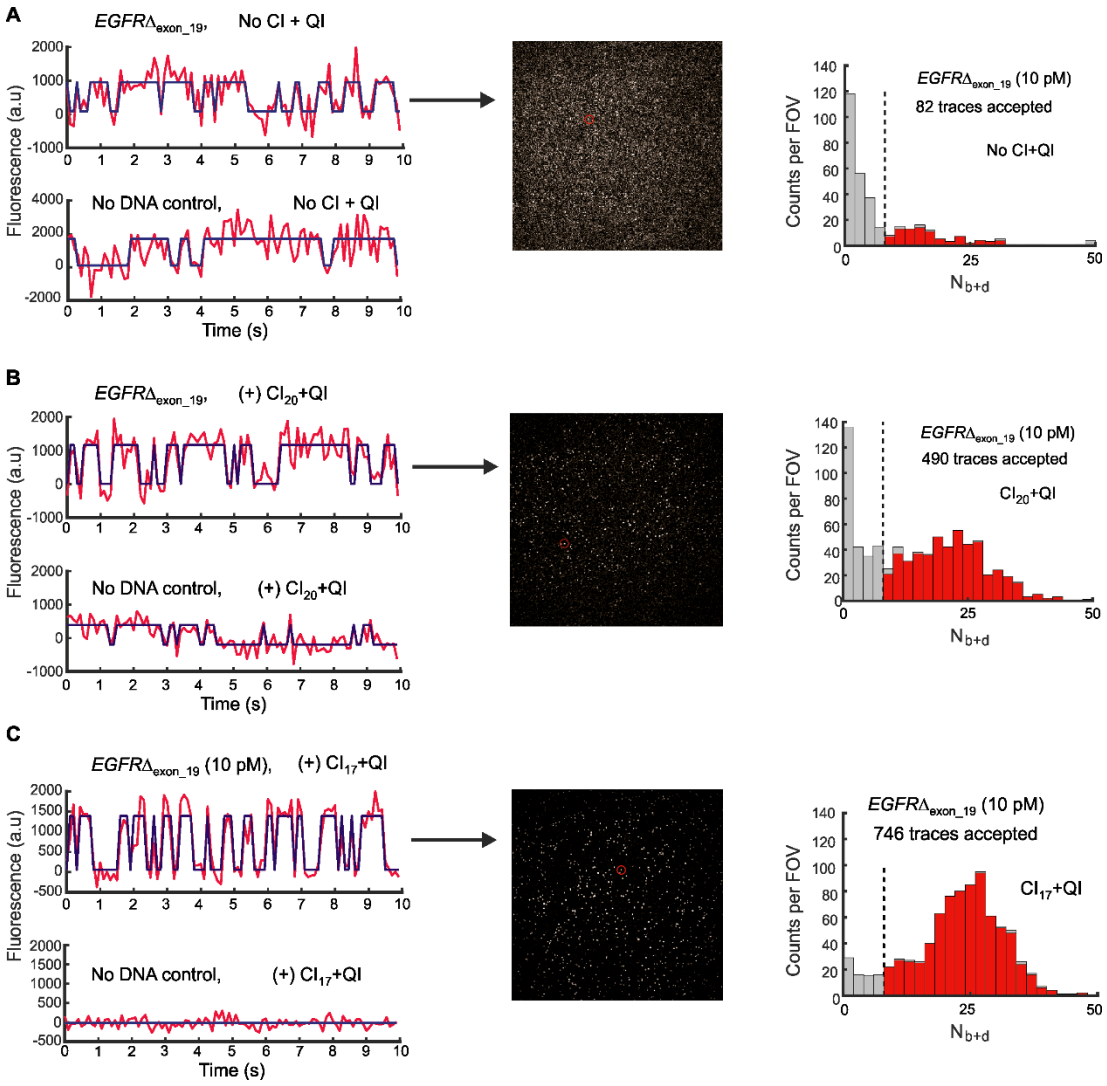

Figure 3.8. Effect of different invaders on the background signals to detect *EGFR* exon 19 deletion mutant DNA (*EGFR*Δexon_19). (**A-C**) Representative single-molecule kinetic traces, images of a field-of-view (FOV) and histograms of the number of candidate molecules per FOV showing a given number of binding and dissociation events (N_{b+d}) detected in 10 s per FOV, after applying thresholds for FRET intensity, S/N, and dwell times of bound and unbound states without invaders (**A**), with invaders CI_{20}+QI (**B**), and with invaders CI_{17}+QI (**C**) in the presence and absence of *EGFR*Δexon_19 target (see Figure 5A for invaders sequences). All experiments were performed using 0.2 mg/mL streptavidin (incubation: 10 min), 10 nM sensor (incubation: 30 min), 10 pM forward strands of *EGFR*Δexon_19 (incubation: 90 min), 1 µM invaders (incubation: 20 min). Objective-TIRF imaging was performed in the presence of 10 % v/v formamide in the imaging buffer. All data are presented as the mean ± s.d. of n = independent experiments.

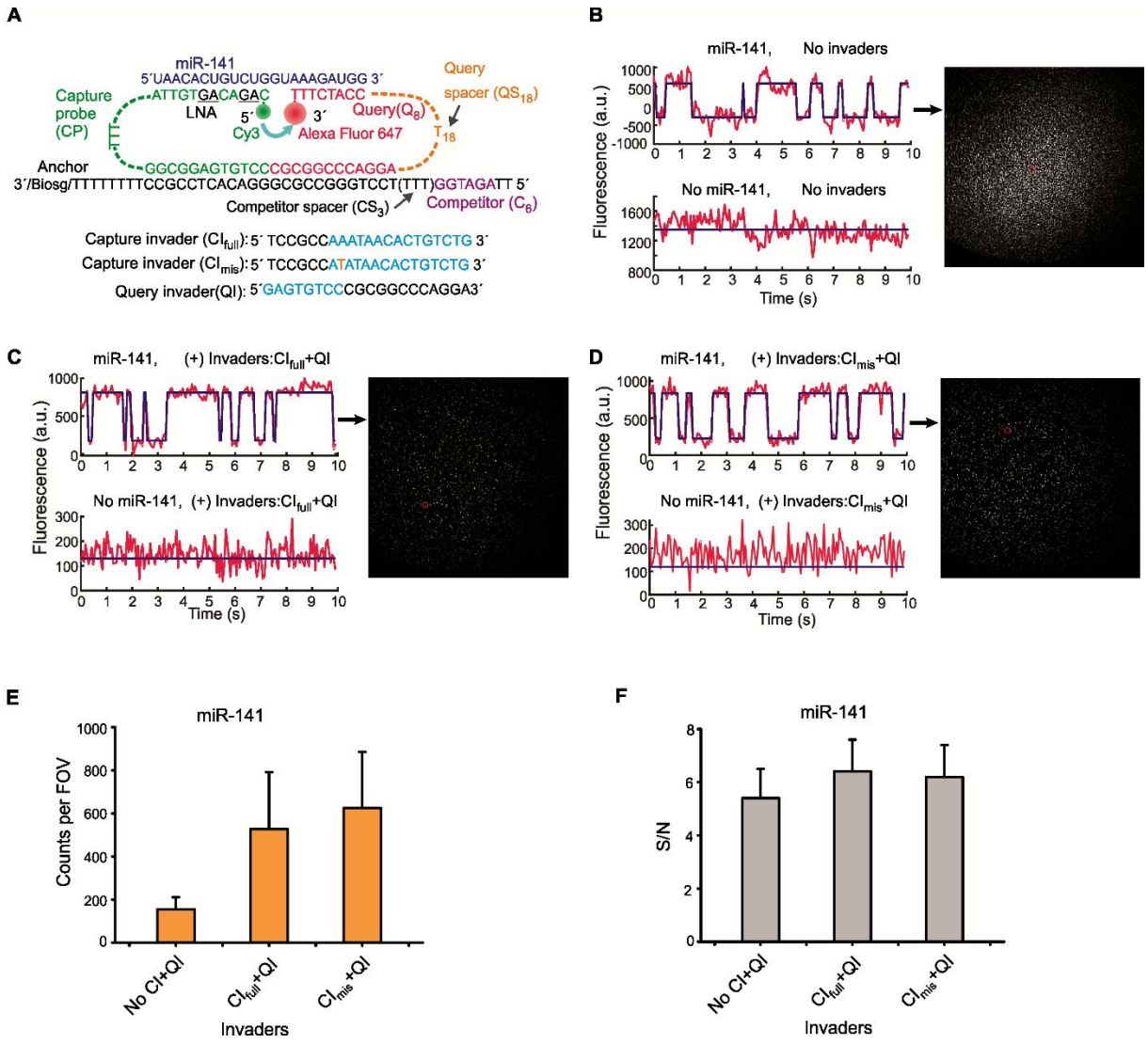

Figure 3.9. Schematic of the design of iSiMREPS sensor for detecting miR-141 and representative single molecule kinetic traces in the presence and absence of different invaders. (**A**) Design of the optimized miR-141 sensor and different invaders tested. (**B-D**) Representative single-molecule kinetic traces and images of a FOV without invaders (**B**), with invaders CI_{full}+QI (**C**), and with invaders CI_{mis}+QI (**D**) in the presence and absence of miR-141. (**E**) Number of accepted counts per FOV in the presence of miR-141 after application of different capture invaders. (**F**) S/N ratio in the candidate target bound molecules after application of different capture invaders. Overall application of invaders improved the background signals as well the signal-to-noise ratio of single molecule traces as well as accepted counts compared to without invaders application. For all experiments shown, sensors were assembled at 200 nM in the presence of 5 nM miR-141. The pre-assembled sensors were then diluted it 1,000-fold and added

to the surface. Imaging was performed in 4× PBS at pH 7.4. All data are presented as the mean ± s.d. of n = independent experiments.

3.3.5 Full Evaluation and Optimization of Formamide Use

Having optimized iSiMREPS designs for both miRNA and mutant DNA as well as a strategy for clearer S/N, we next sought to fully characterize and optimize the acceleration of sensor kinetics to increase the speed of kinetic fingerprinting via formamide addition initially established in **Section 2.4**. As predicted, adding formamide (10% v/v) to the imaging buffer resulted in intensity-time traces with much shorter τ_{on} and τ_{off} for both miR-141 and EGFRΔexon_19 (**Figures 3.10A and 3.10D**, left panels). With a standard acquisition time of 10 s per FOV and image processing (see **Tables 3.2 and 3.3**), histograms of the number of binding and dissociation events (N_{b+d}) for both miR-141 and EGFRΔexon_19 targets showed good separation from background with, but not without, 10% formamide (**Figures 3.10A and 3.10D**, right panels).

Next, we varied the formamide volume fraction from 0% to 20% (v/v) to minimize data acquisition time while retaining sensor function and high sensitivity. The single molecule kinetic traces showed that the τ_{on} and τ_{off} decreased with increasing formamide (**Figures 3.10B and 3.10E**). The $\bar{\tau}_{on}$ and $\bar{\tau}_{off}$ gradually decreased with increasing formamide from 0-10% for both targets but stayed roughly constant from 10-20% for EGFRΔexon_19 and 15-20% for miR-141 (Figs. S8, S9, 4B and 4E). Specifically, shifting from 0% formamide to 10% formamide decreased $\bar{\tau}$on and $\bar{\tau}$off by factors of 7 and 4.5 respectively, for miR-141 (**Figure 3.10B**) and 3.5 and 2.5, respectively, for *EGFR*Δ_{exon_19} (**Figures 3.10E**). The differences between the two sensors are consistent with the fact that DNA-RNA duplexes are more sensitive to destabilization by formamide than DNA-DNA duplexes[106]. The target bound signals separated well from

background at ≥10% formamide and poorly or inconsistently at 0 and 5 % formamide (**Figures 3.11-3.12**). The standard acquisition of ~ 10 s per FOV obtained in iSiMREPS as assisted by 10% formamide is approximately 60-times faster than intermolecular SiMREPS approaches[64, 66].

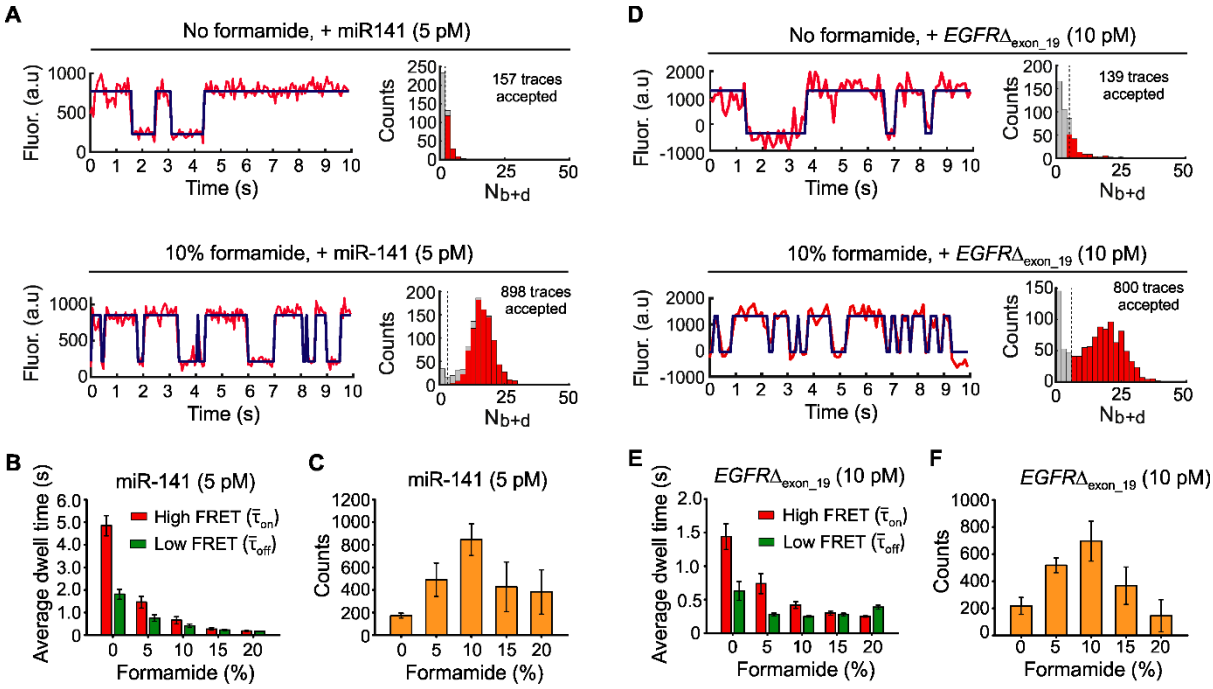

Figure 3.10. The effects of formamide on iSiMREPS sensors for rapid detection of miRNA and ctDNA. (**A**) Representative single- molecule kinetic fingerprints and histograms of the number of candidate molecules per FOV showing a given number of binding and dissociation events (N_{b+d}) after applying thresholds for FRET intensity, S/N, and dwell times of bound and unbound states in presence of 5 pM miR-141, without (top) and with 10% (v/v) formamide (bottom). The $Q_8C_6QS_{18}CS_3$ sensor as depicted in Figure 2A was used for this study and pre-treated with a capture invader (5′TCCGCCATATAACACTGTCTG 3′) and query invader (5′GAGTGTCCCGCGGCCCAGGA 3′) to remove non-target-bound sensors from coverslip before imaging under an objective-TIRF microscope. (**B**) The average dwell times for miR-141 bound state (high-FRET) ($\bar{\tau}_{on}$) and non-bound state (low-FRET) ($\bar{\tau}_{off}$) as a function of formamide (0-20%, v/v). (**C**) The number of candidate miR-141 bound molecules per FOV as a function of formamide after applying an optimized kinetic parameter (see SI, and Table S6). (**D**) Representative single- molecule kinetic fingerprints and N_{b+d} histograms per FOV in presence of 10 pM *EGFR*Δexon_19 without (top) and with 10% formamide (bottom). $Q_8C_6QS_{18}CS_{19}$ sensor and invaders as depicted in Figure 3A were used for this study. (**E**) The $\bar{\tau}_{on}$ and $\bar{\tau}_{off}$ for *EGFR*Δexon_19 as a function of formamide (0-20%, v/v). (**F**) The number of candidate *EGFR*Δexon_19 bound molecules per FOV as a function of formamide after applying optimized kinetic parameters (see Tables S6 and S7). All data are processed at a standard data acquisition of 10s. All data are presented as mean ± s.d., where n ≥ 3 independent experiments.

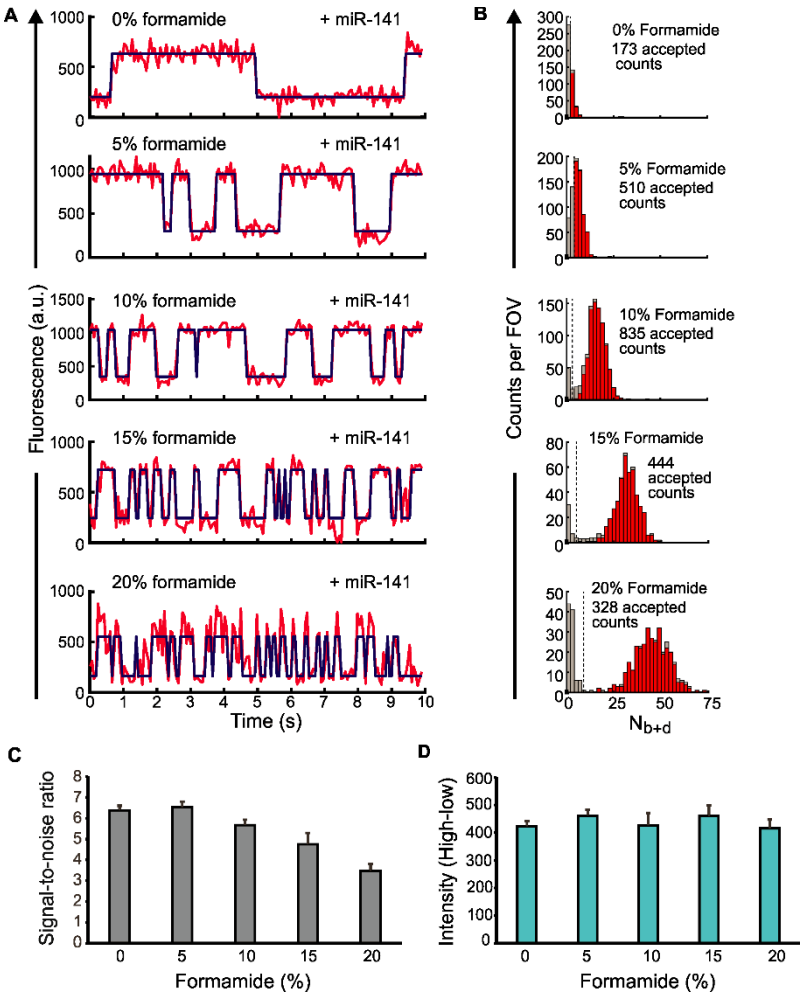

Figure 3.11. Effects of formamide on the iSiMREPS sensor for detecting miR-141. (**A**) Representative traces for the $Q_8C_6QS_{18}CS_3$ miR-141 sensor at 0, 5, 10, 15, and 20% v/v formamide. The signal is in red while the idealized trace obtained from hidden Markov model (HMM) fitting is in blue. (**B**) Histograms from 1 of 3 independent experiments for each formamide condition that show the distribution of N_{b+d} among the accepted traces. These histograms reflect the distribution after application of filters for parameters such as signal-to-noise, intensity, and min and max average dwell times. The red bars represent traces accepted while the grey bars represent traces rejected. (**C**) The average intensity difference between the high and low FRET states in the idealized hidden Markov model for each formamide condition. (**D**) The average signal-to-noise for a trace for each formamide condition. For all experiments shown, sensors were assembled at 200 nM in the presence of 5 nM miR-141. The pre-assembled sensors were then diluted it 1,000-fold and added to the surface. Imaging was performed in 4× PBS at pH 7.4. All data are presented as mean ± s.d. of 3 independent experiments.

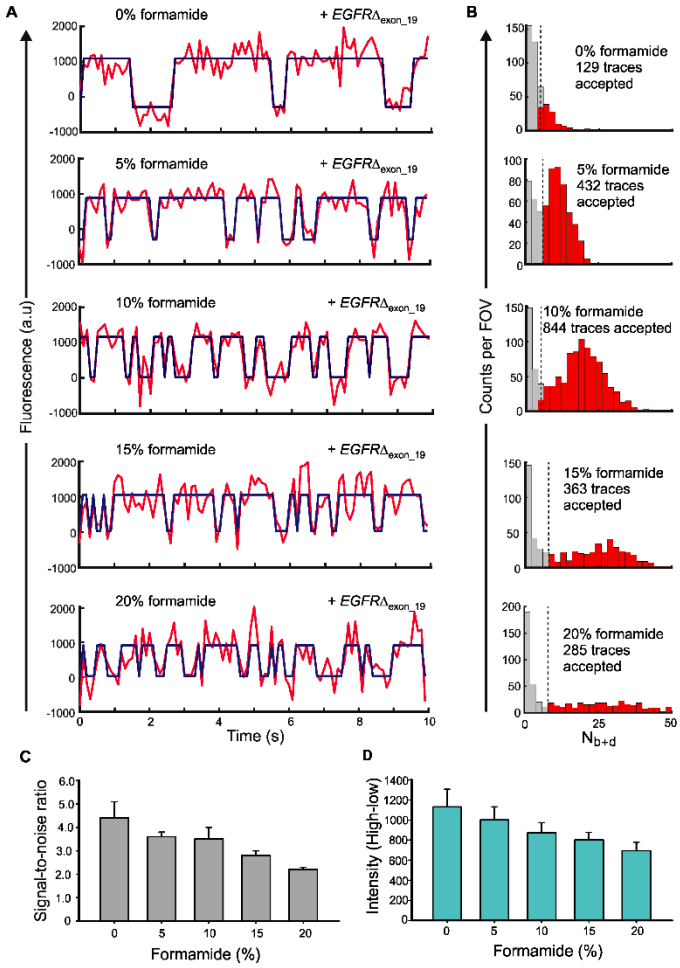

Figure 3.12. Effects of formamide on the iSiMREPS sensor for detecting *EGFR* exon 19 deletion mutant DNA (*EGFR*Δ_{exon_19}). (**A**) Representative single-molecule kinetic traces (red) with an idealized hidden Markov model (HMM) fit (blue) of the $Q_8C_6QS_{18}CS_{19}$ sensor for detecting *EGFR*Δ_{exon_19} at different formamide conditions. (**B**) Histograms of the number of candidate molecules per field-of-view (FOV) showing a given number of binding and dissociation events (N_{b+d}) after applying thresholds for FRET intensity, signal-to-noise, and dwell times of target-bound and non-target-bound states for each formamide condition. Red bars represent accepted traces while grey bars represent rejected traces. (**C, D**) The average signal-to-noise ratio (**C**), and difference in intensity of high- and low-FRET states (**D**) of the accepted traces for each formamide condition. All experiments were performed using 10 nM preassembled sensor consisting of anchor strand, capture and query probes, and 10 pM forward strands of *EGFR*Δ_{exon_19}. Imaging was performed in 4x PBS (pH 7.4) at ambient room temperature under an objective-TIRF microscope. All data are presented as mean ± s.d. of 3 independent experiments.

We next evaluated the formamide dependence of sensitivity. For miR-141 and

EGFRΔ_{exon_19}, the number of accepted traces per FOV (a measure of assay sensitivity) increased

with increasing formamide up to 10%, then decreased at higher formamide concentrations (**Figures 3.10C and 3.10F**). The accepted counts for 0 and 5% formamide likely underrepresented the number of true molecules because many target-bound sensors could not be effectively differentiated from the background in the 10 s data acquisition period (**Figures 3.11-3.12**). The lower number of counts observed in 15 and 20% formamide likely occurred because the reduced stability of the duplexes at these percentages decreases S/N and shortens some events to below the camera exposure time (**Figures 3.11-3.12**). We thus used 10% formamide during subsequent sensor optimization for maximizing sensitivity and specificity.

3.3.6 Establishing iSiMREPS Sensitivity and Specificity

To further improve *EGFR*Δ_{exon_19} detection sensitivity, we next optimized iSiMREPS preparation procedures and assay conditions (e.g., sensor concentration, invaders, target incubation time) (**Figure 3.13**). Since *EGFR*Δ_{exon_19} exists in double-stranded (ds) DNA form in biofluids, the target was thermally denatured at 90˚C for 3 min and cooled at room temperature in the presence of an auxiliary probe that binds stably to the forward strand of mutant DNA (Figure 3A). During this step, the poly-dT (dT_{30}) was included in high molar excess as a carrier[66]. The auxiliary probe and dT_{30} help keep the capture region of the target DNA in an ssDNA form, permitting efficient and specific capture. Experiments using mutant ssDNA and dsDNA treated with the above denaturation steps showed similar results (**Figure 3.14A**). The iSiMREPS assay for the *EGFR*Δ_{exon_19} dsDNA was found to have a LOD of 3.2 fM in buffer (**Figure 3.14B**) and a linear dynamic range spanning ~4 orders of magnitude (Figure S13A), a ~1.5-fold improvement over conventional SiMREPS[66]. *EGFR*Δ_{exon_19} detection in the presence and absence of a large ($10^{5\text{-}6}$-fold) excess of wild-type DNA showed 99.9996-99.9999% specificity for, permitting mutant detection at an allelic fraction of 0.001-0.0001% (**Figure 3.13**, **3.14C** and **Table 3.5**). The

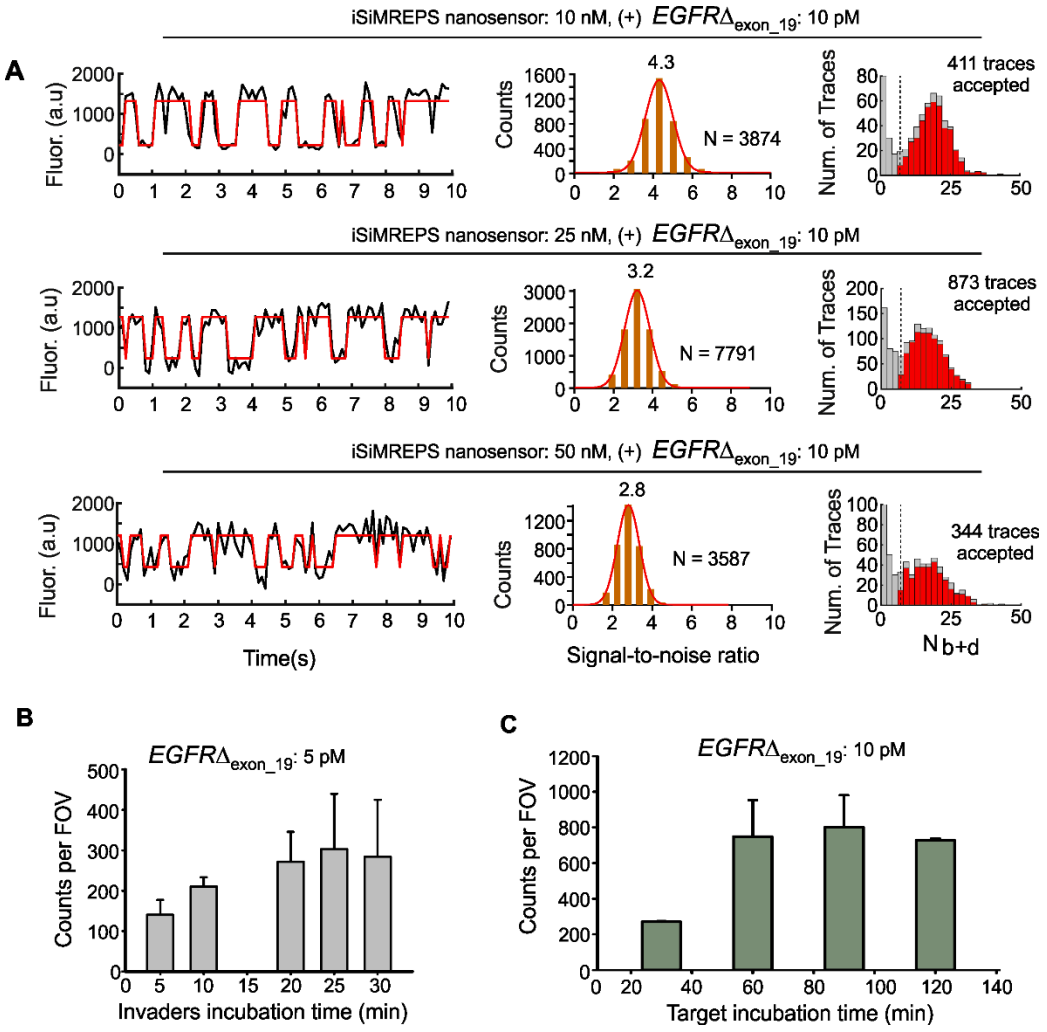

Figure 3.13. Optimization of iSiMREPS assay conditions to enhance sensitivity for detection of *EGFR* exon 19 deletion mutant DNA (*EGFR*Δ_{exon_19}). (A) Effect of sensor concentration on signal-to-noise ratio (S/N) and the number of accepted traces. The experiment was performed using 10, 25, and 50 nM sensor (incubation: 30 min), 10 pM forward strands of *EGFR*Δ_{exon_19} (incubation: 90 min), and 2.5 µM invaders (incubation: 20 min). (B) Effect of invaders incubation times on accepted traces. The experiment was performed using 25 nM sensor (incubation: 30 min), 5 pM forward strands of *EGFR*Δ_{exon_19} (incubation: 90 min), and 2.5 µM invaders (incubation: 5, 10, 20, 25, 30 min). (C) Effect of target incubation times on accepted counts. This experiment was performed using 25 nM sensor (incubation: 30 min), 10 pM forward strands of *EGFR*Δ_{exon_19} (incubation: 30, 60, 90, and 120 min), and 2.5 µM invaders (incubation: 25 min). All experiments were performed using the sensor $Q_8C_6QS_{18}CS_{19}$. All data are presented as mean ± s.d. of 2 independent experiments.

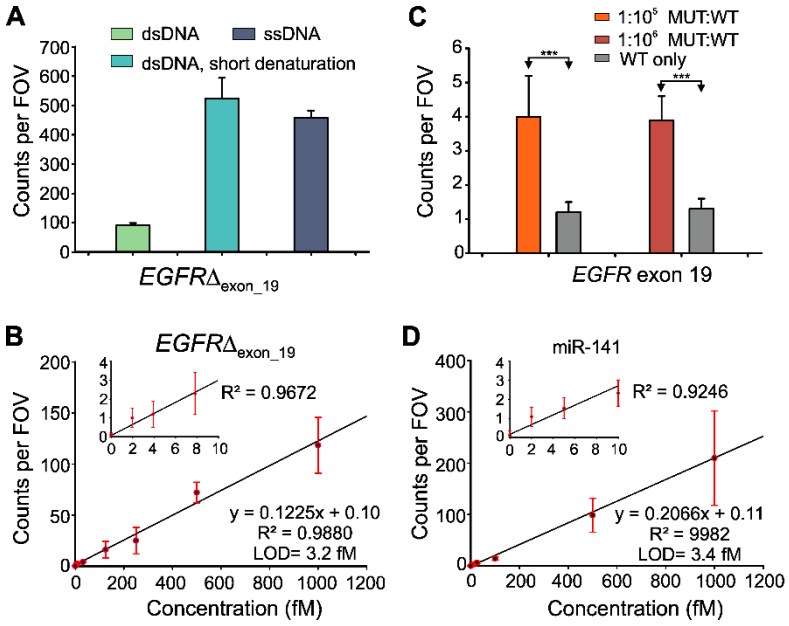

Figure 3.14. Standard curve and specificity of detecting *EGFR* exon 19 deletion (*EGFR*Δ$_{exon_19}$) and miR-141. (**A**) Effect of short thermal denaturation on the accepted counts of *EGFR*Δ$_{exon_19}$ duplex DNA (dsDNA). (**B**) Standard curve for *EGFR*Δ$_{exon_19}$ showing a LOD of 3.2 fM. Linear fits were constrained to a y-intercept of accepted counts at 0 fM. (**C**) Comparison of counts from low MUT allelic fraction and WT only conditions for determining specificity. Triple asterisks indicate the significant differences at 95% confidence levels as assessed using a two-tailed, unpaired t test and showed a specificity of 99.9996-99.9999% over the MUT fraction of 0.001-0.0001%. (**D**) Standard curve for miR-141 showing a LOD of approximately 3.4 fM. Linear fits were constrained to a y-intercept of accepted counts at 0 fM. All data are presented as mean ± s.d., where n ≥ 3 independent experiments.

Mutant allele (%)	MUT (fM)	WT (nM)	C_{WT}/C_{MUT}	Counts ± s.d. in MUT +WT (n = 4)	Counts ± s.d. in WT-only (n = 4)	Specificity (%) = $[1 - \frac{FP}{TP \times (C_{WT}/C_{MUT})}] \times 100$
0.001	500	50	10^5	4.0 ± 1.2	1.2 ± 0.3	99.9996
0.0001	500	500	10^6	3.9 ± 0.7	1.3 ± 0.3	99.9999

Table 3.5. Calculation of specificity for detecting *EGFR* exon 19 deletion mutant DNA (*EGFR*Δ$_{exon_19}$).

miR-141 assay exhibited an LOD of 3.4 fM (**Figure 3.14D**) with a dynamic range of approximately 3.2 orders of magnitude (Figure S13B), a 1.2-fold improvement over conventional SiMREPS[64] ,with similar sensitivity in one 60th of the time. Overall, iSiMREPS shows slightly lower sensitivity than some existing technologies for detecting nucleic acids like droplet digital PCR[48, 107] and NGS[108]. However, it exhibits superior specificity, comparable or better dynamic range than existing single-nucleic acid detection techniques[109] and achieves rapid detection with lower risk of cross-contamination, an elimination of sequence bias or inhibition due to enzymatic amplification, and a lack of need for purification, complex sample preparations or enzymatic reactions compared to existing techniques.

3.4 Discussion and Summary

In this chapter, iSiMREPS was developed into a full assay with the ability to detect both a DNA and RNA target with a limit of detection ~3fM, linear dynamic range of 3.2-3.5 orders of magnitude, and only 30 s of imaging time, a 60fold improvement over the original SiMREPS. This was accomplished by implementing a TMSD strategy to improve signal to noise by removing noisy signal from biosensors without a bound target and utilizing formamide in the imaging buffer in order to achieve the desired sensitivity within the short imaging time. This chapter showed that it was possible to adapt the standardized design utilized for miR-141 more generally as detection for a completely different target was possible with it and that further development into a diagnostic assay for targeted, quick results for nucleic acids of interest was possible for this iSiMREPS. This chapter also further cemented the benefit of using a biosensor approach as the formamide optimization was only possible because both states were directly controllable via the sensor design and the TMSD strategy was also a viable option for similar reasons.

When compared to existing technologies, iSiMREPS shows slightly lower sensitivity than some existing technologies for detecting nucleic acids like droplet digital PCR[48, 107] and NGS[108]. However, it exhibits superior specificity, comparable or better dynamic range than existing single-nucleic acid detection techniques[109] and achieves rapid detection with lower risk of cross-contamination, an elimination of sequence bias or inhibition due to enzymatic amplification, and a lack of need for amplification, purification, complex sample preparations or enzymatic reactions compared to existing techniques. With further development on actual clinical samples and a polished and well-refined scheme for detecting multiple targets, it is conceivable for it to become a clinically useful liquid biopsy tool.

Chapter 4. Multi-target iSiMREPS Detection

4.1 Introduction: Multi-target Assay Rationale

iSiMREPS as demonstrated in the previous chapter has the sensitivity, specificity, and speed necessary to be effective as a liquid biopsy assay. Additionally, Chapter 3 demonstrated that iSiMREPS can be adapted and modified for the detection of 2 very different nucleic acid targets individually and was capable of more general utility in detecting many different kinds of nucleic acid targets. The next step in order to maximize its potential for liquid biopsy applications is developing a deeper understanding of design considerations for iSiMREPS so that a biosensor can be readily created for any nucleic acid of interest as the ability to detect multiple targets of interest a will be necessary for it to be an effective assay in a diagnostic setting and desirable in a research setting. Additionally, multi-target detection in a single assay run would be a desirable quality since biomarker panels are commonly used in clinical settings and since there is also variance in miRNAs levels between different patients both healthy and with disease, a multi-target, panel design would also be desirable [110, 111]. To this end, perfecting the design for additional targets and devising a setup that allows for multiple targets to be detected in a single round of imaging was needed. In this chapter, the design of sensors for members of the miR-17/92 cluster, also known as oncomiR-1, will be demonstrated in detail alongside the process of developing and optimizing those designs. The design decisions necessary for effective performance, the influence that certain design choices in the biosensor have on performance, and

the design guidelines for creating an effective design are outlined here. Additionally, this chapter will outline the results obtained for each design and the implications for multi-target detection as well as outline a 3D printed well multi-target detection approach.

4.2 Methods

4.2.1 Materials and Nucleotides

The same materials outlined in **Section 2.2.1** are also used in this chapter and T_m calculations are done in the same manner outlined in **Section 2.2.1**. The nucleic acid strands utilized in this chapter are listed below in **Table 4.1**.

ID	Sequence: 5´-3´	Usage
miR-17	CAAAGUGCUUACAGUGCAGGUAG	hsa-miR-17-5p
miR-18a	UAAGGUGCAUCUAGUGCAGAUAG	hsa-miR-18a-5p
miR-19a	UGUGCAAAUCUAUGCAAAACUGA	hsa-miR-19a-3p
CP1_ miR-17	/5AmMC6/T+G+TAAG+CACTTTGTTTGGC GGAGTGTCC	CP for 1st generation miR-17 biosensor
CP2_ miR-17	/5Cy3/+TG+TA+AGCACT+TTTTTGGCGGA GTGTCC	CP for 2nd and 3rd generation miR-17 biosensors
QP1_ miR-17	CGCGGCCCAGGATTTTTTTTTTTTTTTTT CTACCTGC/3AlexF647N/	Standard CP for miR-17 biosensors
QP2_miR-17	CGCGGCCCAGGATTTTTTTTTTTTTTTTT CTACCTG/3AlexF647N/	CP for miR-17 biosensors with 7 nt target binding region and one less G-C base pair
Anchor1_miR-17	TTAGGTAGTTTTCCTGGGCCGCGGGACA CTCCGCCTTTTTTTT/3BioTEG/	Standard Anchor for miR-17 biosensors

Anchor2_miR-17	TTCAGGTAGTTTTCCTGGGCCGCGGGAC ACTCCGCCTTTTTTTT/3BioTEG/	Anchor for miR-17 biosensors with extra base to give 7 nt query binding region
CP1_ miR-19a	CCTGTGAGGCGGTTTTC+A+GTT+TTGC/3 Cy3/	CP for 1st generation miR-19a biosensor
CP2_ miR-19a	CCTGTGAGGCGGTTTTC+A+GT+T+TTGC/ 3Cy3/	CP for 2nd and 3rd generation miR-19a biosensors built for SNV discrimination
CP2_miR-19a	CCTGTGAGGCGGTTTTC+A+GT+T+TTGC AT/3Cy3/	Standard CP for 2nd and 3rd generation miR-19a biosensors
QP1_ miR-19a	/5Alex647N/AGATTTGCTTTTTTTTTTTTTT TTTTAGGACCCGGCGC	QP for miR-19a biosensors built for SNV discrimination
QP2_miR-19a	/5Alex647N/ATTTGCACTTTTTTTTTTTTTT TTTTAGGACCCGGCGC	Standard CP for miR-19a biosensors
Anchor1_miR-19a	/5Biosg/TTTTTTTTCCGCCTCACAGGGCGC CGGGTCCTTTTGCAAATTT	Standard Anchor for 1st and 2nd generation miR-19a biosensors
Anchor2_miR-19a	/5Biosg/TTTTTTTTCCGCCTCACAGGGCGC CGGGTCCTTTAGCAAATTA	Anchor for 3rd generation miR-19a biosensors adjusted for unwanted base pairs
CP_miR-18a	/5Cy3/AG+A+TGCA+C+CTTATTTGGCGGA GTGTCC	CP for miR-18a biosensors
QP_miR-18a	CGCGGCCCAGGATTTTTTTTTTTTTTTTT TATCTGCA/3AlexF647N/	QP for miR-18a biosensors

Anchor_18a	ATCAGATATTTTCCTGGGCCGCGGGACA CTCCGCCTTTTTTTT/3BioTEG/	Anchor for miR-18a biosensors
CI_{mis} for miR-17	TCCGCCATAAAAGTGCTTACA	Capture Invader for miR-17 CP with spacer mismatch
QI for miR-17 and miR-18a	GAGTGTCCCGCGGCCCAGGA	Query Invader for miR-17 and miR-18a biosensors
CI_{mis} for miR-19a	ATGCAAAACTGAATACCGCCT	Capture Invader for miR-19a CP with spacer mismatch
QI for miR-19a	AGGACCCGGCGCCCTGTGAG	Query Invader for miR-19a biosensors
CI_{mis} for miR-18a	TCCGCCATATAAGGTGCATCT	Capture Invader for miR-18a CP with spacer mismatch

Table 4.1. Sequence of all nucleotides used in this chapter with their intended purpose. Binding regions are underlined.

4.2.2 Assay Preparation and Imaging

The assay preparation protocol outlined in **Section 2.2.4** that utilized bBSA for P-TIRF was utilized here for all experiments outlined in **Section 4.3.1-4.3.3** using the O-TIRF microscope and imaging protocol as outlined in **Section 3.2.2** on an Oxford Nanoimager (ONI, ONI Inc.) O-TIRF setup. All of these experiments used bBSA, 100 pM sensor, 5 pM target, and no formamide or invaders if run on the ONI setup. The ONI imaging was done with a 60 ms exposure time on a setup with a z-drift correction module, autofocusing, and a laser intensity at around 10% with varying levels of power at a temperature of 26-28°C. Due to the poor control of the laser intensity and temperature variance, the ONI configuration was used more for observations and qualitative data. All O-TIRF experiments in **Section 4.3.5** utilized the

procedures outlined in **Sections 3.2.2-3.2.5** for adding target separately from the biosensors with 2 pM target concentration.

4.2.3 Non-denaturing Polyacrylamide Gel Electrophoresis

Non-denaturing gel experiments in this chapter were performed in the same way outlined in **Section 2.2.8** with a Biometra multigel setup (846-010-200).

4.2.4 3D Printing of Multi-Target Wells

The wells in **Section 4.4** were 3D printed using a Stratasys J750 polyjet 3D printer with veroclear as the material. The wells were designed in CAD Fusion Autodesk with exact specifications for height, length, and width for all parts including the thickness of outer wall, the length of the inner well chamber, the placement of 2 dividers to separate the inner chamber into 4 well compartments and the divider thickness and height to determine the firmness of the design and the maximum sample volume. The dimensions of the 2 wells described in **Section 4.3.6** with the general design depicted there are detailed in **Table 4.1** below. The wells were glued to a coverslip using epoxy (Ellsworth adhesives, hardman double, catalog no. 4001) while being pressed down on from the top by a PanaVise base with a self-centering, extra wide opening head attachment (Models 300 and 376) to ensure a stronger seal and no leaking of sample to the outside of the wells.

Dimension	Well Design 1	Well Design 2
Outer wall thickness (mm)	0.2	0.5
Total base length/width (mm)	9.52	8.9
Outer wall height (mm)	12	8.4
Divider Thickness (mm)	0.12	0.5
Well length/width (mm)	4.5	3.7
Well height (mm)	10	8

Well surface area (mm^2)	20.25	13.69
Well volume (μL)	202	109

Table 4.2. Dimensions and specifications for 3D-printed well designs

4.3 Results and Discussion

4.3.1 Developing miR-17 iSiMREPS Biosensor and Clarifying Design Principles

The miR-17/92 cluster was chosen for clarifying design considerations and optimizations for iSiMREPS sensors across additional targets for a few different reasons. The first is that this cluster would be a viable target for a panel assay because all 6 of its member miRNAs are collectively called oncomiR-1 because of their strong involvement in cancer pathways and their biomarker potential for B-Cell lymphoma[112]. Another reason is that this clusters miRNAs have relevant differences that translate into design differences and would make this cluster a good test case for multi-target detection. Two major ones include varying GC content that translates into changes in dwell times for both states, a pair of single nucleotide variants (SNVs) and sequence similarities that pose challenges in specificity and design for binding sequences that will come up more generally when designing iSiMREPS assays. Thus, miR-17, miR-19a, and miR-18a were chosen among the cluster as targets for further development with miR-17 having a higher GC count, miR-19a being one of a pair of SNVs, and miR-18a being more complex in terms of design specification as will be outlined below.

The first design chosen for the detection of miR-17 as outlined in **Figure 4.1A** was selected based on the standardized design outlined for miR-141 and *EGFR*Δ_{exon_19} in the previous chapter in terms of QS length and the lengths of the QP-target, CP-target, and CP-competitor binding regions. The CP chosen for this design had only 3 LNA residues and was chosen as the CP-target region had a T_m of 64°C which would be sufficient to bind it strongly under room temperature imaging conditions and had a mismatch in the spacer region for the invaders which,

as outlined in Chapter 3, would allow for more effective removal by the invader strands. The QP-target interaction was kept at the same length as was the length of the query spacer as these

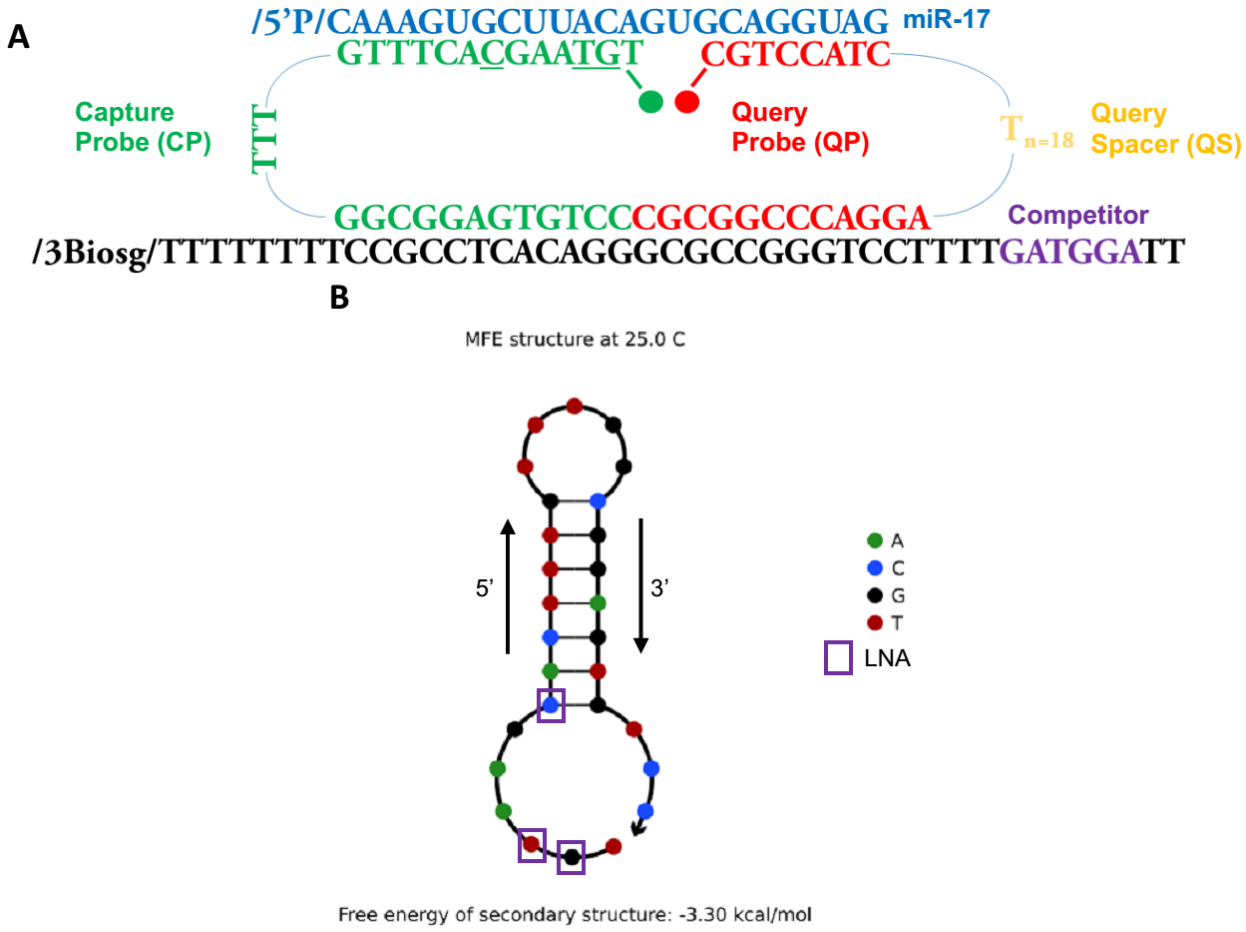

Figure 4.1. The initial, 1st generation miR-17 iSiMREPS design and data used for troubleshooting it. (A) The miR-17 iSiMREPS sensor is as depicted and shares the same basic design elements as the biosensor for miR-141 with the respective bases for miR-17 complementarity. (B) NuPACK[93, 94] simulation of the CP which reveals secondary structure and has both the bases and the LNA-modified residues marked.

choices were found previously to be effective and standardizable and changes from sequence content would require further experimental determination to assess their effect. This design, however, did not function properly as almost no molecule spots were detected when this was

imaged under the ONI using the preassembly protocol and 100 pM sensor concentration as outlined in **Section 4.2.2**. This indicated that there could be potential issues with the assembly or RNA capture as these conditions do not permit significant crowding and noisy signals and a lack of spots indicates that FRET does not occur rendering spot finding poor. Any gels run on this biosensor did not show stable assembly and capture, indicating that there could be issues with unexpected secondary structure in the CP. Upon evaluating the CP using NUPACK[93, 94] for the full CP sequence, it was shown that the CP for this design had an 8 nt hairpin structure that overlapped with an LNA residue (**Figure 4.1B**) and did not show disassembly until reaching a temperature within the 50-55°C range. Since this NUPACK[93, 94] model could not account for the additional strength afforded by LNA residues, it indicated a need for redesigning the CP entirely as a higher temperature was insufficient to preempt this problem. Additionally, when the CP-target sequence was evaluated in Qiagen's LNA Oligo Optimizer[87], it obtained a hybridization score of 33 which indicated a vulnerability to binding to other strands of itself and some of the residues responsible for this contained LNA.

To address these problems with secondary structure, the CP was redesigned as shown in **Figure 4.2A**. The G-C base pair on the 5' end of the miR-17 was eliminated entirely because this pair contributed significantly to the secondary structure observed in **Figure 4.1B** and its removal reduced the secondary structure to only a 4 nt hairpin as seen in **Figure 4.2B**. This new design had a hybridization score of only 25 as the change in LNA placement and removal of the extra G-C residue mitigated the self-binding issue the first design had. The LNA residue placement was also changed to prevent any overlap with the secondary structure in order to ensure that it remained weak and could readily be denatured during the heating step of regular sample preparation. This new CP segment had a T_m of 63°C and was expected to have sufficient

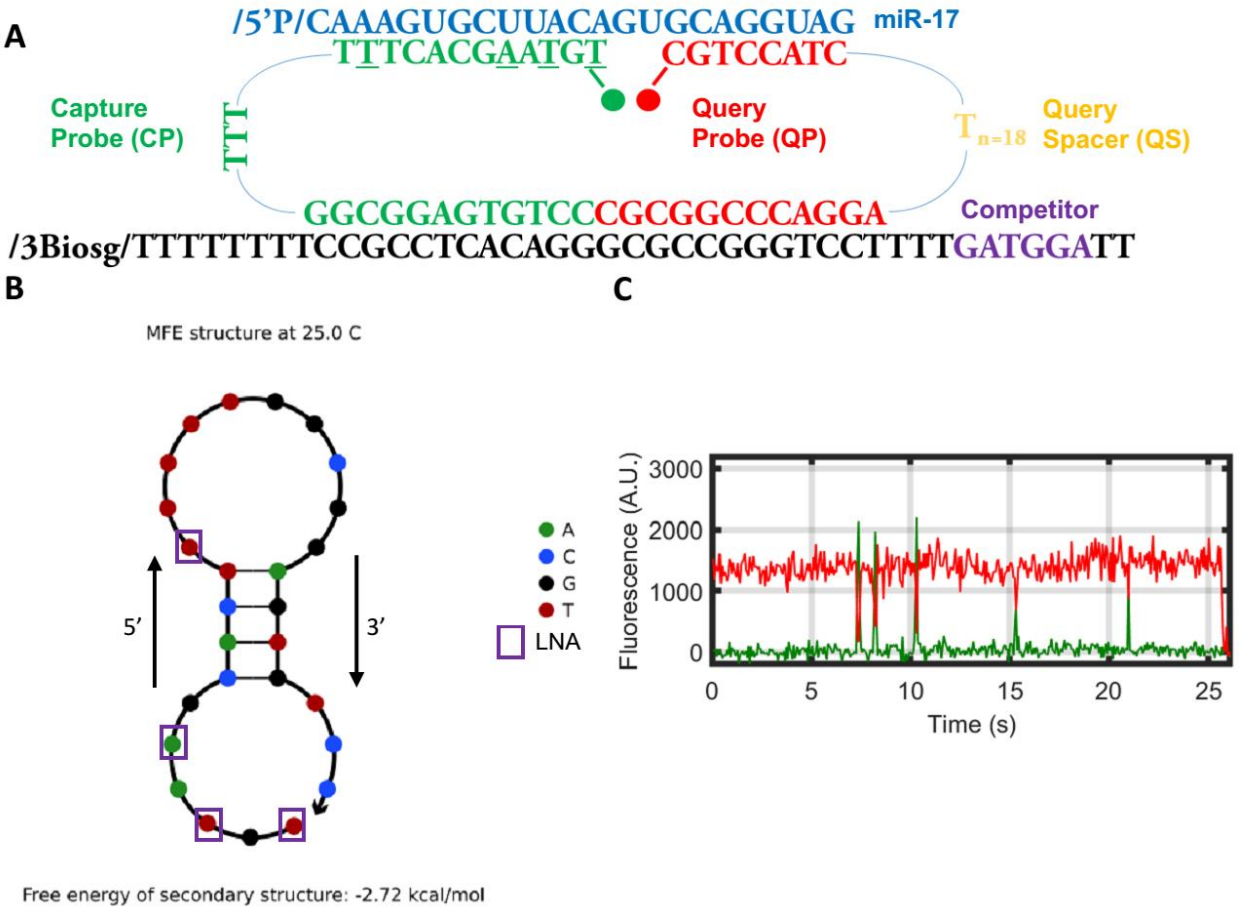

Figure 4.2. The revised, 2nd generation miR-17 design created to alleviate secondary structure issues with the CP and allow for signal generation. (A) The revised miR-17 iSiMREPS sensor is as depicted and removed the 5' GC base pair with miR-17 in order to alleviate secondary structure problems and added 1 LNA with LNAs being spaced out for strong capturing of the miR-17 RNA. (B) NUPACK[93, 94] simulation of the CP which shows changes in secondary structure and is marked with LNA-modified nucleotides. (C) Example trace seen for this biosensor when imagined under the ONI O-TIRF microscope at 5 pM miR-17 and 100 pM sensor without formamide at an elevated temperature around 27-28°C.

binding strength for capture. This new design was tested on the ONI O-TIRF setup as outlined in **Section 4.2.2** and the traces observed showed a very strong high-FRET bias (**Figure 4.2C**). This result can be explained by the high number of GC residues for this QP-target sequence (5) vs that of the QP-target sequence for the miR-141 biosensor (3). Additionally, the T_m for the

QP-target sequence for this biosensor was 36.3°C vs 30.2°C for the miR-141 QP-target sequence. These differences would translate to a strong QP-target interaction and thus a stronger preference for the high-FRET state.

Given the issues of high FRET dominance described for the miR-17 redesign, changes to the QP-target and QP-competitor interactions to achieve parity were needed. This could be accomplished by weakening the strength of the QP-target interaction or strengthening the QP-competitor interaction so that there was less bias in favor of the high-FRET state. A redesign of the miR-17 biosensor for each approach is depicted in **Figure 4.3.** In the design on the left (**Figure 4.3A**), the competitor strand length was increased from 6 nt to 7 nt to raise the T_m from 5 to 11.4°C in order to increase the strength of the QP-competitor interaction and bring the dwell times of both states closer to each other. For the design on the right (**Figure 4.3B**), a GC base pair on the 3' end of the CP was removed in order to reduce the T_m of that target-QP interaction from 36.3 to 21.8°C so that this interaction was weaker and easier to transition away from. While the lengthening of the competitor strand did lengthen low-FRET dwell times, it did not effectively address the high-FRET bias and only served to create long overall dwell times (**Figure 4.3C**). On the other hand, shortening the length of the QP-target sequence dramatically reduced the high-FRET binding dwell time and resulted in traces with significantly improved parity as well as very short binding dwell times that would be ideal for quick fingerprint generation (**Figure 4.3D**). Reducing the target-QP interaction was thus preferable because it achieved the parity alongside lower overall dwell times and this choice fixed the problem of long high-FRET dwell times which increasing the competitor did not have a strong effect on. Thus, the biosensor depicted in **Figure 4.3B** was chosen as the design for further detection.

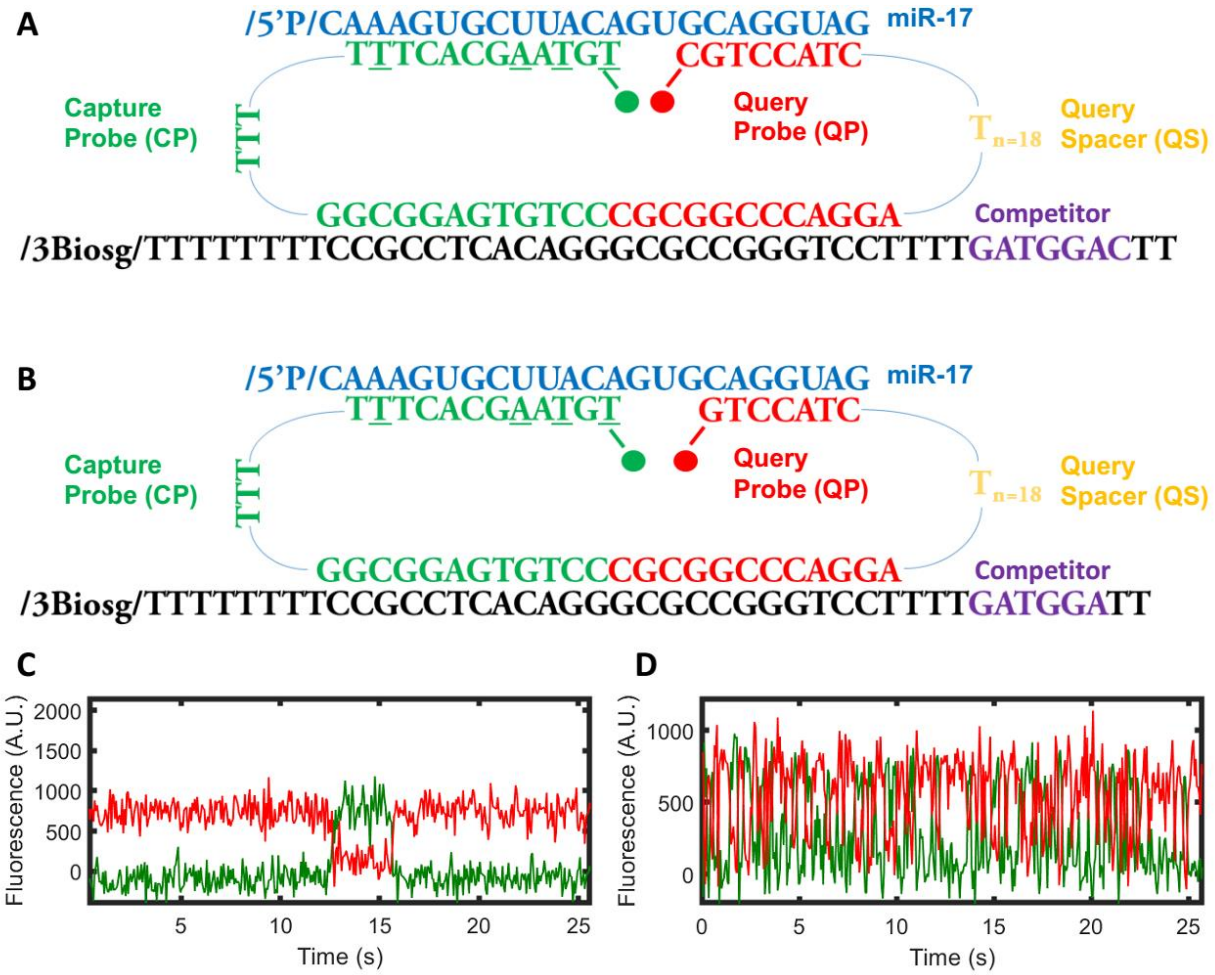

Figure 4.3. The 3rd generation miR-17 designs created in order to address the overwhelming high-FRET bias of the previous design in Figure 4.2. (A) This design adds an extra nucleotide to the competitor to give a 7 nt competitor. (B) This design removes the 3' C that was in Panel A in order to weaken this interaction and achieve greater parity between FRET states. (C) Trace from imaging of the sensor depicted in Panel A. (D) Trace from the imaging of the sensor depicted in panel B. Both of the traces shown in Panels C and D were from imaging experiments that used the ONI O-TIRF microscope with 5 pM miR-17 and 100 pM sensor without formamide or invaders at an elevated temperature around 27-28°C.

4.3.2 Developing miR-19a Biosensor and Solidifying Design Guidelines

The initial design chosen for the detection of miR-19a is depicted in **Figure 4.4A** and similarly to the initial miR-17 design, was based on the standardized design outlined in chapter 3 for miR-141 and *EGFR*Δ_{exon_19}. The CP for this design was chosen because it had a T_m value of

64°C which appeared to be more than enough to ensure a strong capture of the target strand at the imaging temperature and just like with miR-17, had a mismatch in the invader strands designed for this biosensor to achieve best S/N improvement. This design, however, changed the placement of the QP-target sequence to coincide with the final A-U base pair on the 5' end of the CP because this is the only base pair difference that distinguishes miR-19a from miR-19b and this design would allow the QP sequence to differ for that nucleotide and allow these SNVs to be distinguished. The 5' and 3' ends of all the strands in this design were also inverted compared to the designs for miR-141 and miR-17 in order to more reasonably accommodate this shifting of the QP sequence to coincide with that A-U base pair and maintain the same distance between fluorophores as well as an anti-parallel configuration. The competitor length was left unchanged for this initial design given that this length was sufficient for 3 different target designs previously. When imaged, however, this biosensor could not be focused at all under the O-TIRF microscope outlined in **Section 3.2.2** and when imagined under the ONI O-TIRF microscope as outlined in **Section 4.2.2**, it showed only low-FRET behavior if at all and when directly excited, molecules could be immediately seen in the Cy3 channel (**Figure 4.4B**). This indicated that the biosensor was able to assemble as signals from direct excitation were present but that there were problems preventing FRET from occurring. Since these observations would be consistent with problems specifically in the target interactions with the biosensor, a gel was run to determine the strength of capture and structural assembly of the biosensor and miR-19a. This gel showed demonstrably poor capture of the target by the CP as shown by smeared bands both with only target and CP and with all sensor components combined in Lanes 5 and 7 (**Figure 4.4C-D**). These results indicated that the CP needed to be redesigned and that the calculated T_m value was not necessarily a guarantee of good capture.

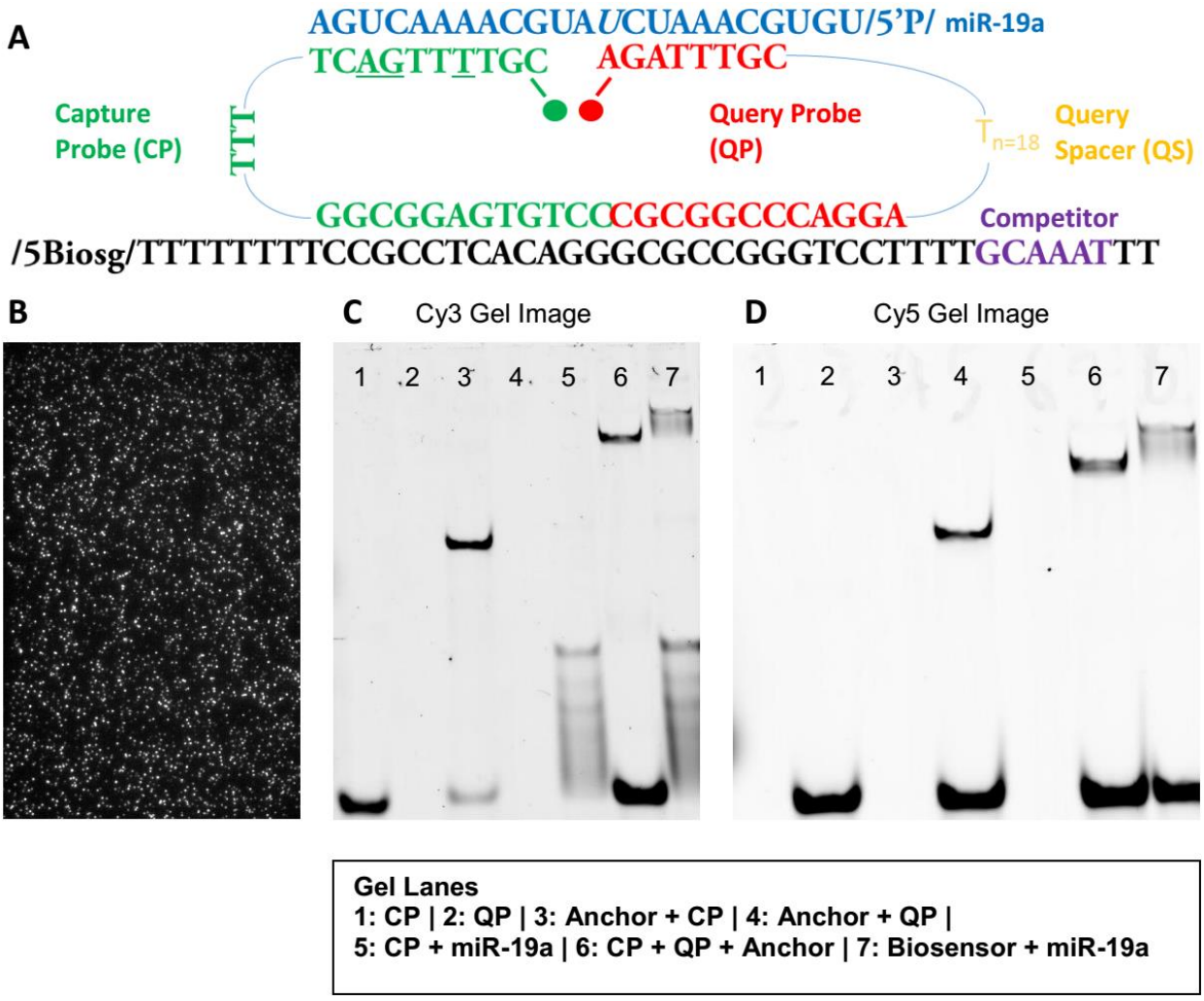

Figure 4.4. 1st generation miR-19a design with initial result and troubleshooting of performance. (A) The initial miR-19a design which was based on the standardized design for miR-141 and had a shifted placement of its QP to coincide with the italicized uracil which is the only residue that differs between miR-19a and miR-19b (B) Field when Cy3 channel was directly excited when imaged under ONI O-TIRF microscope with 5 pM miR-17 and 100 pM sensor without formamide or invaders at an elevated temperature around 27-28°C. (C) Cy3 imaging of Gel for miR-19a biosensor component assembly and target binding (D) Cy5 imaging of Gel for miR-19a biosensor component assembly and target binding.

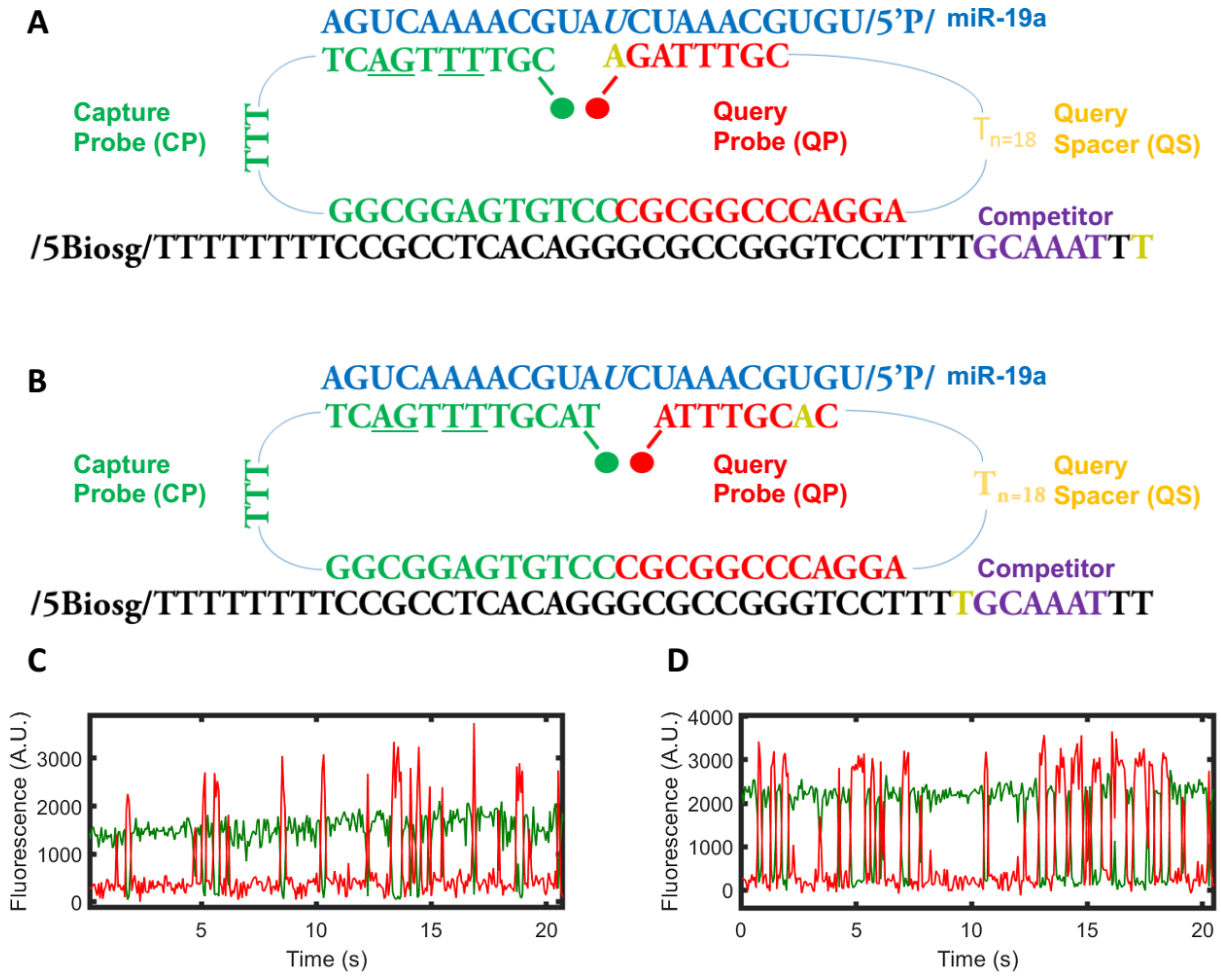

Figure 4.5. 2nd generation miR-19a designs. (A) The new design added an extra LNA residue to the CP in order to strengthen the binding to the target. (B) This design was closer to the miR-141 original and also had the CP modification and was not designed for distinguishing single nucleotide variants like the Panel A design. (C) Panel A sensor trace. (D) Panel B sensor trace.

Two redesigned biosensors were created with an extra LNA residue added to the biosensor to improve target capture and a second design with the CP lengthened and the QP moved back to the standardized design position it held previously were made to assess the feasibility of the SNV discrimination and see if target capture was meaningfully improved (**Figure 4.5**). The new CP for the design on the left had a T_m of 71°C (**Figure 4.5A**) while the design on the right had one of 70°C (**Figure 4.5B**). While both designs showed FRET signal indicating the improvement in target capture was successful and the high-FRET dwell times

looked similar to those expected from miR-141 (T_m of 21.1 for **Figure 4.5A** and 23.3 for **Figure 4.5B**), they also showed unnaturally long low-FRET dwell times (**Figure 4.5C-D**). Upon closer examination of the biosensor structure, this result was due to unwanted complementarity of QP nucleotides outside the QP-competitor region as indicated in Yellow on **Figures 4.5C-D** for both

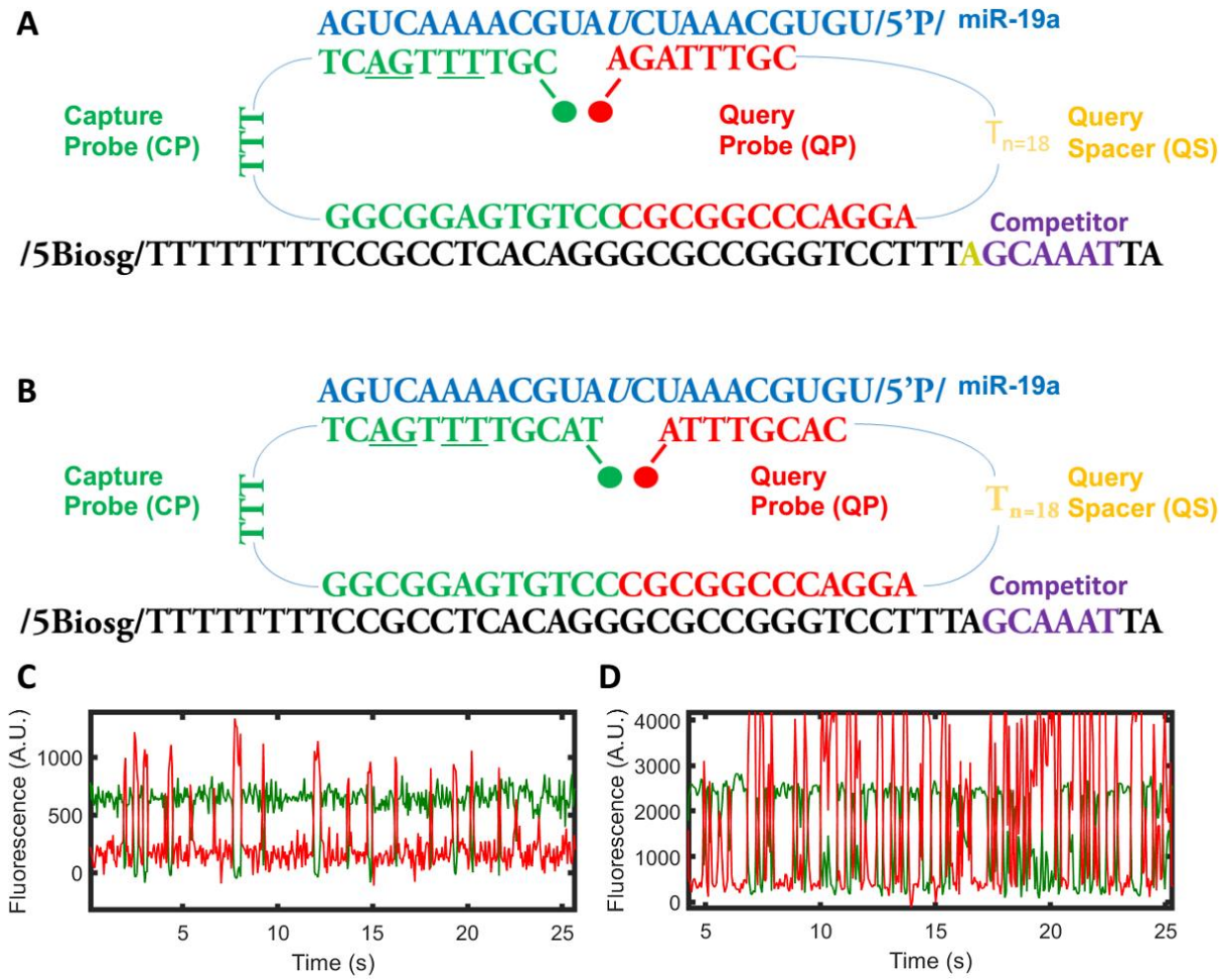

Figure 4.6. Final miR-19a designs. Both designs changed the anchor to add adenine residues in place of thymines at the yellow highlighted spots on the anchor in Figures 4.5A-B (A) The single nucleotide variant design. The residues in yellow indicates an unexpected base pair with the QS thymine. (B) Final design closer to the miR-141 original with modified bases and no unwanted complementarity. (C) Panel A sensor trace. (D) Panel B sensor trace.

designs which resulted in the low-FRET state being more stable than expected and it have a longer, less optimal dwell time.

Given these problems, the anchor strand for these biosensors was redesigned so that the thymine bases on the anchor at the positions highlighted in yellow in **Figure 4.5A-B** were replaced with adenines to prevent unwanted base pairing of those nucleotides with the QP binding sequence (**Figure 4.6A-B**). While the new design from **Figure 4.6A** still demonstrated long low-FRET states like the prior experiments (**Figure 4.6C**), the new design from **Figure 4.6B** showed the desired behavior (**Figure 4.6D**) and was thus chosen as the design of choice for detecting miR-19a. Upon closer examination, the behavior observed for the design from **Figure 4.6A** was because changing the base to an adenine created an additional unwanted base pair with a thymine residue from the QS which resulted in stronger than usual QP-competitor binding and thus a longer dwell time. While the SNV design was not pursued further for multi-target detection, it would have been possible to correct this problem by changing the adenine to a cytosine or guanine to remove any possibility of unwanted base pairing with the QS. That design could then be tested on both miR-19a and miR-19b to determine its ability to distinguish both targets.

4.3.3 miR-18a Biosensors and Limitations Clarified

The design for miR-18a as depicted in **Figure 4.7A** was chosen based on similar considerations as the miR-17 and miR-19a designs. The LNA placement was chosen as this CP binding sequence was highly susceptible to self-structure and this particular placement was one of few to give a hybridization score (28) below the threshold of 30, which considered to be indicative of self-binding problems. The T_m of this CP was also 75°C which was more than strong enough to ensure effective capture. The QP placement and competitor length was chosen as depicted

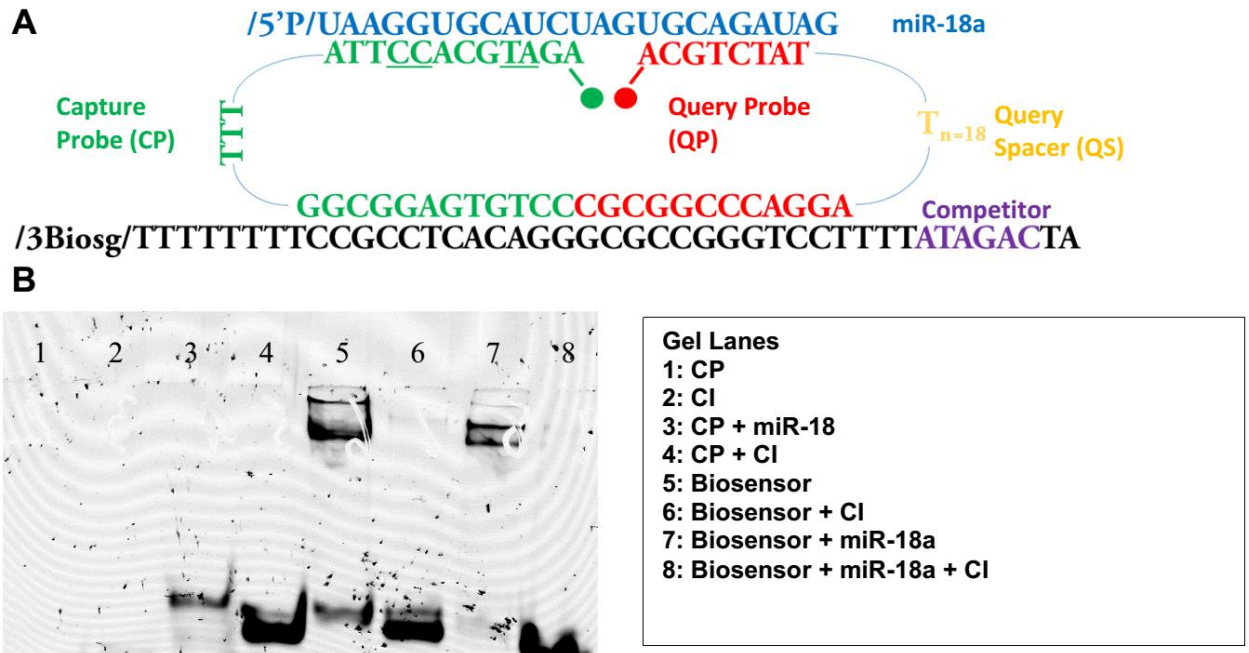

Figure 4.7. miR-18a biosensor and results. (A) miR-18a biosensor design which had the QP shifted to avoid a high number of GC pairs which create significant bias for high-FRET states as seen in **Figure 4.2** for miR-17. LNA placement and CP give minimal secondary structure and self-binding which was issue for other possibilities. (B) Gel to evaluate the target capture and the efficacy of the invaders designed for this biosensor.

in **Figure 4.7A** to keep a number of GC residues for the QP-target sequence comparable to the chosen designs for miR-141 and miR-17 as well as maintain similar competitor strength in order to achieve similar binding kinetics for both states as observed for those 2 biosensors. When imaging this biosensor to evaluate its performance using the O-TIRF setup outlined in **Sections 3.2.2-3.2.5**, a low number of molecules was detected, there were almost no counts, and the field was extremely crowded. Since there results were replicated twice, it indicated the possibility that the invader strands did not effectively remove the background noise from target-less sensors or that there were unforeseen issues with the target capture or biosensor assembly. To further

investigate this, a gel was run to evaluate not only the sensor assembly and target capture, but also the effectiveness of the first invader for this biosensor design. As shown in the gel results (**Figure 4.7B**), the CP does not effectively capture its RNA target as there are 2 clear bands in lane 3 where both are present. Additionally, the CI is shown to successfully bind to the CP as shown by its higher height and a lack of a CP only band in lane 4 where they are both together. This is further corroborated by the lane 7 where the biosensor is combined with miR-18a and it shows 2 bands indicating poor capture of the target. Lastly, when the CI is added along with the miRNA in lane 8, the only band present is in the same area as the CP-invader band in lane 4. This indicates that because the CP's capture of the target is poor, the CPs on all of the miR-18a biosensors assembled at the surface are vulnerable to removal by the invader because their CP-target sequence is far more exposed. Given the difficulties in designing this CP, it was decided that it would be simpler to move forward with multi-target detection using miR-17 and miR-19a in addition to the 2 targets already outlined in Chapter 3. The limitations observed in designing a biosensor for miR-18a, however, reveal that a deeper, more predictive understanding of the interactions within the biosensor would be helpful in creating more effective designs and concrete rules as well as improve design capabilities for difficult targets like this one.

4.3.4 Discussion of iSiMREPS Design Discoveries

These experiments conducted on these various biosensors gave insights into the factors that are important for effective iSiMREPS assay design and general guidelines that should be followed to ensure good design. One set of factors to consider is for the CP. One important factor revealed by all 3 experiments is that the LNA placement on the CP as well as how many nucleotides are LNA-modified is critical in order to minimize any unwanted influence from secondary structure as well as ensuring that there is a sufficiently strong capture. Selecting LNA

placement to avoid nucleotides within hairpins is thus one guideline for iSiMREPS biosensor design. Additionally, the experiments on miR-18a and miR-19a revealed that the T_m was not a sufficient predictor of capture strength of the CP binding sequence on its own as both of these designs had an ineffective capture despite being predicted to be bound strongly. Given the results, at least 4 LNA-modified nucleotides are recommended for the CP-target sequence. Another factor to account for in the CP was its potential for self-binding and secondary structure as this is important for ensuring that the binding regions are accessible to the anchor and target and this was evident in the initial miR-17 design where a large secondary structure interfered with the CPs ability to capture target and a nucleotide had to be removed to correct the problem. This was further evident in the miR-18a design where it was not developed further because of the difficulties incurred in designing a CP without major self-binding problems. Given these results, LNA placement and selection of the CP-target sequence should also account for self-structure and seek to keep the hybridization score within the 20-30 range for a stable structure that is also accessible.

Another important set of factors for the design of iSiMREPS biosensors are the QP and its interactions with the target and competitor. As demonstrated by both the miR-17 and miR-18a experiments, the GC content and length of the QP-target interaction is an important design choice because high GC sequences without a short length demonstrate significantly stronger dwell times and based on the data, 3 GC pairs for an 8 nt QP-target sequence work effectively as do 4 GC pairs for a 7 nt sequence. It is suggested to shift the sequence if this balance cannot be obtained. Secondly, the competitor sequence and nearby nucleotides are a vital consideration as noted in the miR-19a designs because unwanted complementary in this region can artificially lengthen low-FRET dwell times and hinder quick fingerprint generation. It is thus

recommendation to stick to 6 nt competitors to obtain desirable kinetics and monitor nearby nucleotides with base pair substitutions as needed for any unwanted complementarity. With these design rules clarified and more firmly established, iSiMREPS could be further developed for multi-target detection.

4.3.5 miR-17 and miR-19a Biosensor Performance Test

With the finalized designs selected, miR-17 and miR-19a were then tested using the standard protocol for assay preparation outlined in **Section 3.2.4** at 2 pM concentration to ascertain the performance and relatively sensitivity of both designs. As shown in **Figure 4.8**, miR-19a demonstrated exceedingly high sensitivity and consistency with an average of 1371 counts and a CV of 0.08 while miR-17 had much lower sensitivity and consistency as noted by its average of only 76, CV of 0.19, and difficulty in reliably obtaining results. These results cannot be attributed entirely to experimental variations as some of the miR-19a experiments that were successful were run on the same coverslip as miR-17 sensors where the field was too crowded to be focused. Additionally, the averages collected for the miR-17 data in **Figure 4.8** varied the invader strand incubation from 20-40 minutes. Although this varied, this should not invalidate any comparisons because we know that beyond 20 minutes, there is no significant difference in counts as seen in prior data on *EGFR*Δ_{exon_19} from **Figure 3.13B**. These results, especially when paired with the data from miR-141 and *EGFR*Δ_{exon_19} suggest that there is variability in the efficiency of capture for different biosensors that is not readily predicted by simple modeling or T_m values and may involve more complex intramolecular or imaging environment interactions. Nonetheless, these experiments served to illustrate that broad detection using iSiMREPS can be accomplished.

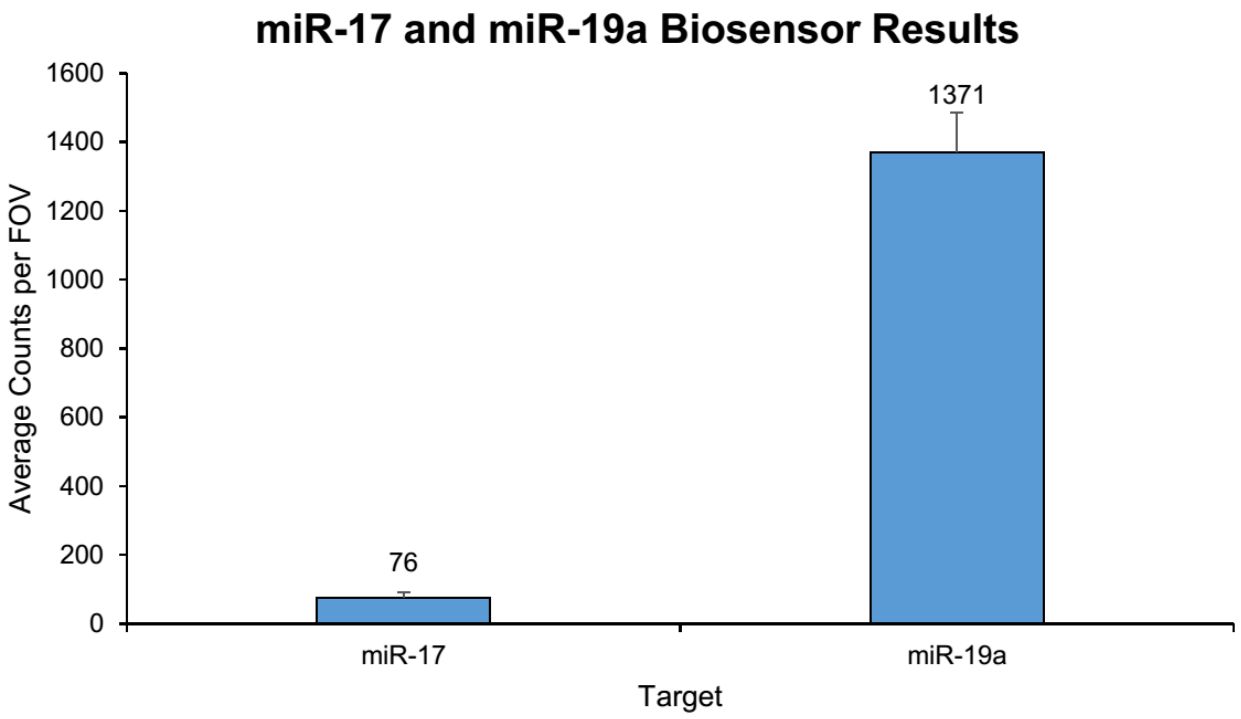

Figure 4.8. Results demonstrating the counts for the new miR-17 and miR-19a biosensor designs shown in Figures 4.3B and 4.6B respectively. Both experiments utilized the protocol for miRNA quantification outlined in Section 3.2.4 with 2 pM RNA target. The miR-17 data varied in Invader incubation time from 20-40 min. All data are presented as mean ± s.d., with n = 3 independent experiments.

4.3.6 3D-Printed Well for Multi-target Detection and Discussion

For multi-target detection, the sample well design depicted in **Figure 4.9A** was created to allow for spatial separation of 4 different iSiMREPS biosensor and detection of their respective targets in a single run of the assay. This design was chosen because it was simple, customizable, and readily usable for detection of multiple targets through implementation of automated stage shifting. By using this well design, it was easy to separate different biosensors without any need for manual spotting or a microarray printer which is more typically used for spatially separated sample[113] as the well itself provides separation and eliminates any need for spotting at specific

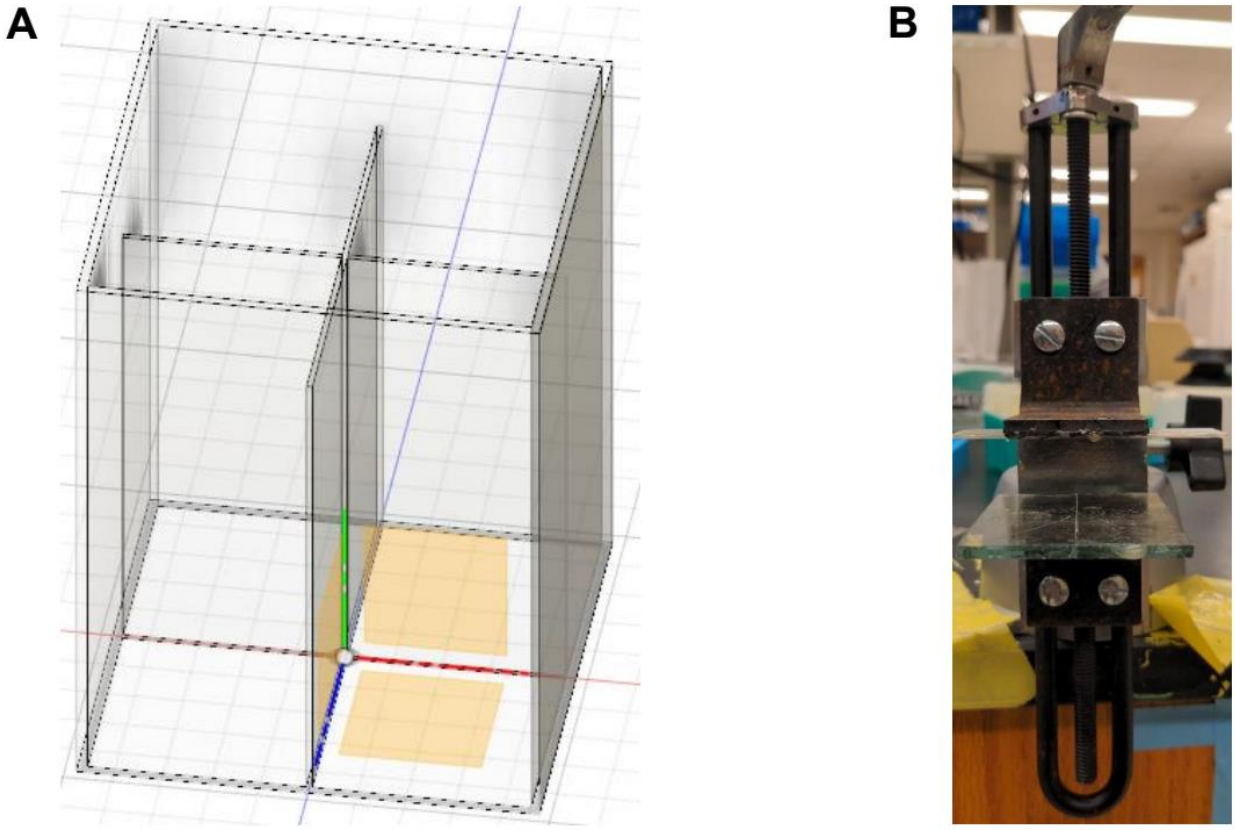

Figure 4.9. 3D Printed well design and PanaVise device to press well for gluing. (A) The 3D printed well design made using CAD Fusion Autodesk and printed with a Veraclear material on a Stratasys J750 Polyjet 3D printer. This design has 4 different compartments which can each fit their own biosensor separated by a divider. (B) This PanaVise device, as outlined in **Section 4.2.4** was used to press down on the top of the wells when using epoxy to glue them to the coverslip to strengthen sealing of the well to prevent leakage.

spaces. Additionally, the well dimensions could be readily altered and customized to allow for a specific volume of sample, a specific surface area for imaging to ensure a given density and sensitivity of detection, and a specific size or configuration suitable for different workflows or samples such as introducing a single sample into all chambers.

The dimensions utilized for the first design are shown in the 2nd column of **Table 4.2** and these were designed so that the wells would have sufficient surface area and volume to be adapted to the existing imaging protocols outlined in **Section 3.2.4** without significant

disruptions in protocol or surface density when imaged and be comparable to the pipette tip wells which had a surface area of 21.65 mm^2 and a volume capacity of ~256 μL. The outer wall and the inner divider were made relatively thin as they were above the 3D printer resolution of 0.1 mm and were sufficient to provide separation of the well chambers. This initial design was problematic, however, because it demonstrated leakage upon gluing and suffered from a brittle construction due to the thin walls and inconsistent print quality despite being above the advertised resolution.

This design was thus modified to have the dimensions in the 3rd column of **Table 4.2** with the biggest difference being thicker walls to reduce printing inconsistencies and to create a sturdier, more robust well. This change in the thickness resolved the printing inconsistency problem and resulted in well-constructed, sturdy wells. Additionally, a PanaVise base and attachment as outlined in **Section 4.2.4** and depicted in **Figure 4.9B** was introduced as part of the preparation procedure because imposing pressure on the top of the well while gluing would allow it to be completely pressed onto the coverslip and leave no openings for leaking. This redesign, however, still proved ineffective for 2 different reasons. The first was that although no leakage to the outside occurred, there was still leaking laterally within the chambers, but only in 1 direction. The second was that the PanaVise system necessitated a taller well design not as well suited for smaller sample volumes because gluing with a short height was unreasonably difficult and error-prone due to poor accessibility of the area around the well when short. Upon closer examination, this problem occurs because the design created in CAD Fusion Autodesk has a slight difference in height between the 2 dividers, which would permit transfer of sample between lateral wells and explains the leaking behavior observed. Additionally, 3D printing is

known to have surface inconsistencies which can create additional complications with leaking as this technique requires an absolute seal to avoid contamination[114].

Given these limitations, one possible method may be to use acetone vapor baths which are commonly used for the smoothening of plastic surfaces and have been previously used for the same purpose on 3D-printed parts[114]. However, a design incorporating microfluidics and automation of separation of biosensors may prove a more effective and consistent procedure given additional development time despite its complexity as they have been frequently utilized in such a way and would offer the additional benefit of removing a need for precise movements when imaging if designed to spot consistently in certain areas of the coverslip[115]. While further development of multi-target detection and clinical samples is necessary, I anticipate that iSiMREPS can be a viable detection tool for miRNAs as it possesses the needed sensitivity for miRNAs and its near-perfect specificity, rapid analysis speed, simple preparation, and lack of drawbacks limiting techniques for shorter sequences such as amplification bias in PCR or a need for extension for NGS would allow it to be an assay well suited for miRNA targets of interest.

Chapter 5. Summary & Outlook

5.1 Summary of Dissertation

Through an ageing population and better detection, cancer has risen to become a prominent disease with enormous health and financial burdens and a great deal of complexity and variation. The prevalence of cancer and the improvement of prognosis the earlier it is detected has created a need for diagnostic tools, especially early stage diagnostics. An effective diagnostic requires a biomarker that can reliably provide a diagnosis or characterization of the cancer being detected. Biomarkers come in many different shapes and forms including proteins, DNA, RNAs, and cells and they are capable of offering both diagnostic and prognostic information for the cancer they are biomarkers for[17, 18]. Cell-free nucleic acids in particular have garnered significant attention recently due to their ability to be part of liquid biopsy assays[26, 27] where detection can be done from collection and analysis of body fluids like blood without a need for invasive, sometimes contraindicated tissue biopsies. ctDNAs and miRNAs have been especially notable among these cfNAs since they show notable differences in expression but healthy and cancer patients and miRNAs have a high level of stability in biofluids thanks to protein complexes[37, 45, 116].

Technologies that have risen to meet detection needs for cfNAs, which typically possess a low abundance at femtomolar level for miRNAs and even lower for ctDNAs, focus primarily on amplification, hybridization of sequencing methods to identify their targets. Amplification techniques rely primarily on PCR to increase concentration of targets to detectable levels and are

an established gold standard with the ability to detect point mutations below 1%; ddPCR in particular, is sensitive enough to attain low copy number sensitivity[49, 117]. PCR-based techniques do, however, suffer from amplification bias that can give false negatives for low abundance targets and false positives from replication errors and primer mismatches, the latter of which is especially problematic for miRNAs[51]. Hybridization-based techniques achieve detection by base pairing the target nucleic acid to a probe with one being fluorescently labeled[52-54]. While they are simple, easy to prepare and work well on high-concentration targets, they suffer from hard limits on specificity due to the nature of binding thermodynamics[55]. Lastly, NGS, the new gold standard for sequencing-based techniques, is very effective for large scale genomic analysis and high throughput analysis, but has the weaknesses of amplification techniques, several complex preparation steps with their own errors, a need for complex bioinformatics analysis, and challenges for shorter sequences due to requiring adapter extension for usability[57-60]. SiMREPS addresses many of these weaknesses through a kinetics-based approach that identifies the target based on binding-dissociation behavior of a fluorescent probe and the signal pattern generated from the changing presence and absence of the probe at the surface[64]. This setup simplifies sample preparation, obviates any need for amplification, and achieves near-perfect specificity because kinetic behavior becomes increasingly differentiated from background as imaging time is extended[64]. It does, however, possess an inherent weakness in analysis speed as probe concentration must be increased to reduce time gaps where no probe is bound to target and this cannot be readily increased without a reduction in signal-to-noise. This places a hard limit on speed and necessitates a fundamental redesign as the speed limitations are inherent to SiMREPS' design.

Chapter 2 introduced iSiMREPS, which combines the kinetics-based detection of SiMREPS with a biosensor design that would capture the target and switch conformations to generate the same type of signal pattern as SiMREPS. This redesign overcame the speed limitations of SiMREPS because it allowed both states to be directly controlled and created an environment of high local concentration of probes that eliminated the time gaps between diffusing probes in SiMREPS. In this chapter, basic design requirements for iSiMREPS biosensors were established and they included a need for LNA modification in the CP to ensure strong capture, a competitor sequence on the anchor strand to ensure transitions between states actually occur, and a longer QS length to permit sufficient flexibility and access to both states to allow for generation of an effective fingerprint. Additionally, several different designs that varied the competitor length and the QS length were tested to determine which was the most effective for further development and standardization and the $Q_8C_6QS_{18}$ biosensor showed the best performance as it had the shortest dwell times while maintaining parity between low- and high-FRET states, enabling fast generation of a distinct fingerprint. Finally, rapid target detection through the use of formamide was demonstrated as an effective way to achieve rapid target detection with state dwell times below 1s for 10% formamide by reducing the duplex stability of the QP-target and QP-competitor interactions thus allowing faster transitions between states and quicker fingerprint generation. This chapter demonstrated the capacity of iSiMREPS for rapid nucleic acid detection.

Chapter 3 developed iSiMREPS into a full-fledged liquid biopsy assay. This began with the transition from a P-TIRF slide sandwich cell apparatus using bBSA for surface capture to an O-TIRF cut tip apparatus using Biotin-PEG. This change allowed for improvement in sensitivity as the cut tip apparatus had a taller height and smaller surface area allowing for greater

concentration of biosensors and target molecules within a given FOV. It also improved experiment reproducibility as PEG was less prone to forming aggregates. The iSiMREPS design established for miR-141 in Chapter 2 was then adapted for detection of *EGFR*Δ_{exon_19} with some minor modifications such as the use of auxiliary probe to account for the longer strand length and modifications to the sequence to fit *EGFR*Δ_{exon_19}. The sensitivity was further improved and the counts improved 3-4fold through the use of a TMSD strategy that improved S/N by removing the QP and CP to reduce noise and unwanted signal bleedthrough from sensors without a target that were near to one with it. Formamide concentration variations were also tested to determine which was most effective at accelerating the fingerprint generation without compromising sensor integrity or sensitivity. 10% v/v formamide was demonstrated to be capable of generated a useful fingerprint within only 10 seconds of imaging. With these optimizations in place, iSiMREPS was capable of achieving detection for both miR-141 and *EGFR*Δ_{exon_19} within only 30 seconds of imaging time total and with a LOD of ~3fM, which is more than sufficient for miRNAs[45].

With assay development completed, Chapter 4 shifted the focus to multi-target detection since iSiMREPS would require effectiveness against a broad range of targets to be a useful assay. This would create a need for clear, well defined design considerations and guidelines to adapt to any target of interest as well as a multi-target design as a panel of multiple biomarkers would be a more feasible clinical strategy and a desirable feature for iSiMREPS. From extensive testing, tweaking and optimization of biosensors for 3 different miRNAs in the miR-17/92 cluster, key design considerations and guidelines became much more apparent. For the CP, the CP-target T_m was not entirely predictive of binding strength and it was important to have at least 4 LNA modifications for sufficiently strong binding. Additionally, modeling to account for potential

secondary structure and self-binding was necessary to avoid complications with capture and LNA placement needed to consider these factors as LNA-modified residues can significantly contribute to such complications. For the QP and competitor, the number of GC residues in additional to length in the CP binding region is critical for obtaining a biosensor with desirable kinetic behaviors as high-GC QP sequences have longer dwell times which can impede fingerprint generation. 3 GC pairs is suggested for 8 nt CP-target sequences and 4 GC pairs for 7 nt CP-target sequences. Additionally, the sequence placement of the CP-target and QP-target interactions is important to ensure proper FRET signal generation and optimize both the QP-target length and GC content as well as the CP-target capture strength. Lastly, the complementarity of the sequence around the competitor must also be accounted for to avoid unwanted complementarity outside the competitor region artificially lengthening dwell times for the low-FRET state. All of these factors needed to be addressed to successfully develop working designs for miR-17 and miR-19a. However, miR-18a proved difficult to design effectively and showed that these guidelines have limitations and iSiMREPS would benefit from more sophisticated modeling that better estimates the interactions within the biosensor and allows for more deliberate, calculated design choices. Additionally, while the 3D-printed well setup for detecting multiple targets in a single run of imaging is promising and useful for demonstrating multi-target detection, there is insufficient printing resolution and consistency to allow for the well compartments to be properly sealed from leakage as well as ample room for human error in preparation and microscope handling to produce inconsistent results. A more sophisticated, consistent design that can readily reproduce results is thus a desirable future direction.

iSiMREPS overall looks well suited as a liquid biopsy tool for miRNAs. Due to the complexity and variance that cancer presents, liquid biopsies have also taken many different

shapes and forms and many different assays with a focus on different cancers and targets have been studied and developed[28, 118]. While iSiMREPS currently lacks the sensitivity needed for ctDNA targets due to their extremely low copy numbers[46, 47] and need for even greater sensitivity, it possesses ample sensitivity for miRNAs, which are a growing area of interest as liquid biopsy targets. Additionally, iSiMREPS offers advantages for miRNA detection as it retains the near-perfect specificity of the original SiMREPS, offers much faster detection and simplified preparation compared to the complexity of NGS or the longer, half hour run times of PCR, the preparation of both techniques, and does not have an inherent weakness for shorter sequences like NGS or PCR[51, 61-64, 117]. While it requires further development for multi-target detection so that it can be utilized in panels and additional testing on clinical samples to solidify its clinical utility, it has the potential to join the toolkit of liquid biopsy assays used by clinicians and researchers as a highly specific, simple, and rapid assay for miRNAs.

5.2 Outlook & Future Directions

There is ample room for iSiMREPS to be developed further beyond the original proof-of-concept demonstrated in Chapters 2 and 3 along the lines of multi-target detection and clinical utility that was explored in Chapter 4. Chapter 3 established that iSiMREPS could be applied more generally to multiple targets as a successful proof-of-concept was shown for miR-141 and *EGFR*Δ_{exon_19} and this was further confirmed with successful designs for miR-17 and miR-19a in Chapter 4. However, it was clearly apparent from the results in chapter 4 that the extent of target capture and by extension, sensitivity for the target, is not consistent between different biosensors even when they are designed with the same template. Additionally, while basic modeling and T_m values provide useful information and necessary guidelines for effective design, they are not always predictive of actual behavior and have difficulty accounting for all possible interactions

within the biosensor as seen by miR-18a's biosensor being unable to capture properly and generate FRET signal and the original miR-19a design having weak capture in spite of a predicted CP-target T_m of 64°C.

Thus, a more in-depth and sophisticated modeling system that can more thoroughly take into account the various interactions within the biosensor as well as with the surrounding environment would be a welcome addition as it would allow for more deliberate, carefully chosen biosensor design and allow for much clearer, well-defined criteria for adapting iSiMREPS to any target of interest. One potential avenue for this is building a new model that focuses on the capture of the target at the surface using a contact-focused model similar to the coarse-grained Monte-Carlo simulation utilized in **Section 3.3.2** which utilized contact between strands as a means of estimating distribution between low- and high-FRET states and the QS length was varied. Coarse-grained models have been previously utilized for assisting with problems related to both DNA and RNA structure as well as for research focused on creating and developing DNA or RNA nanotechnology[119-121]. These models can expand on the nearest neighbor model frequently used to calculate T_m by incorporating factors such as base-pairing, stacking interactions, contact, coaxial interactions, and buffer conditions such as the concentration of salt used[119-121]. Additionally, this type of model is suitable for iSiMREPS biosensors as coarse-grained models are currently optimized for use with shorter strands typically less than 100 nt long which is consistent with a wide range of targets that iSiMREPS would be used for and with the strands that compose iSiMREPS biosensors. This model could be developed concurrently with experiments on a variety of different targets and sensor configurations in order to provide a more consistent, quantifiable, and predictive measure of design parameters for target capture such as capture efficiency, LNA modification and

placement, and secondary structure and how well they translate into effective performance for target detection. If successful, this model could be packaged as an additional part of software already used for iSiMREPS such as the trace analysis and filtering software in order to assist with the design process and allow its user to modify iSiMREPS for any target of interest. An automation of this process using machine learning optimization developed with real data sets similar to the trace parameter optimizer would also be helpful to improve the efficiency of iSiMREPS detection development and evaluate viability of designs. This software expansion and optimization of behavior using machine learning with real data could also be taken a step further where optimization recommendations could also be given for all other iSiMREPS parameters including the query-target length, placement, and the competitor. Since these parameters follow a more predictable pattern as shown in **Section 2.3** and the Monte-Carlo modeling for the QS in **Section 3.3.2**, developing an optimization algorithm similar to the trace optimizer would be within reach and would be helpful in simplifying biosensor design for new targets and allowing the technique to be more easily adopted by new users.

In addition to modeling for improving design, further expansion of iSiMREPS to clinical samples beyond the initial proof-of-concept and a completion of multi-target detection started in Chapter 4 would also be desirable directions for iSiMREPS. Since one long term use of iSiMREPS would be for panel detection of nucleic acids for patient diagnostics, extending the testing of iSiMREPS to actual clinical samples or conditions like was demonstrated for classic SiMREPS for let-7a and let-7c[64] would be necessary. The choice of the miR-17/92 cluster in Chapter 4 was in part because of this clusters strong connection to cancer pathways and it showing promising diagnostic value for B-Cell lymphoma and potentially for colorectal cancer[112]. This cluster, as mentioned in Chapter 4, was also desirable to test iSiMREPS ability to

work on many different targets and even SNVs. Demonstrating detection of members of this cluster from a B-cell lymphoma patients sample would thus provide a strong proof-of-concept for iSiMREPS' utility as a diagnostic tool directly on clinical samples. Completion of this proof-of-concept would open the door to testing on other types of samples and targets of interest such as urinary miRNAs for bladder cancer[122]. Additionally, the rapid detection achieved by iSiMREPS can translate into other benefits for clinical use. In addition to high throughput when sample volumes are large, the number of FOVs recorded from a sample can be greatly expanded to allow for potential improvements of LOD from finding additional targets in the extra FOVs or analysis of multiple targets that are spatially separated in a single run of the assay by shifting to FOVs containing biosensors for different targets.

iSiMREPS also has room to grow in both scope for nucleic acids and beyond as well as sensitivity. Single molecule technology similar to iSiMREPS developed by the Walter group has previously been shown to be able to evaluate nucleic acids with secondary structures that can undergo conformational changes[123]. Thus, detection of nucleic acid targets that could undergo such changes would be another potential application of iSiMREPS provided FRET pairing is possible and a region where the QP shows different behavior from differences such as structure alterations or sequence availability. iSiMREPS will also be a suitable technique for other biomarkers where FRET pairing is possible and especially for those that cannot be amplified. One such target for further development would be proteins where amplification cannot be done and being able to detect directly from sample rapidly and with high sensitivity would be very beneficial. There is precedent for using kinetic fingerprinting for this purpose as SiMREPS has been demonstrated for protein detection previously and was able to achieve a much better LOD over ELISA-based techniques[124]. Given this successful demonstration, it is conceivable that

iSiMREPS could be similarly adapted for protein detection using a primary and secondary antibody labeled with fluorophores that are capable of FRET pairing similarly to how SiMREPS utilized a capture antibody and a fluorescently labeled antigen-binding fragment. Pursuing this direction will require deliberate consideration of antibodies or fragments as the size variance of proteins and the position the antibodies bind to will dictate the FRET efficiency and subsequently, the observed signal. Furthermore, the sensitivity also has room for further improvement if combined with pre-concentration techniques were the area covered by target molecules is further reduced. One way this might be accomplished is utilizing an Aqueous Two Phase System (ATPS) which has used previously for the concentration of biomolecules[125]. Since the biopolymer, typically PEG, and the salt concentration of these systems is primarily what separates biomolecules[125], this could readily be adapted to an iSiMREPS workflow as nucleic acids are negatively charged and would be amenable to this type of concentration. Implementing this would require careful consideration of the ATPS makeup and an evaluation on what effects it has on the sample and if those effects translate to differences in detection and quantification. Completion of these future directions would greatly improve the range of targets iSiMREPS can be used for.

There is also the possibility of further improvements to the assay and design to enhance its capabilities. One design change would be to run the assay at slightly above room temperature to ensure minimal temperature fluctuations. This would grant the data better reproducibility and shrink some of the larger error bars observed in **Figures 3.14B and 3.14D**, which were the result of the data collection being spread out over a longer time period and the temperature of the room varying from 19-23°C. Performing the imaging at a temperature of around 27-30°C consistently would potentially obviate the need for formamide as the additional temperature would achieve a

similar effect. We can observe this in **Figure 4.3D** where the experiment was done at a temperature of 28°C without formamide and the trace transitions very rapidly. Another design enhancement could be further improving analysis speed by lowering the camera exposure time below the 60 ms used for miR-141 in Chapter 3 and utilizing the higher formamide percentages. Given the generally high intensity of traces relative to background for iSiMREPS as seen in **Figures 3.9C-D** and even with high formamide percentages as seen in **Figure 3.12A**, it should be possible to lower the exposure time while retaining sufficient intensity to distinguish the signal from background. This would allow for lifetimes shorter than the 60 ms exposure to be more readily picked up and may allow higher formamide percentage traces to be more easily distinguished from background due to the traces looking cleaner and better distinguished as shorter transitions can now be more accurately observed. Given that the lifetimes at 15% formamide for miR-141 are already <0.2 s and can go even lower at 20% (**Figure 3.11C**), detection in 3-4 seconds could realistically be achieved. Lastly, another modification that can be used to modulate the biosensor behavior is to introduce mismatches within key sequences in place of length alterations. Since sufficiently long sequences can maintain duplex formation even with mismatches but see decreases in T_m from it[126], mismatches within the sequence to tune kinetic behavior can be utilized. They are well suited for situations where changes in sequence length or placement may be difficult to implement like they were for the miR-18a biosensor in **Section 4.3.3** or where utilizing them can remove unwanted interactions like the capture spacer toehold interaction with the fully complementary invaders in **Section 3.3.4**.

Lastly, creating a well-tested, substantive multi-target setup for iSiMREPS would be another future direction since multiple biomarkers can be helpful to either improve the reliability of detection where single biomarkers can be insufficient for diagnostic accuracy or to obtain a

greater breadth of information about the patients' disease state or condition[110, 111]. Multiple biomarkers can be especially helpful for miRNAs and cancer since cancers have layered, complex characterization and the regulation of miRNAs is very intricate, complex, and tied to many different processes with expression levels and regulation also varying for individual miRNAs and different people[127, 128]. Given this complexity and variation, profiles of multiple miRNAs can be more informative than a single one[128]. Other methods of spatially separating sample may be worth pursuing as a future direction in lieu of the 3D-printed well design in **Section 4.3.6** given the issues observed for it. One approach for example may be a modified sample introduction setup that utilizes microfluidics as a way of introducing a single sample to multiple areas while separating and segmenting different sensor components on the slide over coverslip used for microscope imaging[115]. While this setup is potentially more complex and would require longer development times, it would allow for some degree of automation and reproducibility in sample preparation as well as simple, consistent segmentation of different biosensors to the imaging surface. Another potential approach may be utilizing phase separated cells or compartments where different biosensors can be segmented into individual cells and imaged simultaneously as well as analyzed by spatial segment for the number of counts for each target within each segment[129]. While this approach may require a more deliberate, thorough and involved design for multi-target detection, it also has the potential to be better adapted for iSiMREPS as simple, color-based multiplexing would be limited by a need for different FRET pairs and hampered by potential overlap in emissions between different fluorophores[130].

Overall, while this dissertation has demonstrated iSiMREPS and what it is capable of, there is still room for further growth and development and only a fraction of the potential of the technique has been tapped into. I anticipate iSiMREPS becoming part of the liquid biopsy assay

toolkit as a fast, highly specific tool well suited for miRNA panels. This thesis demonstrates building an assay from the ground up and will be a worthwhile experience for creating new techniques for other scientific problems in my future work.

References

1. Siegel, R. L.; Miller, K. D.; Fuchs, H. E.; Jemal, A., Cancer Statistics, 2021. *CA: A Cancer Journal for Clinicians* **2021,** *71* (1), 7-33.
2. ACS. Economic Impact of Cancer 2018. https://www.cancer.org/treatment/finding-and-paying-for-treatment/managing-costs/economic-impact-of-cancer.html.
3. Block, K. I.; Gyllenhaal, C.; Lowe, L.; Amedei, A.; Amin, A. R. M. R.; Amin, A.; Aquilano, K.; Arbiser, J.; Arreola, A.; Arzumanyan, A.; Ashraf, S. S.; Azmi, A. S.; Benencia, F.; Bhakta, D.; Bilsland, A.; Bishayee, A.; Blain, S. W.; Block, P. B.; Boosani, C. S.; Carey, T. E.; Carnero, A.; Carotenuto, M.; Casey, S. C.; Chakrabarti, M.; Chaturvedi, R.; Chen, G. Z.; Chen, H.; Chen, S.; Chen, Y. C.; Choi, B. K.; Ciriolo, M. R.; Coley, H. M.; Collins, A. R.; Connell, M.; Crawford, S.; Curran, C. S.; Dabrosin, C.; Damia, G.; Dasgupta, S.; DeBerardinis, R. J.; Decker, W. K.; Dhawan, P.; Diehl, A. M. E.; Dong, J.-T.; Dou, Q. P.; Drew, J. E.; Elkord, E.; El-Rayes, B.; Feitelson, M. A.; Felsher, D. W.; Ferguson, L. R.; Fimognari, C.; Firestone, G. L.; Frezza, C.; Fujii, H.; Fuster, M. M.; Generali, D.; Georgakilas, A. G.; Gieseler, F.; Gilbertson, M.; Green, M. F.; Grue, B.; Guha, G.; Halicka, D.; Helferich, W. G.; Heneberg, P.; Hentosh, P.; Hirschey, M. D.; Hofseth, L. J.; Holcombe, R. F.; Honoki, K.; Hsu, H.-Y.; Huang, G. S.; Jensen, L. D.; Jiang, W. G.; Jones, L. W.; Karpowicz, P. A.; Keith, W. N.; Kerkar, S. P.; Khan, G. N.; Khatami, M.; Ko, Y. H.; Kucuk, O.; Kulathinal, R. J.; Kumar, N. B.; Kwon, B. S.; Le, A.; Lea, M. A.; Lee, H.-Y.; Lichtor, T.; Lin, L.-T.; Locasale, J. W.; Lokeshwar, B. L.; Longo, V. D.; Lyssiotis, C. A.; MacKenzie, K. L.; Malhotra, M.; Marino, M.; Martinez-Chantar, M. L.; Matheu, A.; Maxwell, C.; McDonnell, E.; Meeker, A. K.; Mehrmohamadi, M.; Mehta, K.; Michelotti, G. A.; Mohammad, R. M.; Mohammed, S. I.; Morre, D. J.; Muralidhar, V.; Muqbil, I.; Murphy, M. P.; Nagaraju, G. P.; Nahta, R.; Niccolai, E.; Nowsheen, S.; Panis, C.; Pantano, F.; Parslow, V. R.; Pawelec, G.; Pedersen, P. L.; Poore, B.; Poudyal, D.; Prakash, S.; Prince, M.; Raffaghello, L.; Rathmell, J. C.; Rathmell, W. K.; Ray, S. K.; Reichrath, J.; Rezazadeh, S.; Ribatti, D.; Ricciardiello, L.; Robey, R. B.; Rodier, F.; Rupasinghe, H. P. V.; Russo, G. L.; Ryan, E. P.; Samadi, A. K.; Sanchez-Garcia, I.; Sanders, A. J.; Santini, D.; Sarkar, M.; Sasada, T.; Saxena, N. K.; Shackelford, R. E.; Shantha Kumara, H. M. C.; Sharma, D.; Shin, D. M.; Sidransky, D.; Siegelin, M. D.; Signori, E.; Singh, N.; Sivanand, S.; Sliva, D.; Smythe, C.; Spagnuolo, C.; Stafforini, D. M.; Stagg, J.; Subbarayan, P. R.; Sundin, T.; Talib, W. H.; Thompson, S. K.; Tran, P. T.; Ungefroren, H.; Vander Heiden, M. G.; Venkateswaran, V.; Vinay, D. S.; Vlachostergios, P. J.; Wang, Z.; Wellen, K. E.; Whelan, R. L.; Yang, E. S.; Yang, H.; Yang, X.; Yaswen, P.; Yedjou, C.; Yin, X.; Zhu, J.; Zollo, M., Designing a broad-spectrum integrative approach for cancer prevention and treatment. *Seminars in Cancer Biology* **2015,** *35*, S276-S304.

4. Rybinski, B.; Yun, K., Addressing intra-tumoral heterogeneity and therapy resistance. *Oncotarget* **2016,** *7* (44), 72322-72342.
5. Block, K. I.; Block, P. B.; Gyllenhaal, C., Integrative Therapies in Cancer:Modulating a Broad Spectrum of Targets for Cancer Management. *Integrative Cancer Therapies* **2015,** *14* (2), 113-118.
6. El-Deiry, W. S.; Goldberg, R. M.; Lenz, H.-J.; Shields, A. F.; Gibney, G. T.; Tan, A. R.; Brown, J.; Eisenberg, B.; Heath, E. I.; Phuphanich, S.; Kim, E.; Brenner, A. J.; Marshall, J. L., The current state of molecular testing in the treatment of patients with solid tumors, 2019. *CA: a cancer journal for clinicians* **2019,** *69* (4), 305-343.
7. Naito, Y.; Aburatani, H.; Amano, T.; Baba, E.; Furukawa, T.; Hayashida, T.; Hiyama, E.; Ikeda, S.; Kanai, M.; Kato, M.; Kinoshita, I.; Kiyota, N.; Kohno, T.; Kohsaka, S.; Komine, K.; Matsumura, I.; Miura, Y.; Nakamura, Y.; Natsume, A.; Nishio, K.; Oda, K.; Oda, N.; Okita, N.; Oseto, K.; Sunami, K.; Takahashi, H.; Takeda, M.; Tashiro, S.; Toyooka, S.; Ueno, H.; Yachida, S.; Yoshino, T.; Tsuchihara, K.; Japanese Society of Medical, O.; Japan Society of Clinical, O.; Japanese Cancer, A., Clinical practice guidance for next-generation sequencing in cancer diagnosis and treatment (edition 2.1). *Int J Clin Oncol* **2021,** *26* (2), 233-283.
8. Brierley, J.; O'Sullivan, B.; Asamura, H.; Byrd, D.; Huang, S. H.; Lee, A.; Piñeros, M.; Mason, M.; Moraes, F. Y.; Rösler, W.; Rous, B.; Torode, J.; van Krieken, J. H.; Gospodarowicz, M., Global Consultation on Cancer Staging: promoting consistent understanding and use. *Nature Reviews Clinical Oncology* **2019,** *16* (12), 763-771.
9. ACS. Survival Rates for Pancreatic Cancer 2021. https://www.cancer.org/cancer/pancreatic-cancer/detection-diagnosis-staging/survival-rates.html.
10. ACS. Survival Rates for Colorectal Cancer 2021. https://www.cancer.org/cancer/colon-rectal-cancer/detection-diagnosis-staging/survival-rates.html.
11. Kamisawa, T.; Wood, L. D.; Itoi, T.; Takaori, K., Pancreatic cancer. *Lancet* **2016,** *388* (10039), 73-85.
12. Dama, E.; Colangelo, T.; Fina, E.; Cremonesi, M.; Kallikourdis, M.; Veronesi, G.; Bianchi, F., Biomarkers and Lung Cancer Early Detection: State of the Art. *Cancers* **2021,** *13* (15), 3919.
13. Herceg, Z.; Hainaut, P., Genetic and epigenetic alterations as biomarkers for cancer detection, diagnosis and prognosis. *Molecular Oncology* **2007,** *1* (1), 26-41.
14. Abbas, M.; Faggian, A.; Sintali, D. N.; Khan, G. J.; Naeem, S.; Shi, M.; Dingding, C., Current and future biomarkers in gastric cancer. *Biomedicine & Pharmacotherapy* **2018,** *103*, 1688-1700.
15. De Roock, W.; Biesmans, B.; De Schutter, J.; Tejpar, S., Clinical Biomarkers in Oncology. *Molecular Diagnosis & Therapy* **2009,** *13* (2), 103-114.
16. Beale, G.; Chattopadhyay, D.; Gray, J.; Stewart, S.; Hudson, M.; Day, C.; Trerotoli, P.; Giannelli, G.; Manas, D.; Reeves, H., AFP, PIVKAII, GP3, SCCA-1 and follisatin as surveillance biomarkers for hepatocellular cancer in non-alcoholic and alcoholic fatty liver disease. *BMC Cancer* **2008,** *8* (1), 200.
17. Tosoian, J.; Loeb, S., PSA and Beyond: The Past, Present, and Future of Investigative Biomarkers for Prostate Cancer. *TheScientificWorldJOURNAL* **2010,** *10*, 637648.

18. Slamon, D. J.; Clark, G. M.; Wong, S. G.; Levin, W. J.; Ullrich, A.; McGuire, W. L., Human Breast Cancer: Correlation of Relapse and Survival with Amplification of the HER-2/neu Oncogene. *Science* **1987,** *235* (4785), 177-182.
19. Naz, Z.; Usman, S.; Saleem, K.; Ahmed, S.; Bashir, H.; Bilal, M.; Sumrin, A., Alpha-fetoprotein: A fabulous biomarker in hepatocellular, gastric and rectal cancer diagnosis. *Biomedical Research* **2018,** *29*.
20. Wu, W.; Gao, H.; Li, X.; Peng, S.; Yu, J.; Liu, N.; Zhan, G.; Zhu, Y.; Wang, K.; Guo, X., β-hCG promotes epithelial ovarian cancer metastasis through ERK/MMP2 signaling pathway. *Cell Cycle* **2019,** *18* (1), 46-59.
21. Zhu, W.-Y.; Li, H.-F.; Fang, K.-X.; Zhang, B.-J.; Zhou, S.-Q.; Zhang, Y.-K.; Le, H.-B.; Hu, X.-F., Epidermal Growth Factor Receptor Mutations and Their Prognostic Value with Carcinoembryonic Antigen in Pathological T1 Lung Adenocarcinoma. *Disease Markers* **2018,** *2018*, 2942618.
22. Chang, S.; Park, H. K.; Choi, Y.-L.; Jang, S. J., Interobserver Reproducibility of PD-L1 Biomarker in Non-small Cell Lung Cancer: A Multi-Institutional Study by 27 Pathologists. *J Pathol Transl Med* **2019,** *53* (6), 347-353.
23. Wong, H.-L.; Pfeiffer, R. M.; Fears, T. R.; Vermeulen, R.; Ji, S.; Rabkin, C. S., Reproducibility and Correlations of Multiplex Cytokine Levels in Asymptomatic Persons. *Cancer Epidemiology Biomarkers & Prevention* **2008,** *17* (12), 3450.
24. Anfossi, S.; Babayan, A.; Pantel, K.; Calin, G. A., Clinical utility of circulating non-coding RNAs — an update. *Nature Reviews Clinical Oncology* **2018,** *15* (9), 541-563.
25. Schwarzenbach, H.; Hoon, D. S. B.; Pantel, K., Cell-free nucleic acids as biomarkers in cancer patients. *Nature Reviews Cancer* **2011,** *11* (6), 426-437.
26. Crowley, E.; Di Nicolantonio, F.; Loupakis, F.; Bardelli, A., Liquid biopsy: monitoring cancer-genetics in the blood. *Nature Reviews Clinical Oncology* **2013,** *10* (8), 472-484.
27. Heitzer, E.; Ulz, P.; Geigl, J. B., Circulating Tumor DNA as a Liquid Biopsy for Cancer. *Clinical Chemistry* **2015,** *61* (1), 112-123.
28. Rodríguez, J.; Avila, J.; Rolfo, C.; Ruíz-Patiño, A.; Russo, A.; Ricaurte, L.; Ordóñez-Reyes, C.; Arrieta, O.; Zatarain-Barrón, Z. L.; Recondo, G.; Cardona, A. F., When Tissue is an Issue the Liquid Biopsy is Nonissue: A Review. *Oncology and Therapy* **2021,** *9* (1), 89-110.
29. Goldman, J. W.; Noor, Z. S.; Remon, J.; Besse, B.; Rosenfeld, N., Are liquid biopsies a surrogate for tissue EGFR testing? *Annals of Oncology* **2018,** *29*, i38-i46.
30. Krol, J.; Loedige, I.; Filipowicz, W., The widespread regulation of microRNA biogenesis, function and decay. *Nature Reviews Genetics* **2010,** *11* (9), 597-610.
31. van Kouwenhove, M.; Kedde, M.; Agami, R., MicroRNA regulation by RNA-binding proteins and its implications for cancer. *Nature Reviews Cancer* **2011,** *11* (9), 644-656.
32. Kozomara, A.; Griffiths-Jones, S., miRBase: integrating microRNA annotation and deep-sequencing data. *Nucleic Acids Res* **2011,** *39* (Database issue), D152-D157.
33. Olive, V.; Jiang, I.; He, L., mir-17-92, a cluster of miRNAs in the midst of the cancer network. *The International Journal of Biochemistry & Cell Biology* **2010,** *42* (8), 1348-1354.
34. Olive, V.; Li, Q.; He, L., mir-17-92: a polycistronic oncomir with pleiotropic functions. *Immunological Reviews* **2013,** *253* (1), 158-166.

35. Condrat, C. E.; Thompson, D. C.; Barbu, M. G.; Bugnar, O. L.; Boboc, A.; Cretoiu, D.; Suciu, N.; Cretoiu, S. M.; Voinea, S. C., miRNAs as Biomarkers in Disease: Latest Findings Regarding Their Role in Diagnosis and Prognosis. *Cells* **2020,** *9* (2), 276.
36. Lan, H.; Lu, H.; Wang, X.; Jin, H., MicroRNAs as Potential Biomarkers in Cancer: Opportunities and Challenges. *BioMed Research International* **2015,** *2015*, 125094.
37. Ortiz-Quintero, B., Cell-free microRNAs in blood and other body fluids, as cancer biomarkers. *Cell Proliferation* **2016,** *49* (3), 281-303.
38. Bautista-Sánchez, D.; Arriaga-Canon, C.; Pedroza-Torres, A.; De La Rosa-Velázquez, I. A.; González-Barrios, R.; Contreras-Espinosa, L.; Montiel-Manríquez, R.; Castro-Hernández, C.; Fragoso-Ontiveros, V.; Álvarez-Gómez, R. M.; Herrera, L. A., The Promising Role of miR-21 as a Cancer Biomarker and Its Importance in RNA-Based Therapeutics. *Molecular Therapy - Nucleic Acids* **2020,** *20*, 409-420.
39. Zhao, W.; Zhao, J.-J.; Zhang, L.; Xu, Q.-F.; Zhao, Y.-M.; Shi, X.-Y.; Xu, A.-G., Serum miR-21 level: a potential diagnostic and prognostic biomarker for non-small cell lung cancer. *Int J Clin Exp Med* **2015,** *8* (9), 14759-14763.
40. Bryant, R. J.; Pawlowski, T.; Catto, J. W. F.; Marsden, G.; Vessella, R. L.; Rhees, B.; Kuslich, C.; Visakorpi, T.; Hamdy, F. C., Changes in circulating microRNA levels associated with prostate cancer. *British Journal of Cancer* **2012,** *106* (4), 768-774.
41. Mitchell, P. S.; Parkin, R. K.; Kroh, E. M.; Fritz, B. R.; Wyman, S. K.; Pogosova-Agadjanyan, E. L.; Peterson, A.; Noteboom, J.; Briant, K. C.; Allen, A.; Lin, D. W.; Urban, N.; Drescher, C. W.; Knudsen, B. S.; Stirewalt, D. L.; Gentleman, R.; Vessella, R. L.; Nelson, P. S.; Martin, D. B.; Tewari, M., Circulating microRNAs as stable blood-based markers for cancer detection. *Proceedings of the National Academy of Sciences* **2008,** *105* (30), 10513.
42. Thierry, A. R.; El Messaoudi, S.; Gahan, P. B.; Anker, P.; Stroun, M., Origins, structures, and functions of circulating DNA in oncology. *Cancer Metastasis Rev* **2016,** *35* (3), 347-376.
43. Villaflor, V.; Won, B.; Nagy, R.; Banks, K.; Lanman, R. B.; Talasaz, A.; Salgia, R., Biopsy-free circulating tumor DNA assay identifies actionable mutations in lung cancer. *Oncotarget; Vol 7, No 41* **2016**.
44. Fan, G.; Zhang, K.; Ding, J.; Li, J., Prognostic value of EGFR and KRAS in circulating tumor DNA in patients with advanced non-small cell lung cancer: a systematic review and meta-analysis. *Oncotarget; Vol 8, No 20* **2017**.
45. Weber, J. A.; Baxter, D. H.; Zhang, S.; Huang, D. Y.; How Huang, K.; Jen Lee, M.; Galas, D. J.; Wang, K., The MicroRNA Spectrum in 12 Body Fluids. *Clinical Chemistry* **2010,** *56* (11), 1733-1741.
46. Diaz, L. A., Jr.; Bardelli, A., Liquid biopsies: genotyping circulating tumor DNA. *J Clin Oncol* **2014,** *32* (6), 579-586.
47. Wu, J.; Tang, W.; Huang, L.; Hou, N.; Wu, J.; Cheng, X.; Ma, D.; Qian, P.; Shen, Q.; Guo, W.; Peng, W.; Liu, Y.; Jiang, C.; Feng, J., The analysis of cell-free DNA concentrations and integrity in serum of initial and treated of lymphoma patients. *Clinical Biochemistry* **2019,** *63*, 59-65.
48. Milbury, C. A.; Zhong, Q.; Lin, J.; Williams, M.; Olson, J.; Link, D. R.; Hutchison, B., Determining lower limits of detection of digital PCR assays for cancer-related gene mutations. *Biomolecular Detection and Quantification* **2014,** *1* (1), 8-22.

49. Uchiyama, Y.; Nakashima, M.; Watanabe, S.; Miyajima, M.; Taguri, M.; Miyatake, S.; Miyake, N.; Saitsu, H.; Mishima, H.; Kinoshita, A.; Arai, H.; Yoshiura, K. i.; Matsumoto, N., Ultra–sensitive droplet digital PCR for detecting a low–prevalence somatic GNAQ mutation in Sturge–Weber syndrome. *Scientific Reports* **2016,** *6* (1), 22985.
50. Long, S.; Berkemeier, B., Maximizing viral detection with SIV droplet digital PCR (ddPCR) assays. *PLoS One* **2020,** *15* (5), e0233085-e0233085.
51. Potapov, V.; Ong, J., Examining Sources of Error in PCR by Single-Molecule Sequencing. *PLoS One* **2017,** *12*, e0169774.
52. Cohen, L.; Hartman, M. R.; Amardey-Wellington, A.; Walt, D. R., Digital direct detection of microRNAs using single molecule arrays. *Nucleic Acids Res* **2017,** *45* (14), e137-e137.
53. Li, Z.; Zhou, X.; Li, L.; Liu, S.; Wang, C.; Li, L.; Yu, C.; Su, X., Probing DNA Hybridization Equilibrium by Cationic Conjugated Polymer for Highly Selective Detection and Imaging of Single-Nucleotide Mutation. *Analytical Chemistry* **2018,** *90* (11), 6804-6810.
54. Wu, L. R.; Wang, J. S.; Fang, J. Z.; R Evans, E.; Pinto, A.; Pekker, I.; Boykin, R.; Ngouenet, C.; Webster, P. J.; Beechem, J.; Zhang, D. Y., Continuously tunable nucleic acid hybridization probes. *Nature Methods* **2015,** *12* (12), 1191-1196.
55. Zhang, D. Y.; Chen, S. X.; Yin, P., Optimizing the specificity of nucleic acid hybridization. *Nature Chemistry* **2012,** *4* (3), 208-214.
56. Chatterjee, T.; Li, Z.; Khanna, K.; Montoya, K.; Tewari, M.; Walter, N. G.; Johnson-Buck, A., Ultraspecific analyte detection by direct kinetic fingerprinting of single molecules. *TrAC Trends in Analytical Chemistry* **2020,** *123*, 115764.
57. McGinnis, J.; Laplante, J.; Shudt, M.; George, K. S., Next generation sequencing for whole genome analysis and surveillance of influenza A viruses. *Journal of Clinical Virology* **2016,** *79*, 44-50.
58. Morrison, J.; Koeman, J. M.; Johnson, B. K.; Foy, K. K.; Beddows, I.; Zhou, W.; Chesla, D. W.; Rossell, L. L.; Siegwald, E. J.; Adams, M.; Shen, H., Evaluation of whole-genome DNA methylation sequencing library preparation protocols. *Epigenetics & Chromatin* **2021,** *14* (1), 28.
59. Tenea, G. N.; Hurtado, P., Next-Generation Sequencing for Whole-Genome Characterization of Weissella cibaria UTNGt21O Strain Originated From Wild Solanum quitoense Lam. Fruits: An Atlas of Metabolites With Biotechnological Significance. *Front Microbiol* **2021,** *12*, 675002-675002.
60. Barberán-Soler, S.; Vo, J. M.; Hogans, R. E.; Dallas, A.; Johnston, B. H.; Kazakov, S. A., Decreasing miRNA sequencing bias using a single adapter and circularization approach. *Genome Biology* **2018,** *19* (1), 105.
61. Darvasi, O.; Szabo, P. M.; Nemeth, K.; Szabo, K.; Spisak, S.; Liko, I.; Czirjak, S.; Racz, K.; Igaz, P.; Patocs, A.; Butz, H., Limitations of high throughput methods for miRNA expression profiles in non-functioning pituitary adenomas. *Pathology & Oncology Research* **2019,** *25* (1), 169-182.
62. Siddika, T.; Heinemann, I. U., Bringing MicroRNAs to Light: Methods for MicroRNA Quantification and Visualization in Live Cells. *Frontiers in Bioengineering and Biotechnology* **2021,** *8* (1534).
63. Baker, M., MicroRNA profiling: separating signal from noise. *Nature Methods* **2010,** *7* (9), 687-692.

64. Johnson-Buck, A.; Su, X.; Giraldez, M. D.; Zhao, M.; Tewari, M.; Walter, N. G., Kinetic fingerprinting to identify and count single nucleic acids. *Nature Biotechnology* **2015,** *33* (7), 730-732.
65. Jungmann, R.; Avendaño, M. S.; Woehrstein, J. B.; Dai, M.; Shih, W. M.; Yin, P., Multiplexed 3D cellular super-resolution imaging with DNA-PAINT and Exchange-PAINT. *Nature Methods* **2014,** *11* (3), 313-318.
66. Hayward, S. L.; Lund, P. E.; Kang, Q.; Johnson-Buck, A.; Tewari, M.; Walter, N. G., Ultraspecific and Amplification-Free Quantification of Mutant DNA by Single-Molecule Kinetic Fingerprinting. *Journal of the American Chemical Society* **2018,** *140* (37), 11755-11762.
67. Mehrotra, P., Biosensors and their applications - A review. *J Oral Biol Craniofac Res* **2016,** *6* (2), 153-159.
68. Cammann, K., Bio-sensors based on ion-selective electrodes. *Fresenius' Zeitschrift für analytische Chemie* **1977,** *287* (1), 1-9.
69. Thévenot, D. R.; Toth, K.; Durst, R. A.; Wilson, G. S., Electrochemical biosensors: recommended definitions and classification1International Union of Pure and Applied Chemistry: Physical Chemistry Division, Commission I.7 (Biophysical Chemistry); Analytical Chemistry Division, Commission V.5 (Electroanalytical Chemistry).1. *Biosensors and Bioelectronics* **2001,** *16* (1), 121-131.
70. Mohamed, H. M., Sensors and Biosensors for Environment Contaminants. In *Nanosensor Technologies for Environmental Monitoring*, Inamuddin; Asiri, A. M., Eds. Springer International Publishing: Cham, 2020; pp 109-134.
71. Andryukov, B. G.; Besednova, N. N.; Romashko, R. V.; Zaporozhets, T. S.; Efimov, T. A., Label-Free Biosensors for Laboratory-Based Diagnostics of Infections: Current Achievements and New Trends. *Biosensors* **2020,** *10* (2), 11.
72. Ye, S.; Feng, S.; Huang, L.; Bian, S., Recent Progress in Wearable Biosensors: From Healthcare Monitoring to Sports Analytics. *Biosensors* **2020,** *10* (12), 205.
73. Ramirez-Valles, E. G.; Rodríguez-Pulido, A.; Barraza-Salas, M.; Martínez-Velis, I.; Meneses-Morales, I.; Ayala-García, V. M.; Alba-Fierro, C. A., A Quest for New Cancer Diagnosis, Prognosis and Prediction Biomarkers and Their Use in Biosensors Development. *Technology in Cancer Research & Treatment* **2020,** *19*, 1533033820957033.
74. Damborský, P.; Švitel, J.; Katrlík, J., Optical biosensors. *Essays Biochem* **2016,** *60* (1), 91-100.
75. Gootenberg, J. S.; Abudayyeh, O. O.; Lee, J. W.; Essletzbichler, P.; Dy, A. J.; Joung, J.; Verdine, V.; Donghia, N.; Daringer, N. M.; Freije, C. A.; Myhrvold, C.; Bhattacharyya, R. P.; Livny, J.; Regev, A.; Koonin, E. V.; Hung, D. T.; Sabeti, P. C.; Collins, J. J.; Zhang, F., Nucleic acid detection with CRISPR-Cas13a/C2c2. *Science* **2017,** *356* (6336), 438-442.
76. Chen, J. S.; Ma, E.; Harrington, L. B.; Costa, M. D.; Tian, X.; Palefsky, J. M.; Doudna, J. A., CRISPR-Cas12a target binding unleashes indiscriminate single-stranded DNase activity. *Science* **2018,** *360* (6387), 436-439.
77. Hochreiter, B.; Pardo-Garcia, A.; Schmid, J. A., Fluorescent Proteins as Genetically Encoded FRET Biosensors in Life Sciences. *Sensors* **2015,** *15* (10), 26281-26314.
78. Schaaf, T. M.; Li, A.; Grant, B. D.; Peterson, K.; Yuen, S.; Bawaskar, P.; Kleinboehl, E.; Li, J.; Thomas, D. D.; Gillispie, G. D., Red-Shifted FRET Biosensors for High-Throughput Fluorescence Lifetime Screening. *Biosensors* **2018,** *8* (4), 99.

79. Naresh, V.; Lee, N., A Review on Biosensors and Recent Development of Nanostructured Materials-Enabled Biosensors. *Sensors* **2021,** *21* (4), 1109.
80. Li, J.; Johnson-Buck, A.; Yang, Y.; Shih, W.; Yan, H.; Walter, N., Exploring the speed limit of toehold exchange with a cartwheeling DNA acrobat. *Nature Nanotechnology* **2018,** *13*.
81. Chatterjee, S.; Chauvier, A.; Dandpat, S. S.; Artsimovitch, I.; Walter, N. G., A translational riboswitch coordinates nascent transcription–translation coupling. *Proceedings of the National Academy of Sciences* **2021,** *118* (16), e2023426118.
82. Scull, C. E.; Dandpat, S. S.; Romero, R. A.; Walter, N. G., Transcriptional Riboswitches Integrate Timescales for Bacterial Gene Expression Control. *Front Mol Biosci* **2021,** *7*, 607158-607158.
83. Göhring, J.; Kellner, F.; Schrangl, L.; Platzer, R.; Klotzsch, E.; Stockinger, H.; Huppa, J. B.; Schütz, G. J., Temporal analysis of T-cell receptor-imposed forces via quantitative single molecule FRET measurements. *Nature Communications* **2021,** *12* (1), 2502.
84. Filius, M.; Kim, S. H.; Severins, I.; Joo, C., High-Resolution Single-Molecule FRET via DNA eXchange (FRET X). *Nano Letters* **2021,** *21* (7), 3295-3301.
85. Laitinen, O. H.; Nordlund, H. R.; Hytönen, V. P.; Kulomaa, M. S., Brave new (strept)avidins in biotechnology. *Trends in Biotechnology* **2007,** *25* (6), 269-277.
86. IDT OligoAnalyzer. https://www.idtdna.com/calc/analyzer.
87. Qiagen Tm Prediction and LNA Oligo Optimizer. https://geneglobe.qiagen.com/us/explore/tools/tm-prediction/form.
88. Johnson-Buck, A.; Li, J.; Tewari, M.; Walter, N. G., A guide to nucleic acid detection by single-molecule kinetic fingerprinting. *Methods* **2019,** *153*, 3-12.
89. NICOLAI, C.; SACHS, F., SOLVING ION CHANNEL KINETICS WITH THE QuB SOFTWARE. *Biophysical Reviews and Letters* **2013,** *08* (03n04), 191-211.
90. Blanco, M.; Walter, N. G., Analysis of complex single-molecule FRET time trajectories. *Methods Enzymol* **2010,** *472*, 153-178.
91. Roth, E.; Glick Azaria, A.; Girshevitz, O.; Bitler, A.; Garini, Y., Measuring the Conformation and Persistence Length of Single-Stranded DNA Using a DNA Origami Structure. *Nano Letters* **2018,** *18* (11), 6703-6709.
92. IDT. Locked nucleic acids and their applications. https://www.idtdna.com/pages/technology/custom-dna-rna/locked-nucleic-acids.
93. Zadeh, J. N.; Steenberg, C. D.; Bois, J. S.; Wolfe, B. R.; Pierce, M. B.; Khan, A. R.; Dirks, R. M.; Pierce, N. A., NUPACK: Analysis and design of nucleic acid systems. *Journal of Computational Chemistry* **2011,** *32* (1), 170-173.
94. Caltech. NUPACK Analysis 2007.
95. Blake, R. D.; Delcourt, S. G., Thermodynamic effects of formamide on DNA stability. *Nucleic Acids Res* **1996,** *24* (11), 2095-2103.
96. Bronson, J. E.; Fei, J.; Hofman, J. M.; Gonzalez, R. L.; Wiggins, C. H., Learning Rates and States from Biophysical Time Series: A Bayesian Approach to Model Selection and Single-Molecule FRET Data. *Biophysical Journal* **2009,** *97* (12), 3196-3205.
97. Becker, N. B.; Rosa, A.; Everaers, R., The radial distribution function of worm-like chains. *The European Physical Journal E* **2010,** *32* (1), 53-69.
98. Saleh, O. A.; McIntosh, D. B.; Pincus, P.; Ribeck, N., Nonlinear Low-Force Elasticity of Single-Stranded DNA Molecules. *Phys. Rev. Lett.* **2009,** *102* (6), 068301.
99. Marko, J. F.; Siggia, E. D., Stretching DNA. *Macromolecules* **1995,** *28* (26), 8759-8770.

100. Chen, H.; Meisburger, S. P.; Pabit, S. A.; Sutton, J. L.; Webb, W. W.; Pollack, L., Ionic strength-dependent persistence lengths of single-stranded RNA and DNA. *Proc. Natl. Acad. Sci. U. S. A.* **2012,** *109* (3), 799.
101. Seol, Y.; Skinner, G. M.; Visscher, K., Elastic Properties of a Single-Stranded Charged Homopolymeric Ribonucleotide. *Phys. Rev. Lett.* **2004,** *93* (11), 118102.
102. Muinao, T.; Pal, M.; Boruah, H. P. D., Cytosolic and Transmembrane Protein Extraction Methods of Breast and Ovarian Cancer Cells: A Comparative Study. *J Biomol Tech* **2018,** *29* (3), 71-78.
103. Zhang, D. Y.; Seelig, G., Dynamic DNA nanotechnology using strand-displacement reactions. *Nature Chemistry* **2011,** *3* (2), 103-113.
104. Dunn, K.; Trefzer, M.; Johnson, S.; Tyrrell, A., Investigating the dynamics of surface-immobilized DNA nanomachines. *Scientific reports* **2016,** *6*, 29581.
105. ThermoFisher. Alexa Fluor Dyes—Across the Spectrum. https://www.thermofisher.com/us/en/home/brands/molecular-probes/key-molecular-probes-products/alexa-fluor/alexa-fluor-dyes-across-the-spectrum.html.
106. Casey, J.; Davidson, N., Rates of formation and thermal stabilities of RNA:DNA and DNA:DNA duplexes at high concentrations of formamide †. *Nucleic Acids Res* **1977,** *4* (5), 1539-1552.
107. Mestdagh, P.; Hartmann, N.; Baeriswyl, L.; Andreasen, D.; Bernard, N.; Chen, C.; Cheo, D.; D'Andrade, P.; DeMayo, M.; Dennis, L.; Derveaux, S.; Feng, Y.; Fulmer-Smentek, S.; Gerstmayer, B.; Gouffon, J.; Grimley, C.; Lader, E.; Lee, K. Y.; Luo, S.; Mouritzen, P.; Narayanan, A.; Patel, S.; Peiffer, S.; Rüberg, S.; Schroth, G.; Schuster, D.; Shaffer, J. M.; Shelton, E. J.; Silveria, S.; Ulmanella, U.; Veeramachaneni, V.; Staedtler, F.; Peters, T.; Guettouche, T.; Wong, L.; Vandesompele, J., Evaluation of quantitative miRNA expression platforms in the microRNA quality control (miRQC) study. *Nat. Methods* **2014,** *11* (8), 809-815.
108. Postel, M.; Roosen, A.; Laurent-Puig, P.; Taly, V.; Wang-Renault, S. F., Droplet-based digital PCR and next generation sequencing for monitoring circulating tumor DNA: a cancer diagnostic perspective. *Expert. Rev. Mol. Diagn.* **2018,** *18* (1), 7-17.
109. Gilboa, T.; Garden, P. M.; Cohen, L., Single-molecule analysis of nucleic acid biomarkers – A review. *Anal. Chim. Acta* **2020,** *1115*, 61-85.
110. Daniel, R.; Wu, Q.; Williams, V.; Clark, G.; Guruli, G.; Zehner, Z., A Panel of MicroRNAs as Diagnostic Biomarkers for the Identification of Prostate Cancer. *International Journal of Molecular Sciences* **2017,** *18* (6), 1281.
111. Weis, A.; Marquart, L.; Calvopina, D. A.; Genz, B.; Ramm, G. A.; Skoien, R., Serum MicroRNAs as Biomarkers in Hepatitis C: Preliminary Evidence of a MicroRNA Panel for the Diagnosis of Hepatocellular Carcinoma. *International Journal of Molecular Sciences* **2019,** *20* (4), 864.
112. He, L.; Thomson, J. M.; Hemann, M. T.; Hernando-Monge, E.; Mu, D.; Goodson, S.; Powers, S.; Cordon-Cardo, C.; Lowe, S. W.; Hannon, G. J.; Hammond, S. M., A microRNA polycistron as a potential human oncogene. *Nature* **2005,** *435* (7043), 828-833.
113. Sultankulova, K. T.; Kozhabergenov, N. S.; Strochkov, V. M.; Burashev, Y. D.; Shorayeva, K. A.; Chervyakova, O. V.; Rametov, N. M.; Sandybayev, N. T.; Sansyzbay, A. R.; Orynbayev, M. B., New oligonucleotide microarray for rapid diagnosis of avian viral diseases. *Virology Journal* **2017,** *14* (1), 69.

114. Wickramasinghe, S.; Do, T.; Tran, P., FDM-Based 3D Printing of Polymer and Associated Composite: A Review on Mechanical Properties, Defects and Treatments. *Polymers* **2020,** *12* (7), 1529.
115. Zhang, K.; Kang, D.-K.; Ali, M. M.; Liu, L.; Labanieh, L.; Lu, M.; Riazifar, H.; Nguyen, T. N.; Zell, J. A.; Digman, M. A.; Gratton, E.; Li, J.; Zhao, W., Digital quantification of miRNA directly in plasma using integrated comprehensive droplet digital detection. *Lab on a Chip* **2015,** *15* (21), 4217-4226.
116. Tuaeva, N. O.; Falzone, L.; Porozov, Y. B.; Nosyrev, A. E.; Trukhan, V. M.; Kovatsi, L.; Spandidos, D. A.; Drakoulis, N.; Kalogeraki, A.; Mamoulakis, C.; Tzanakakis, G.; Libra, M.; Tsatsakis, A., Translational Application of Circulating DNA in Oncology: Review of the Last Decades Achievements. *Cells* **2019,** *8* (10), 1251.
117. Ma, H.; Bell, K. N.; Loker, R. N., qPCR and qRT-PCR analysis: Regulatory points to consider when conducting biodistribution and vector shedding studies. *Molecular Therapy - Methods & Clinical Development* **2021,** *20*, 152-168.
118. Wan, J. C. M.; Massie, C.; Garcia-Corbacho, J.; Mouliere, F.; Brenton, J. D.; Caldas, C.; Pacey, S.; Baird, R.; Rosenfeld, N., Liquid biopsies come of age: towards implementation of circulating tumour DNA. *Nature Reviews Cancer* **2017,** *17* (4), 223-238.
119. Šulc, P.; Romano, F.; Ouldridge, T. E.; Doye, J. P.; Louis, A. A., A nucleotide-level coarse-grained model of RNA. *J Chem Phys* **2014,** *140* (23), 235102.
120. Ouldridge, T.; Louis, A.; Doye, J., Structural, mechanical, and thermodynamic properties of a coarse-grained DNA model. *The Journal of chemical physics* **2011,** *134*, 085101.
121. Sulc, P.; Romano, F.; Ouldridge, T.; Rovigatti, L.; Doye, J.; Louis, A., Sequence-dependent thermodynamics of a coarse-grained DNA model. *The Journal of chemical physics* **2012,** *137*, 135101.
122. Juracek, J.; Slaby, O., Urinary MicroRNAs as Emerging Class of Noninvasive Biomarkers. In *RNA Interference and CRISPR Technologies: Technical Advances and New Therapeutic Opportunities*, Sioud, M., Ed. Springer US: New York, NY, 2020; pp 221-247.
123. Rinaldi, A. J.; Lund, P. E.; Blanco, M. R.; Walter, N. G., The Shine-Dalgarno sequence of riboswitch-regulated single mRNAs shows ligand-dependent accessibility bursts. *Nature Communications* **2016,** *7* (1), 8976.
124. Chatterjee, T.; Knappik, A.; Sandford, E.; Tewari, M.; Choi, S. W.; Strong, W. B.; Thrush, E. P.; Oh, K. J.; Liu, N.; Walter, N. G.; Johnson-Buck, A., Direct kinetic fingerprinting and digital counting of single protein molecules. *Proceedings of the National Academy of Sciences* **2020,** *117* (37), 22815.
125. Iqbal, M.; Tao, Y.; Xie, S.; Zhu, Y.; Chen, D.; Wang, X.; Huang, L.; Peng, D.; Sattar, A.; Shabbir, M. A. B.; Hussain, H. I.; Ahmed, S.; Yuan, Z., Aqueous two-phase system (ATPS): an overview and advances in its applications. *Biological Procedures Online* **2016,** *18* (1), 18.
126. TIBANYENDA, N.; DE BRUIN, S. H.; HAASNOOT, C. A. G.; VAN DER MAREL, G. A.; VAN BOOM, J. H.; HILBERS, C. W., The effect of single base-pair mismatches on the duplex stability of d(T-A-T-T-A-A-T-A-T-C-A-A-G-T-T-G) · d(C-A-A-C-T-T-G-A-T-A-T-T-A-A-T-A). *European Journal of Biochemistry* **1984,** *139* (1), 19-27.
127. Mogilyansky, E.; Rigoutsos, I., The miR-17/92 cluster: a comprehensive update on its genomics, genetics, functions and increasingly important and numerous roles in health and disease. *Cell Death & Differentiation* **2013,** *20* (12), 1603-1614.

128. Zedan, A. H.; Blavnsfeldt, S. G.; Hansen, T. F.; Nielsen, B. S.; Marcussen, N.; Pleckaitis, M.; Osther, P. J. S.; Sørensen, F. B., Heterogeneity of miRNA expression in localized prostate cancer with clinicopathological correlations. *PLoS One* **2017,** *12* (6), e0179113-e0179113.
129. Zhang, Y.; Kojima, T.; Kim, G.-A.; McNerney, M. P.; Takayama, S.; Styczynski, M. P., Protocell arrays for simultaneous detection of diverse analytes. *Nature Communications* **2021,** *12* (1), 5724.
130. Gómez-García, P. A.; Garbacik, E. T.; Otterstrom, J. J.; Garcia-Parajo, M. F.; Lakadamyali, M., Excitation-multiplexed multicolor superresolution imaging with fm-STORM and fm-DNA-PAINT. *Proc Natl Acad Sci U S A* **2018,** *115* (51), 12991-12996.